Measurement of the solar neutrino energy spectrum at Super-Kamiokande

スーパー神岡実験における太陽ニュートリノのエネルギースペクトルの研究

石野宏和

Measurement of the solar neutrino energy spectrum at Super-Kamiokande

Hirokazu Ishino

Doctor Thesis, University of Tokyo
January 1999

Abstract

Measurements of solar neutrinos at Super-Kamiokande are presented. Super-Kamiokande started taking data on the 1st of April in 1996. In the present thesis, data taken from 31th of May, 1996 to 25th of March, 1998 (total live time is 503.8days) are used for this analysis with electron energy threshold of 6.5MeV and in 22.5ktons fiducial volume.

We measured energy spectrum of recoil electrons scattered by the solar neutrinos. If neutrino flavor oscillations, which are the most plausible solution for solving the solar neutrino problem, happen, the energy spectrum shape distort from that of expected. Comparison of the energy spectrum shape between the observation and the expectation with possible systematic errors gives a χ^2 value of 24.4 with 15 degrees of freedom, which corresponds to a 5.9% confidence level. This slightly small significance is discussed with possible large hep neutrino flux and neutrino oscillations.

Acknowledgment

First of all, I would like to express my sincere appreciation to my advisor, Prof. Y.Totsuka. He introduced me this great experiment, namely Super-Kamiokande, and supported me throughout this work.

I would like to show my appreciation to Prof. Y.Suzuki. His advice and encouragement were helpful for my analysis.

I gratefully acknowledge the helpful advice of Prof. M.Nakahata. He taught me a lot of things which are useful and helpful for my work. Without his help, I would never accomplish my thesis.

I would like to thank Dr. K.Inoue, Dr. Y.Fukuda, Dr. Y.Takeuchi, and Dr. Y.Koshio for their suggestions and advice about solar neutrino analysis. I also wish to thank the graduate students: Dr. T.Yamaguchi, Dr. H.Okazawa, Mr. E.Ichihara, Mr. N.Sakurai and Ms. M.Nemoto, and the members in USA: Prof. B.Svoboda, Dr. J.Hill, Dr. M.Vagins, Dr. M.Smy, Dr. B.K.Kim and Mr. R.Sanford.

I would like to thank Dr. K.Martens and Mr. E.Blaufuss for reading and checking this thesis.

I would like to thank all the other Super-Kamiokande collaborators. Especially, Prof. T.Kajita, Dr. Y.Itow, Dr. M.Miura, Mr. M.Shiozawa, Mr. T.Hayakawa, Dr. S.Kasuga, Dr. Y.Hayato, Mr. Y.Obayashi, Mr. K.Ishihara, Mr. K.Okumura, Mr. M.Etoh and Mr. J.Kameda. I often had useful discussions with them about the experiment.

Finally, I gratefully acknowledge the cooperation of Kamioka Mining and Smelting Company and financial support of the Japan Society for the Promotion of Science.

Contents

List of Figures

Chapter 1

Introduction

The sun is the source of the energy for all life on the earth, the source of information of stellar evolution as a standard star for astronomers, and also the intense source of neutrinos for physicists. Solar neutrinos are generated in the central core of the sun with solar energy as a result of nuclear fusion. It takes about $1 \sim 2 \times 10^5$ years for photons generated in the core to reach the solar surface, hence we cannot investigate the core by optical measurements. On the other hand, because of the large permeability of neutrinos, an observation of solar neutrinos enables us to investigate the core of the sun. Solar neutrinos pass through very dense matter that we never achieve on the earth and they travel the long distance of $1.5 \cdot 10^8$km from the sun to the earth. Such characteristic conditions provide us an opportunity to investigate almost unknown properties of neutrinos such as mass and magnetic moment.

Solar neutrinos have been observed by four different experiments: the Homestake experiment which uses Cl nuclei as a target, Kamiokande which used electrons in H_2O molecules, and GALLEX and SAGE which use Ga. The Homestake experiment first observed that the flux of solar neutrinos is significantly smaller than the flux calculated by the Standard Solar Model (SSM). This discrepancy, the so-called 'Solar neutrino problem', was confirmed by other experiments later. Moreover, it was found that a degree of deficit of the solar neutrino flux depends on targets. Taking into account the energy threshold of each experiment, at present, the most suitable solution of the problem is thought to be neutrino flavor oscillations. It indicates that neutrinos have mass and mix with different generations. The neutrino oscillation phenomenon in the vacuum was studied by Z.Maki, M.Nakagawa, S.Sakata, V.Gribov and B.Pontecorvo in references [1] at first. In 1978, Wolfenstein [2] considered neutrino oscillations in the matter, and in 1986 Mikheyev and Smirnov [3] found the feature of adiabatic neutrino transition in matter. It was applied to the sun and predicted the energy dependence of the solar neutrino deficit. So, this is called 'MSW effect'.

In order to solve the solar neutrino problem, not only high statistical solar neutrino data should be observed but also quantities which are independent from SSM expectations, such as distortion of energy spectrum and variations of solar neutrino event rate, should be measured. For that purpose, second generation solar neutrino observations, such as Super-Kamiokande, was proposed and started in 1996.

In this thesis, the results of ^{8}B solar neutrino observation in Super-Kamiokande with about 500 days data are reported. In Chapter 2, details of the SSM and the MSW effect is presented. In Chapter 3, a description of Super-Kamiokande is presented. In Chapter 4 and 5, event reconstructions and calibration of the Super-Kamiokande detector are described respectively. Chapter 6 gives an account of the reduction method of the data in order to eliminate backgrounds for the ^{8}B solar neutrino observation. Chapter 7 is devoted to descriptions of the results of the ^{8}B neutrino flux measurement, time variation of the flux, the energy spectrum of recoil electrons scattered by the solar neutrinos, and systematic errors that are important to see a distortion of the ^{8}B neutrino energy spectrum. Chapter 8 describes the two flavor neutrino oscillations analysis based on the results and systematic errors.

Chapter 2

Solar Neutrinos and the Standard Solar Model

This chapter gives an account of the Standard Solar Model (SSM), existing solar neutrino experiments, and the Mikheyev, Smirnov, Wolfenstein (MSW) effect. The SSM describes stellar evolution and predicts the flux of solar neutrinos, while solar neutrino experiments provide the observational data about these fluxes. The MSW effect, which describes the propagation of massive neutrinos through matter, opens a pioneering way to solve the contradiction between the SSM prediction and observed data under certain conditions.

2.1 Solar neutrinos

There had been questions about what the source of energy of the sun is in former days. It had been considered that the gravitational or chemical energy maintained the sun shining. The time scale that the gravitational energy can support the energy is $\sim GM_\odot^2/R_\odot L_\odot \sim 10^7$year. Here, G, $M_\odot$, $R_\odot$ and $L_\odot$ are gravitational constant, the solar mass, radius, and luminosity, respectively. A period that chemical energy can support is, even shorter, about 10^4 years. It is known that the age of the sun is about $\sim 10^{10}$ years. This evidence is supported by the facts that the oldest rock was molded about 3.8 billion years ago, and that meteoritic ages are of order 4.5 billion years [4]. That means that gravitational or chemical energy cannot be the source of the solar energy. After the discovery of radiation and quantum mechanics, it was found that the nuclear fusion is the only source of the energy that can maintain the sun shining for such a long time.

The temperature of the center of the sun in which nuclear fusion occurs can be calculated by the theory of stellar evolution, and it is found that the temperature is of order 10^7K. On the other hand, hydrogen atoms, namely protons, which are the main fuels of nuclear fusion, repel each other due to the electrical charge. In order to trigger off the nuclear fusion, these protons have to have enough thermal energy to overcome the Coulomb potential, but protons do not have sufficient thermal energy at such a temperature. However, thanks to tunneling, which is a pure quantum effect, nuclear fusion can occur. The energy dependence of the nuclear fusion

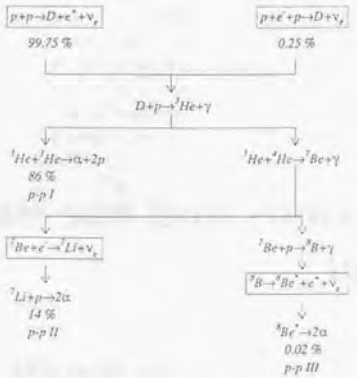

Figure 2–1: PP-chain

cross section is [5]:

$$\sigma(E) = \frac{S(E)}{E}\exp(-2\pi\eta) \tag{2-1}$$

$$\eta = Z_1 Z_2 \frac{e^2}{\hbar v} \tag{2-2}$$

where, $S(E)$ is the cross section factor (when $E = 0$, this factor is denoted as S_0), and the factor $\exp(-2\pi\eta)$ is the Gamow penetration factor which includes the barrier penetrating factor. For proton-proton interactions, this factor is of order 10^{-5}, and this suppression factor enables the sun to shine for several billion years.

The nuclear fusion reaction is formally written as the following equation:

$$4\mathrm{p} \rightarrow \alpha + 2\mathrm{e}^+ + 2\nu_e \tag{2-3}$$

In this reaction, two electron neutrinos are generated with an energy release of 26.73MeV. In the sun, this net reaction proceeds in two different reaction systems, the so-called proton-proton chain (pp-chain) and the Carbon-Nitrogen-Oxygen cycle (CNO-cycle). These reaction systems are shown in figure 2–1 and 2–2. The reactions that generate electron neutrinos in the pp-chain are:

$$\mathrm{p{+}p} \rightarrow \mathrm{D} + \mathrm{e}^+ + \nu_e \qquad \text{(pp neutrino)} \tag{2-4}$$

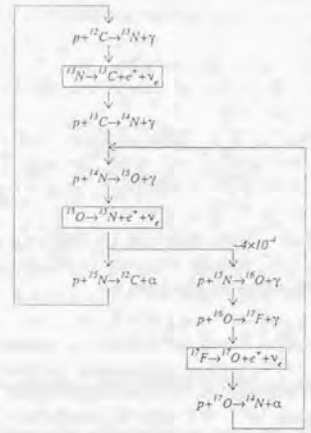

Figure 2–2: CNO-cycle

$$p+e^-+p \rightarrow D+\nu_e \qquad \text{(pep neutrino)} \tag{2-5}$$
$$^7Be+e^- \rightarrow {}^7Li+\nu_e \qquad (^7\text{Be neutrino}) \tag{2-6}$$
$$^8B \rightarrow {}^8Be^*+e^++\nu_e \qquad (^8\text{B neutrino}) \tag{2-7}$$

In addition to these reactions, there is another reaction which generates neutrinos called hep neutrino,

$$^3He+p \rightarrow \alpha+e^++\nu_e \qquad \text{(hep neutrino)} \tag{2-8}$$

The nuclear fusion reactions are dominated by (2-4), and hence the flux of pp neutrinos is the largest one (it accounts for about 90% for the total solar neutrino flux). Unfortunately the end point energy of pp neutrinos is small (0.420MeV). At present day, these neutrinos are detected by radiochemical ^{71}Ga experiments only, which are described later. The cross section of reaction (2-4) is calculated accurately by the theory of weak interactions and the measured properties of proton-proton or proton-deuteron scattering.

Reaction (2-5) emits a 1.4MeV neutrino line. These neutrinos can be detected in the ^{37}Cl experiment, but this contribution to the signal is very small (see table 2-3).

Reaction (2-6) generates two lines (0.861MeV or 0.383MeV) of neutrino energies[1]. Neutrinos with higher energy line can be detected by ^{37}Cl experiment.

Reaction (2-7) generates ^{8}B neutrinos. These neutrinos are relatively easy to detect because of their high energy endpoint ($\sim$ 15MeV) and are detected by all previous experiments. The rate of this reaction in the sun is determined by the reaction

$$^7Be+p \rightarrow {}^8B+\gamma \tag{2-9}$$

Unfortunately, the cross section of this reaction is known with comparatively larger uncertainty ($\sim$10%) than other reactions.

Though the last reaction (2-8) in the pp-chain generates the most energetic neutrinos, whose spectrum endpoint is 18.77MeV, the flux of these neutrinos is quite small (the ratio to the flux of ^{8}B neutrinos is order 10^{-3}).

In the CNO-cycle, there are three reactions which generate neutrinos,

$$^{13}N \rightarrow {}^{13}C+e^++\nu_e \qquad (q \leq 1.199\text{MeV}) \tag{2-10}$$
$$^{15}O \rightarrow {}^{15}N+e^++\nu_e \qquad (q \leq 1.732\text{MeV}) \tag{2-11}$$
$$^{17}F \rightarrow {}^{17}O+e^++\nu_e \qquad (q \leq 1.740\text{MeV}) \tag{2-12}$$

where, q indicates neutrino energy. The characteristic energy of these reactions is not so large, and the percentage of solar luminosity contributed by CNO-cycle reactions is estimated to be only about 1.5% in the SSM. Hence, contribution of these neutrinos to solar neutrino experiments is small.

[1]The reason why two lines appear is that there are two final states for ^{7}Li.

input parameter	value
Luminosity($L_\odot$)	$3.844(1\pm0.004)\times10^{33}erg\cdot$ s^{-1}
Mass($M_\odot$)	1.989×10^{30}kg
Radius($R_\odot$)	6.96×10^{5}km
Age	$4.57(1\pm0.004)\times10^{9}$years

Table 2-1: input parameters used by BP98 model [12]

2.2 The Standard Solar Model

The Standard Solar Model (SSM) is a model which describes stellar evolution, the status of the sun, and calculates the solar neutrino flux according to the equation of state. Input parameters used are nuclear reaction cross section, the solar luminosity, the solar age, elemental abundances, radiative opacities, etc. There exist several SSMs calculated by many authors, Turck Chièze and Lopes (1993)[6], Castellani *et al.* (1994)[7], Kovetz and Shaviv (1994)[8], Christensen-Dalsgaard (1994)[9], and Shi *et al.* (1994)[10]. Element diffusion driven by the strong pull of gravity on helium and heavier elements toward the stellar interior relative to hydrogen is also included in modern solar model calculations (for example, J.N.Bahcall and M.H.Pinsonneault (BP95) [11] and (BP98) [12]). The solar neutrino flux calculated by the BP98 model is employed in this thesis as a theoretical reference. It has been found that the solar neutrino fluxes calculated by these models are consistent within about 2% when the same input parameters are adopted.

The input parameters used in the BP98 model are listed in table 2-1. After the equation of stellar state is solved numerically from these input parameters, the interior state of the sun such as the radial dependence of temperature, matter density, pressure, and the neutrino fluxes can be computed. The radial dependence of the electron density is shown in fig 2-3. The computed neutrino flux is tabulated in table 2-2. The energy spectrum of solar neutrinos is shown in figure 2-4. And the production fractions of the neutrinos as a function of the solar radius are shown in figure 2-5. As seen on table 2-2, the uncertainty of the pp neutrino flux is very small ($\pm$1%). On the other hand, the uncertainty of the ^{8}B neutrino flux is large ($^{+19}_{-14}$%). The main sources of this error are the cross section uncertainty in reaction (2-9) (10.5%), the cross section of reaction (^{3}He+^{4}He$\rightarrow{}^7$Be+γ, see figure 2-1) (7.5%), opacity (5.2%), the ratio of heavy elemental abundance relative to hydrogen (Z/X) (4.2%), and element diffusion (4.0%) [12]. The dependence of ^{8}B neutrino flux ($\phi(^8\text{B})$) on two of them is expressed as [5]:

$$\phi(^8\text{B}) \propto S_{17}^{1.0}(\text{Z/X})^{-0.08} \tag{2-13}$$

where S_{17} is the cross section factor of reaction (2-9). The ^{8}B neutrino flux is proportional to S_{17}, and in order to reduce the uncertainty in the prediction of this flux, a precise measurement of S_{17} is crucial. It is almost impossible to measure the ^{7}Be+p cross section at the temperature of the solar core, because at the low energies corresponding to the temperature at the core of the sun (10^7K $\sim$ 1keV), the event rate of this reaction is too low. At present, the only way to obtain the cross section factor ($S_{17}(0)$) is to measure it at energies down to $\sim$ 100keV and

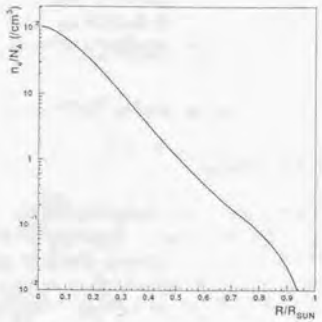

Figure 2–3: The radial dependence of electron density in the sun. The horizontal axis is $R/R_\odot$ and vertical axis is n_e/N_A, where R is the solar radius, n_e is the electron density (/cm^3) and N_A is the Avogadro constant.

Type of neutrino	Flux (/cm^2/s)
pp-chain	
pp neutrino	$5.94(1.00\pm0.01)\times10^{10}$
pep neutrino	$1.39(1.00\pm0.01)\times10^{8}$
^{7}Be neutrino	$4.80(1.00\pm0.09)\times10^{9}$
^{8}B neutrino	$5.15(1.00^{+0.19}_{-0.14})\times10^{6}$
hep neutrino	2.10×10^{3}
CNO-cycle	
^{13}N	$6.05(1.00^{+0.19}_{-0.13})\times10^{8}$
^{15}O	$5.32(1.00^{+0.22}_{-0.15})\times10^{8}$
^{17}F	$6.33(1.00^{+0.12}_{-0.11})\times10^{6}$

Table 2–2: Solar neutrino fluxes on the earth predicted by BP98 model [12].

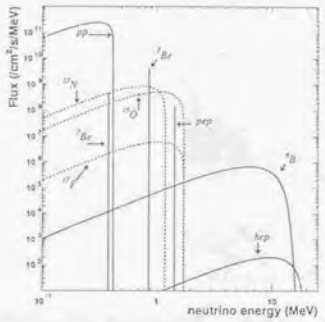

Figure 2–4: Energy spectrum of solar neutrinos

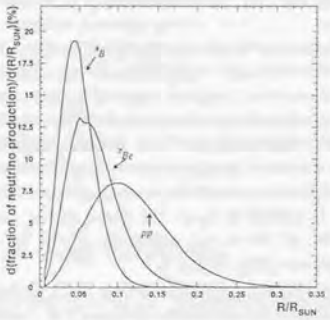

Figure 2–5: Production point distribution as a function of the solar radius

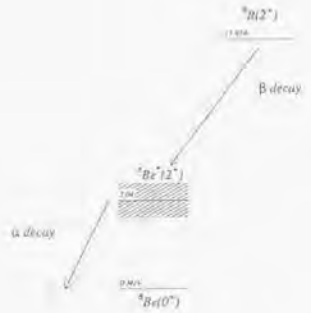

Figure 2-6: Energy levels of decay chains of $^8B(\beta^+)^8Be(2\alpha)$

extrapolate down to the solar temperature. Reference [13] summarizes measurements of this factor. BP98 model uses recommended value in the reference [13], which is measured value of an experiment [14], namely $S_{17}(0) = 19^{+4}_{-2}$eVb.

2.3 Energy spectrum of ^{8}B neutrinos

The ^{8}B neutrinos can be detected most easily among the solar neutrinos, since the energy of these neutrinos is high enough to eliminate backgrounds from natural radioactivity and the cross section of neutrino interaction to the target is large. The importance in observing the ^{8}B neutrinos comes from, (1) the absolute flux strongly depends on the temperature at the core (18-th power), so it is a most suitable monitor of the temperature, and (2) investigations of neutrino oscillations in a broad neutrino energy range is possible. A precise measurement of energy spectrum of the ^{8}B neutrinos is one of the most important keys for solving the solar neutrino problem. Therefore, it is crucial to know the shape of the energy spectrum precisely. In this section, a brief description of the energy spectrum of the ^{8}B neutrinos is given. The details of it are laid out in the papers [15], [16], [17].

The ^{8}B neutrinos are generated in the β decay of reaction (2-7). Subsequently, $^8Be^*$ decays to 2α. Energy levels of this sequence of decays are shown in figure 2-6. Unfortunately the transition to the ground state of ^{8}Be is forbidden in the decay of ^{8}B. Thus the β-decay of ^{8}B proceeds to a broad exited state of ^{8}Be, which affects the ensuing β-decay spectrum. Yet the subsequent decay of the exited state into 2α particles allow to determine the width of this intermediate state, which is needed to calculate the ^{8}B neutrino spectrum. Several measurements of the

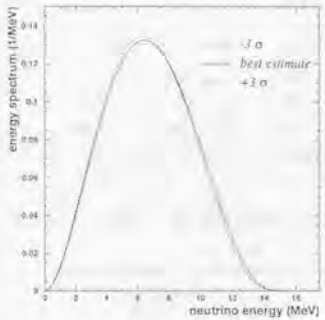

Figure 2-7: ^{8}B neutrino energy spectrum with $\pm 3\sigma$ error calculated in the reference [15]. Solid line is the best-estimate (standard) spectrum. Two broken lines are those allowed by the $\pm 3\sigma$ uncertainties as described in the text.

energy spectrum of these α particles exist [18], [19], [20], [21]. In reference [15], the energy spectrum of neutrinos and positrons is calculated from these measurements of α particle energy distributions and the calculated positron energy spectrum is compared with that measured in reference [16]. The agreement is good (reduced χ^2 of comparison between experimentally measured and theoretically calculated energy spectrum ~ 1). In reference [15], the uncertainties of the ^{8}B neutrino energy spectrum are also discussed. The main uncertainty comes from a bias in the measured α particle energy, i.e. $E_\alpha \to E_\alpha + b$. This bias differ $\sim$0.05MeV among the four experiments, while the mean value of energy spectrum of α particles is $\sim$1.5MeV. This energy bias is attributed to the energy calibration of each measurement. Reference [15] calculated this bias and 3σ error to $b = 0.025 \pm 0.072$MeV. Using this input, the energy spectrum of the ^{8}B neutrinos is calculated. The result is shown in figure 2-7, with a $\pm 3\sigma$ error. In this thesis, the ^{8}B energy spectrum estimated in reference [15] with error is employed as the standard.

2.4 Observation of solar neutrinos

In this section, solar neutrino observations by four experiments are described.

2.4.1 Homestake Experiment

The first experiment which observed solar neutrinos is the Homestake chlorine experiment. It started solar neutrino observation in 1970. This experiment uses ^{37}Cl nuclei as a neutrino target,

neutrino source	Cl(SNU)	Ga(SNU)
pp	0.00	69.6
pep	0.2	2.8
^{7}Be	1.15	34.4
^{8}B	5.9	12.4
^{13}N	0.1	3.7
^{15}O	0.4	6.0
total	$7.7^{+1.2}_{-1.0}$	129^{+8}_{-6}

Table 2-3: The contribution of neutrino source to capture rate for ^{37}Cl and ^{71}Ga [12].

which capture electron neutrinos by an inverse β decay reaction:

$$\nu_e + {}^{37}\mathrm{Cl} \rightarrow \mathrm{e}^- + {}^{37}\mathrm{Ar} \tag{2-14}$$

The detector contains 615 metric tons of liquid perchloroethylene (C_2Cl_4) in a cylindrical tank, which is located at a depth of 1480 meters underground (4400 m water equivalent) in the Homestake Gold Mine at Lead, South Dakota. This deep depth helps to avoid energetic cosmic ray muons which produce ^{37}Ar by photo nuclear interactions and cause a serious background. The natural abundance of ^{37}Cl nuclei is 24.23%, therefore, the number of ^{37}Cl nucleus is about 2.2×10^{30}. The energy threshold of reaction (2-14) is 0.814MeV, allowing the observation not only of ^{8}B neutrinos but also the higher energy line from the ^{7}Be neutrinos[2]. ^{37}Ar nuclei capture an electron by the inverse reaction of (2-14) with a half life of 35days and decay to ^{37}Cl under emission of an Auger electron of 2.82keV in energy. The ^{37}Ar atoms produced in the inverse β-decay reaction are extracted by purging the liquid with helium and are collected from the gas stream in a charcoal trap. Extraction is initiated after typically three months of exposure to solar neutrinos. The number of ^{37}Ar atoms is counted by detecting the Auger electrons with a gas proportional counter. The cross section for reaction (2-14) has contributions from transitions to the ground state of ^{37}Ar as well as to exited states. For the transition to the ground state the cross section can easily be exhausted from the life time of ^{37}Ar. For the excited states, it is based upon the measurement of the β decay of ^{37}Ca to ^{37}K[15]. The expected event rate of solar neutrino interactions (2-14) is estimated to be $7.7^{+1.2}_{-1.0}$ SNU (10^{-36} captures per second per atom) in the BP98 model [12]. The contribution of each solar neutrino sources to the total capture rate is shown in table 2-3. The measured count rate of solar neutrinos is [22]:

$$2.56\pm0.16(\mathrm{stat.})\pm0.16(\mathrm{syst.})\mathrm{SNU} \tag{2-15}$$

and the ratio to the theoretical prediction is:

$$\frac{\mathrm{Data(Cl)}}{\mathrm{SSM}} = 0.332\pm0.030 \tag{2-16}$$

[2]Of course, pep neutrinos and neutrinos produced by CNO-cycle can also be detected, but, as described in previous section, the contribution of the fluxes of these neutrinos is very small.

Thus the measured flux of solar neutrinos is significantly smaller than that predicted from the SSM. This is so-called the first solar neutrino problem.

2.4.2 Kamiokande

Solar neutrino observations at Kamiokande started in 1987. Kamiokande used a water Cherenkov counter. The detector with 3000 tons of pure water was located about 1000m underground (2700 m water equivalent) in the Mozumi mine, Kamioka town, Gifu prefecture, Japan. The inner photosensitive volume which was a cylindrical in shape (15.6 m in diameter and 16.1 m in height) contained 2140 tons of water viewed by 948 50cm-diameter-photo-multiplier tubes (PMTs), which are distributed over the inner surface of the water tank, providing a photo-coverage of 20%. For solar neutrino observation, fiducial volume containing 680 tons water is used. The solar neutrinos are detected using the reaction:

$$\nu_e + \mathrm{e} \rightarrow \nu_e + \mathrm{e} \tag{2-17}$$

The recoil electron emits Cherenkov photons in the water, which are detected by the PMTs surrounding the water. From the observed number of Cherenkov photons, hit pattern in the detector and timing information of each PMT, the energy and direction of the electron and the vertex where the event happened are reconstructed. Since the scattered electron keeps the neutrino direction within $\sqrt{2m_e/E}$, where m_e is the electron mass and E is neutrino energy, solar neutrino events can be identified by their directional correlation to the sun. This was the first experiment which detected the solar neutrinos directly and showed that the measured neutrinos really come from the sun.

Because the energy threshold for the recoil electrons in Kamiokande was ~7.0MeV, Kamiokande can only observe ^{8}B neutrinos. The flux of solar neutrinos (^{8}B neutrino) measured over 2079 days is [23], [24],

$$2.80 \pm 0.19(stat.) \pm 0.33(syst.)(\times10^{6}\mathrm{cm}^{-2}\mathrm{s}^{-1}) \tag{2-18}$$

while the BP98 predicts $5.15(1.00^{+0.19}_{-0.14})\times10^{6}\mathrm{cm}^{-2}\mathrm{s}^{-1}$ (see table 2-2). This result confirms the first solar neutrino problem and suggested the second solar neutrino problem (the ^{7}Be problem) described later.

2.4.3 ^{71}Ga experiments

At present time, the experiments which detect pp neutrinos (end point is 0.420 MeV) are GALLEX and SAGE using ^{71}Ga targets. The inverse β-decay reaction is:

$$^{71}\mathrm{Ga} + \nu_e \rightarrow \mathrm{e}^- + {}^{71}\mathrm{Ge} \tag{2-19}$$

The energy threshold of this reaction is 0.2332 MeV. The ^{71}Ge atom decays via electron capture, which is the inverse reaction of (2-19), with a half life of 11.43 days. The number of ^{71}Ge atoms is counted by detecting Auger electrons and X-rays generated by the electron capture process. The energies of the Auger electrons and X-rays are listed in table 2-4.

type of particles	energy (keV)	electron orbit	branching ratio (%)
Auger electron	10.367	K	41.5
Auger electron X-ray	1.17 9.2	K	5.3
Auger electron X-ray	0.12 10.26	K	41.2
Auger electron	1.2	L	10.3
Auger electron	0.12	M	1.7

Table 2–4: The energies and branching ratios of Auger electrons and X-rays generated by an electron capture reaction of ^{71}Ge atom.

The GALLEX experiment, which started in 1991, uses a detector at the Gran Sasso Underground Laboratories (3300 m water equivalent) that contains 33 tons of gallium in the form of a gallium chloride solution ($GaCl_3$-HCl). After three or four weeks of exposure, the Ge atoms, which form $GeCl_4$ molecules, are extracted chemically. For counting the Ge decay, the Ge is found in the form of GeH_4. Together with Xenon, the GeH_4 is then used as counting gas in small proportional counter. The Ge decay in the proportional counter is identified by their characteristic energy depositions. The SAGE (Russian-American Gallium Experiment) experiment started in 1990 at the Baksan Neutrino Observatory in the Northern Caucasus Mountains. This experiment, which is carried out under 4715m water equivalent, uses 60 tons (until July 1991: 30tons) of liquid gallium as a detector. Gallium can be kept as liquid thanks to a low melting point (29.8°C). The extraction of Ge atoms is done chemically and, like in the GALLEX experiment, GeH_4 is introduced into small proportional counter to count the number of ^{71}Ge atoms.

The observed rate for each experiment is as follows:

$$77.5 \pm 6.2(\text{stat.})^{+4.3}_{-4.7}(\text{syst.})\text{SNU(for GALLEX (1991}\sim\text{1997))} \text{ [25]} \tag{2-20}$$

$$66.6^{+6.8}_{-7.1}(\text{stat.})^{+3.8}_{-4.0}(\text{syst.})\text{SNU(for SAGE (1990}\sim\text{1997))} \text{ [26]} \tag{2-21}$$

The expected event rate is 129^{+8}_{-6}SNU from the BP98, this means that both GALLEX and SAGE observed a significantly smaller solar neutrino flux than predicted and the Ga experiments also confirm the solar neutrino problems.

The merit of these experiments is that the detector response to neutrinos was calibrated directly using an intense artificial neutrino source, namely ^{51}Cr. ^{51}Cr is produced by neutron capture on ^{50}Cr at reactor. ^{51}Cr decays by electron capture with a half life of 27.71 days,

$$^{51}\text{Cr} + e^- \rightarrow {}^{51}\text{V} + \nu_e \tag{2-22}$$

90 % ^{51}Cr decays emitting a monochromatic ≈750 keV neutrino and, while in 10 % of the decays, a ≈430 keV neutrino and a 320 keV γ-ray are emitted. The strength of the source is determined

	GALLEX		SAGE(1994)
	First(1994)	Second(1995)	
Chromium weight(g)	35530±10	35575±10	512.7
The strength (×10^{15}Bq)	$63.4^{+1.1}_{-1.6}$	$69.1^{+3.3}_{-2.1}$	19.1±0.2

Table 2–5: Characteristics of the ^{51}Cr sources. The references are [27] for GALLEX and [28] for SAGE.

independently by neutron- and gamma-monitoring during the irradiation, by calorimetry, by gamma counting of energy of 320 keV and by chemical analysis of the decay product, ^{51}V. A source experiment was done twice for GALLEX and once for SAGE. The characteristics of the sources used in the experiments are listed in table 2–5.

The source experiments allow to compare directly the expected signal to the observed one. The ratio of these two quantities was found to be 0.93±0.08 [25] for GALLEX and 0.95±0.12 [28] for SAGE. GALLEX also carried out a test for recovery efficiency using ^{71}As decay. A ^{71}As decays via electron capture (68%) or positron decay (32%) to a ^{71}Ge*, which decays to ^{71}Ge under emission of a γ-ray of 0.175MeV. A known number of ^{71}As atoms (∼30000) was introduced into the GALLEX target solution, and ^{71}Ge recovery factor was measured. The result is 99.9±0.8%(1σ) [25]. This result supplemented the validity of the measurement method in the GALLEX radiochemical neutrino detector. These agreements between measurement and prediction confirm validity of the results of solar neutrino measurement at the Ga experiments.

2.4.4 The ^{7}Be problem

As written in the subsection above, all four solar neutrino experiments observe solar neutrino rates far below the expectation from the SSM. A summary comparison is shown in figure 2–8. The fluxes of pp and pep neutrinos are considered to be robust since these fluxes are essentially estimated from the solar luminosity, which is determined within ±0.4% accuracy. This flux is calculated with only a 1% uncertainty in standard solar models and the predicted event rate for Ga experiments is 69.6 SNU. On the other side, both Ga experiments indicate that observed solar neutrino event rate ($77.5^{+7.5}_{-7.8}$SNU for GALLEX, $66.6^{+7.8}_{-8.1}$SNU for SAGE) is almost exhausted by pp neutrinos (69.6±0.7SNU) as seen in figure 2–8. The ^{8}B neutrinos observed by Kamiokande also contribute to the Ga experiment measurement. The expected event rate to which ^{8}B neutrinos contribute is calculated using the ^{8}B energy spectrum normalized to the rate observed in Kamiokande. This value is computed to be about 5.4SNU. This means that there is no room for ^{7}Be neutrinos which ought to be observed at a rate of 34.4SNU. ^{7}Be neutrinos are generated by electron capture in ^{7}Be and this capture rate is about 1000 times larger than the reaction rate of (2-9). In order to explain the significant small flux of ^{7}Be neutrinos in standard solar model, the cross section of reaction (2-9) has to be increased by about 2 orders of magnitude, but this cross section is measured with ∼10% accuracy. This discrepancy is shown in figure 2–9 [31]. This figure shows a correlation between the ^{7}Be and ^{8}B neutrino flux ratio

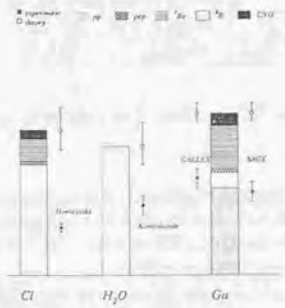

Figure 2–8: The comparison between observation and prediction of solar neutrino event rate (or flux). The contribution of each neutrino sources is also drawn.

of measurement to prediction in the standard solar model. The hatched area is the 90% C.L. allowed region derived from the measurement. The dot-dashed and dot contour means 95% and 99% C.L., respectively. Also shown are the prediction of 1000 Monte Carlo SSM's, various non-standard solar models [3], and the models characterized by a low central temperature and low S_{17}.

2.5 Possible solution for solar neutrino problem

In the previous section, it is found that the solar neutrino problems seem impossible to be solved with modifications of solar models. A possible, and the most plausible, solution to the solar neutrino problems is neutrino flavor oscillation. This would imply that the neutrino has mass and neutrinos of different generations mix. This section briefly describes what neutrino oscillations are.

2.5.1 Vacuum oscillation of neutrino flavor

If neutrinos have mass and different generations mix as quarks do, observed neutrino flavor will change as they propagate. This phenomenon occurs because the propagation eigenstate, namely a mass eigenstate, of a neutrino is not a flavor eigenstate. Currently it is believed that there

[3]Non-standard models are the models which try lowering the ^{8}B neutrino flux by changing parameters unphysically.

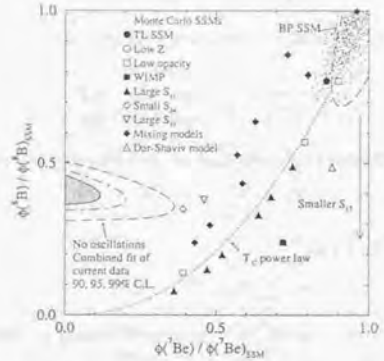

Figure 2–9: This figure shows a correlation between the ^{7}Be and ^{8}B neutrino flux ratio of measurement to prediction for standard solar models [31]. The hatched area is the 90% C.L. allowed region derived from the measurement. The dot-dashed and dot contour means 95% and 99% C.L., respectively. Also shown are the prediction of 1000 Monte Carlo SSM's, various non-standard solar models, and the models characterized by a low central temperature and low S_{17}. For detailed explanation of this figure, see reference [31].

are three kinds of neutrinos, namely, ν_e, ν_μ, and ν_τ. For simplicity, only two flavor oscillations between ν_e and ν_μ is taken into account here.

Mixing between two generations can be expressed as follow:

$$\begin{pmatrix} |\,\nu_e\rangle \\ |\,\nu_\mu\rangle \end{pmatrix} = \begin{pmatrix} \cos\theta & \sin\theta \\ -\sin\theta & \cos\theta \end{pmatrix} \begin{pmatrix} |\,\nu_1\rangle \\ |\,\nu_2\rangle \end{pmatrix} \equiv U \begin{pmatrix} |\,\nu_1\rangle \\ |\,\nu_2\rangle \end{pmatrix} \tag{2-23}$$

where $|\,\nu_{1,2}\rangle$ are the mass eigenstates, θ is the mixing angle, and U is the mixing matrix. From now on, i, j denote 1 or 2 and a, b denote e or μ. The propagation of mass eigenstates is expressed as:

$$|\,\nu_i(t)\rangle = e^{-iE_i t}\,|\,\nu_i(0)\rangle \tag{2-24}$$

where t is the time and E_i is the energy of a neutrino for mass eigenstate i. E_i is approximated as follow,

$$E_i = \sqrt{p^2 + m_i^2} \simeq p + \frac{m_i^2}{2p} \simeq E + \frac{m_i^2}{2E} \tag{2-25}$$

where m_i is the mass of eigenstate i. Equation (2-23) can be rewritten as:

$$|\,\nu_a(t)\rangle = \sum_i U_{ai}\,|\,\nu_i(t)\rangle \tag{2-26}$$

substitution of (2-24) in (2-26) yields:

$$|\,\nu_a(t)\rangle = \sum_i U_{ai} e^{-iE_i t}\,|\,\nu_i(0)\rangle \tag{2-27}$$

$$= \sum_i \sum_b U_{ai} U_{ib}^{-1} e^{-iE_i t}\,|\,\nu_b(0)\rangle \tag{2-28}$$

Therefore, the amplitude that the same flavor is maintained is,

$$\langle \nu_a\,|\,\nu_a(t)\rangle = \sum_i \sum_b U_{ai} U_{ib}^{-1} e^{-iE_i t} \langle \nu_a\,|\,\nu_b(0)\rangle \tag{2-29}$$

$$= \sum_i \sum_b U_{ai} U_{ib}^{-1} e^{-iE_i t} \delta_{ab} \tag{2-30}$$

$$= \sum_i U_{ai} U_{ia}^{-1} e^{-iE_i t} \tag{2-31}$$

The probability that the same flavor is kept, $P(a \to a, t)$, is:

$$P(a \to a, t) = |\,\langle \nu_a\,|\,\nu_a(t)\rangle\,|^2 \tag{2-32}$$

$$= \sum_i \sum_j U_{ai} U_{ia}^{-1} U_{aj} U_{ja}^{-1} e^{-i(E_i - E_j)t} \tag{2-33}$$

Finally substituting equation (2-23) in (2-33) yields:

$$P(a \to a, t) = 1 - \sin^2 2\theta \sin^2 \frac{\Delta m^2}{4E} t \tag{2-34}$$

where $\Delta m^2 = m_2^2 - m_1^2$. Therefore, the probability that an electron neutrino generated at $t = 0$ remains an electron neutrino after time t, or distance L (assuming $t = L$ in natural units) becomes:

$$P(\nu_e \to \nu_e, L) = 1 - \sin^2 2\theta \sin^2 \frac{\pi L}{L_V} \tag{2-35}$$

where

$$L_V = \frac{4\pi E}{\Delta m^2} = 2.48 \frac{E(\mathrm{MeV})}{\Delta m^2(\mathrm{eV}^2)} (m) \tag{2-36}$$

is the oscillation length in the vacuum.

The vacuum oscillation phenomenon is searched for by several experiments which use accelerators or reactors as neutrino source. However, these experiments did not find the phenomenon. Recently, observations of atmospheric neutrinos (which are decay products of mesons (π's, K's, or μ's) created in interactions of primary cosmic rays (protons and nuclei) in the atmosphere), by Super-Kamiokande confirmed that neutrino oscillation does occur between $\nu_\mu \leftrightarrow \nu_\tau$ channel[4]. The atmospheric neutrinos generated on the opposite side of the earth travel about 1×10^4km. Therefore, the observation of 1GeV atmospheric neutrinos has sensitivity for Δm^2 down to $\sim 2.5 \times 10^{-3}\mathrm{eV}^2$. Actually, the observations suggest that non-oscillation is rejected at the 6.2σ level from the zenith angle distribution of neutrino events and the double ratio of muon neutrino and electron neutrino flux of measured to expected, and that the allowed region of Δm^2 is $10^{-3} \sim 10^{-2}\mathrm{eV}^2$ [29].

Another aspect of vacuum oscillation is expected for solar neutrinos, if Δm^2 between ν_e and ν_μ is suitable. The distance between the sun and the earth is about $1.5{\times}10^{11}$m, and typical energy of the ^{8}B neutrinos is about 10MeV, therefore, if the Δm^2 is of order $10^{-10}\mathrm{eV}^2$ and the mixing angle is sufficiently large, a seasonal deviation from the expected value of ν_e flux time variation caused by the elliptical orbit of the earth may be observed. And the shape of the ^{8}B neutrino energy spectrum is distorted due to the energy dependence of the vacuum oscillation length. Since this oscillation is caused by a just agreement of the vacuum oscillation length and the orbital radius, this is called the 'Just-so' solution. In order to verify this solution, high statistical solar neutrino events, hence, massive detectors like Super-Kamiokande are needed.

2.5.2 Neutrino oscillation in matter

Wolfenstein suggested that neutrino oscillations in matter are different from those in vacuum due to an additional potential the ν_e experiences. With analogy to optics, the phase factor of propagation of the neutrino is changed from ipx to $ipn_l x$, where n_l is the index of refraction of flavor l. n_l is represented as follow [30],

$$n_l = 1 + \frac{2\pi N}{p^2} f_l(0) \tag{2-37}$$

[4] or $\nu_\mu \leftrightarrow \nu_s$ channel; where ν_s is sterile neutrino

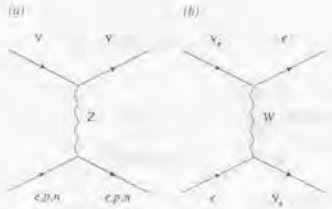

Figure 2–10: The Feynman diagrams of neutrino interaction in matter. Figure (a) shows neutral current interaction via Z boson exchange between a neutrino and an electron, a proton or a neutron. Figure (b) shows charged current interaction via W boson exchange between an electron neutrino and an electron.

where N is the number of density of scatters and $f_l(0)$ is the forward scattering amplitude. An electron, a muon and a tau neutrino interact with an electron, a proton and a neutron via a neutral current interaction. For solar neutrino energy, only electron neutrinos can interact with an electron via a charged current interaction (figure 2–10). This causes the difference in $f_l(0)$ for an electron neutrino from the other type neutrinos, and this additional phase shift causes neutrino oscillation in matter to differ from that in vacuum. Since S.P.Mikheyev, A.Yu.Smirnov applied this theory to the solar neutrino problem, this effect is called the 'MSW effect'. The MSW effect could solve the solar neutrino problems, if $\Delta m^2 \sim 10^{-5}$ and $\sin^2 2\theta \simeq 10^{-3} \sim 1$. In order to explain the MSW effect mathematically, let us consider the propagation of a neutrino in matter. Again, only two flavor eigenstates are considered for simplicity. The time development equation of flavor eigenstates in matter is

$$i\frac{d}{dt}\begin{pmatrix} |\,\nu_e(t)\rangle \\ |\,\nu_\mu(t)\rangle \end{pmatrix} = \left\{ U \begin{pmatrix} E_1 & 0 \\ 0 & E_2 \end{pmatrix} U^{-1} + \begin{pmatrix} V_C + V_N & 0 \\ 0 & V_N \end{pmatrix} \right\} \begin{pmatrix} |\,\nu_e(t)\rangle \\ |\,\nu_\mu(t)\rangle \end{pmatrix} \qquad (2\text{-}38)$$

where V_C and V_N represent the effective potential for neutral and charged current interactions, respectively. The diagonal component of V_N can be absorbed into a common phase, $e^{-i\int V_N dt}$. V_C is calculated to be $\sqrt{2}G_F N_e$, where G_F is the Fermi coupling constant and N_e is the electron

density. Equation (2-38) is rewritten,

$$i\frac{d}{dt}\begin{pmatrix} |\,\nu_e(t)\rangle \\ |\,\nu_\mu(t)\rangle \end{pmatrix} = \frac{1}{2E}\left\{ \frac{1}{2}(m_1^2 + m_2^2 + A)I + \frac{1}{2}\begin{pmatrix} -\Delta m^2\cos 2\theta + A & \Delta m^2 \sin 2\theta \\ \Delta m^2 \sin 2\theta & \Delta m^2 \cos 2\theta - A \end{pmatrix} \right\} \begin{pmatrix} |\,\nu_e(t)\rangle \\ |\,\nu_\mu(t)\rangle \end{pmatrix} \qquad (2\text{-}39)$$

where $A = 2\sqrt{2}G_F N_e E$ and I is the 2×2 unit matrix. Eigenvalues of the matrix are regarded as effective masses of two mass eigenstates in matter. The eigenvalues are

$$m_{im}^2 = \frac{m_1^2 + m_2^2 + A}{2} \pm \frac{1}{2}\sqrt{(\Delta m^2 \cos 2\theta - A)^2 + \Delta m^4 \sin^2 2\theta} \qquad (i = 1, 2) \qquad (2\text{-}40)$$

and the eigenstate in matter is

$$\begin{pmatrix} |\,\nu_{1m}\rangle \\ |\,\nu_{2m}\rangle \end{pmatrix} = \begin{pmatrix} \cos\theta_m & -\sin\theta_m \\ \sin\theta_m & \cos\theta_m \end{pmatrix} \begin{pmatrix} |\,\nu_e\rangle \\ |\,\nu_\mu\rangle \end{pmatrix} \qquad (2\text{-}41)$$

where θ_m is the effective mixing angle in matter and given by,

$$\tan 2\theta_m = \frac{\tan 2\theta}{1 - \dfrac{L_V}{L_e \cos 2\theta}} \qquad (2\text{-}42)$$

with $L_e = \sqrt{2}\pi/GN_e$. Thus, if the following relation is satisfied, the mixing angle in matter becomes maximal ($\theta_m = \pi/4$) even if the vacuum mixing angle is small.

$$L_V = L_e \cos 2\theta \qquad \text{or} \qquad \Delta m^2 \cos 2\theta = 2\sqrt{2}G_F N_e E \qquad (2\text{-}43)$$

This condition is called 'resonance condition'. The electron density at which the resonant condition is satisfied is denoted as $N_{e,res} \equiv \Delta m^2 \cos 2\theta / 2\sqrt{2}G_F E$.

Let us consider solar neutrinos. As shown in figure 2–3, the electron density varies as a function of solar radius. It is largest in the center where nuclear fusion happens and it decreases as the radius increases. Therefore, a neutrino with energy larger than the critical energy E_{crit}, always passes through a position where resonance condition is satisfied. The critical energy is given by:

$$E_{crit} = \frac{\Delta m^2 \cos 2\theta}{2\sqrt{2}G_F N_{e,c}} = 6.6 \cos 2\theta \left(\frac{\Delta m^2}{10^{-4}\mathrm{eV}^2}\right) \mathrm{MeV} \qquad (2\text{-}44)$$

where $N_{e,c}$ is the electron density in the center of the sun. Figure 2–11 shows the mass eigenvalues of two neutrino mass eigenstates in matter as a function of electron density. If the energy of a neutrino is greater than E_{crit}, $\theta_m \cong \pi/2$ from equation (2-42), hence, $|\,\nu_e\rangle$ is almost $|\,\nu_2\rangle$. While the mass eigenstates propagate from the center of the sun to the surface of it, the mass of the eigenstates changes as shown in figure 2–11. When a neutrino passes the resonance region,

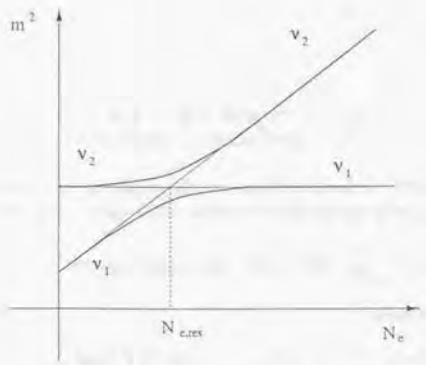

Figure 2–11: MSW effect in the sun.

θ_m becomes $\pi/4$ and the mixing becomes maximal. If the variation of the electron density is reasonable (see eq(2-46)), the main component of flavor $\mid \nu_2\rangle$ state changes from $\mid \nu_e\rangle$ to $\mid \nu_\mu\rangle$ adiabatically, if the vacuum mixing angle θ is small enough. Therefore, a neutrino which is produced as an electron neutrino becomes a muon neutrino when it reaches the surface where the electron density is almost zero. The condition which allows the transition of neutrino flavor from ν_e to ν_μ adiabatically is called adiabatic condition.

Actually, level jumping from $\mid \nu_2\rangle$ to $\mid \nu_1\rangle$ occurs. The probability of this jump, P_{jump}, is approximately calculated by L.D.Landau and C.Zener [46],

$$P_{jump} = \exp\left(-\frac{\pi}{4}\frac{\sin^2 2\theta}{E\cos 2\theta}\frac{\Delta m^2}{\left|\frac{1}{N_e}\frac{dN_e}{dr}\right|}\right) \tag{2-45}$$

The adiabatic condition holds if $P_{jump} \ll 1$, namely,

$$\sin^2 2\theta \Delta m^2 \geq E\cos 2\theta \left|\frac{1}{N_e}\frac{dN_e}{dr}\right| \tag{2-46}$$

Figure 2–12 shows the example of the MSW effect in the sun, where $E/\Delta m^2$ and $\sin^2 2\theta$ are 6.0×10^5 and 0.001, respectively. As shown in figure 2–12, the resonance occurs at $R/R_\odot \simeq 0.3$ and it is found that ν_e is converted to ν_μ with about 35% probability.

As the MSW effect for certain parameter range in Δm^2 and $\sin^2 2\theta$ may convert an ν_e into a ν_μ on its way out of the sun, it is possible for part of this parameter range that the ν_μ are converted back to ν_e when passing through the earth. Figure 2–13 shows the electron density

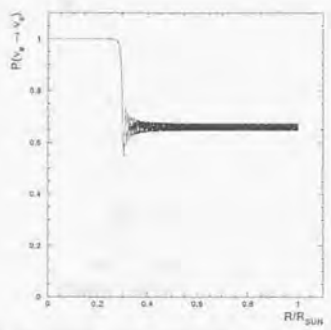

Figure 2–12: Survival probability $P(\nu_e \to \nu_e, L)$ as a function of the solar radius when $E/\Delta m^2 = 6.0\times10^5$ and $\sin^2 2\theta = 0.001$.

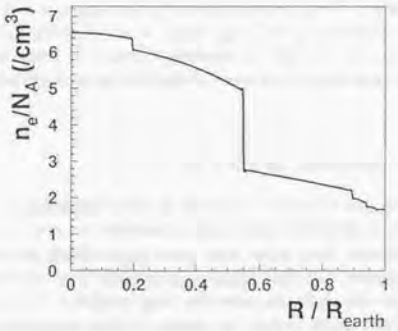

Figure 2–13: The electron density distribution as a function of the radius of the earth[32].

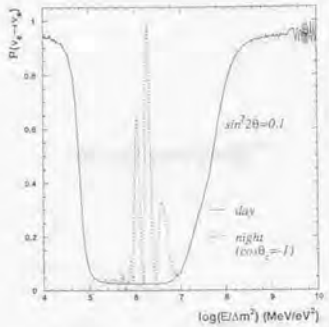

Figure 2–14: The probability $P(\nu_e \to \nu_e)$ at some place on the earth surface is drawn as a function of $\frac{E}{\Delta m^2}$ both for day-time (solid line) and night-time ($\theta_z = 180°$) (broken line), where $\sin^2 2\theta = 0.1$.

distribution as a function of the radius of the earth. This effect leads to the prediction that the observed electron neutrino flux at night when neutrinos go through the earth may be larger than that during the day when the neutrinos come directly from the sun. This is called the 'day-night effect'. Again, like the seasonal effect, in order to study this effect, a high statistics observation is necessary. Figure 2–14 shows the probability $P(\nu_e \to \nu_e)$ distribution as a function of $\frac{E}{\Delta m^2}$ for day-time and night-time ($\theta_z = 0, 180°$, respectively, where θ_z is the zenith angle defined in figure 2–15). The energy dependence of survival probability of ν_e leads to a distortion of energy spectrum.

2.5.3 The feature of neutrino oscillation

In section 2.4, the observations of solar neutrinos by four experiments were described. All experiments suggest that the observed flux of solar electron neutrinos is less than predicted. The assumption that neutrinos have mass and their generations mix and that an electron neutrino produced in the core of the sun converts to another type of neutrino by MSW effect or Just-so oscillation has the capability to solve the solar neutrino problem. The regions of the parameters, Δm^2 and $\sin^2 2\theta$, which satisfy the results of four experiments are limited as seen in figure 2–16. In the MSW region (the upper figure). there are three isolated allowed region. The left side region ($\Delta m^2 \simeq 10^{-5.5}\text{eV}^2$ and $\sin^2 2\theta \simeq 10^{-2}$) is called 'small angle solution' and the right side region ($\Delta m^2 \simeq 10^{-5}$ and $\sin^2 2\theta \simeq 0.6$) is called 'large angle solution'. The lower region ($\Delta m^2 \simeq 10^{-7}\text{eV}^2$ and $\sin^2 2\theta \simeq 0.8$) is called LOW solution. The lower figure shows

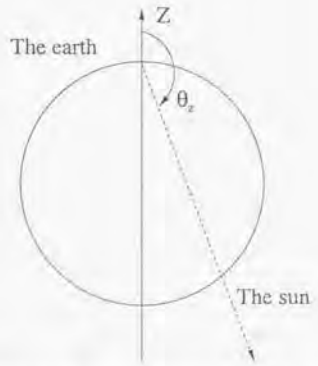

Figure 2–15: The definition of zenith angle

Just-so oscillation solution region ($\Delta m^2 \sim 10^{-10}\text{eV}^2$ and $\sin^2 2\theta \simeq 0.7 \sim 1.0$).

Figure 2–17 shows the ^{8}B neutrino energy spectrum with the distorted spectra caused by the neutrino oscillations in cases of small angle solution ($\Delta m^2 = 5.62 \times 10^{-6}\text{eV}^2$, $\sin^2 2\theta = 6.31 \times 10^{-3}$: broken line) and Just-so solution ($\Delta m^2 = 1.00 \times 10^{-10}\text{eV}^2$, $\sin^2 2\theta = 0.988$: dotted line).

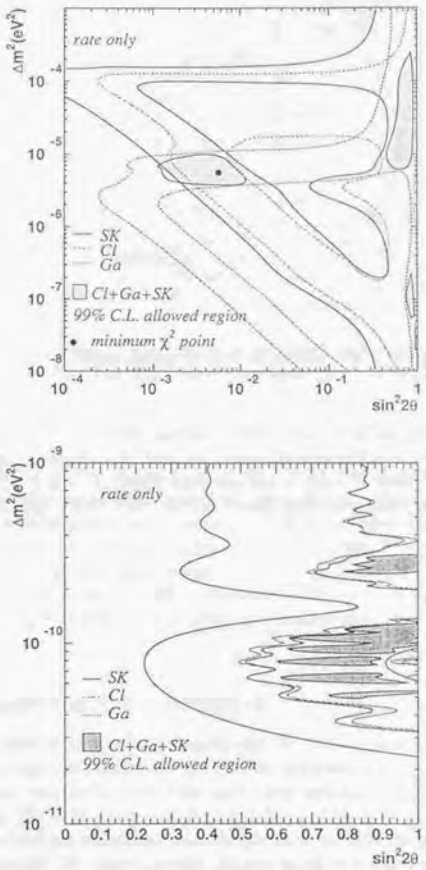

Figure 2–16: The allowed regions of Δm^2 and $\sin^2 2\theta$ which satisfy results of all four experiments. The upper region shows the MSW effect and the lower figure shows the Just-so oscillation region.

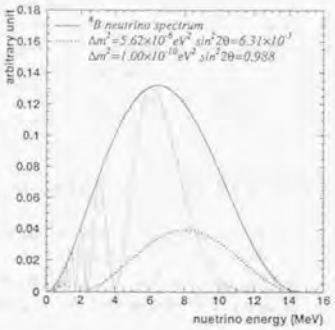

Figure 2–17: ^{8}B neutrino spectra with and without neutrino oscillations. The solid line shows ^{8}B β decay neutrino energy spectrum. The broken and dotted lines are the spectra with neutrino oscillations for small angle solution ($\Delta m^2 = 5.62 \times 10^{-6}\mathrm{eV}^2$, $\sin^2 2\theta = 6.31 \times 10^{-3}$) and Just-so solution ($\Delta m^2 = 1.00 \times 10^{-10}\mathrm{eV}^2$, $\sin^2 2\theta = 0.988$: dotted line), respectively.

Chapter 3

Super-Kamiokande

Super-Kamiokande (Super Kamioka neutrino detection experiment, SK) is an experiment using a water Cherenkov counter. It aims to observe solar neutrinos, atmospheric neutrinos, supernovae neutrinos, and to search for nucleon decays.

In this chapter, a description of SK is given together with the detection method for neutrinos and the Monte Carlo (MC) detector simulation.

3.1 Detection principle for solar neutrinos

When a charged particle having a velocity of v travels in a medium the index of refraction of which is n, Cherenkov photons are emitted if $v > c/n$, where c is the light velocity in vacuum. Cherenkov photons are emitted into a forward cone around the particle track with opening angle of θ measured from the direction of the particle. θ is given by:

$$\cos\theta = \frac{1}{n\beta} \quad (\beta \equiv \frac{v}{c}) \tag{3-1}$$

In the case of pure water, ($n = 1.334$), θ is about 42° for $\beta \simeq 1$. The number of Cherenkov photons (dN) generated in the wavelength interval $d\lambda$ per track length dx is,

$$dN = 2\pi\alpha\left(1 - \frac{1}{n^2\beta^2}\right)\frac{1}{\lambda^2}dxd\lambda \tag{3-2}$$

α is the fine structure constant. The number of Cherenkov photons in the wavelength range of 300~600nm, which is the sensitive region of the PMTs, is about 340 in water per 1cm track length for a charged particle having a unit charge and velocity of $\beta \simeq 1$. The energy threshold for an electron to emit Cherenkov photons is $\frac{n}{\sqrt{n^2-1}}m_e \simeq 0.78\text{MeV}$, where $m_e = 0.511\text{MeV}$ is the rest mass of an electron.

A neutrino interacts with electrons via neutral and charged current interaction:

$$\nu + \mathrm{e} \rightarrow \nu + \mathrm{e} \tag{3-3}$$

The differential cross section $d\sigma_{\nu e}$ of neutrino-electron elastic scattering is given by:

$$\frac{d\sigma_{\nu e}}{dT_e} = \frac{G_F^2 m_e}{2\pi}\left\{A_0 + B_0\left(1 - \frac{T_e}{E_\nu}\right)^2 + C_0\frac{m_e T_e}{E_\nu^2}\right\} \tag{3-4}$$

where T_e is the scattered electron's kinetic energy, E_ν is the incident neutrino energy, $G_F = 1.16636 \times 10^{-11}\text{MeV}^{-2}$ is the Fermi coupling constant. The order of magnitude for the cross section is set by the first coefficient $\frac{G_F^2 m_e}{2\pi} = 4.31\times10^{-45}$ (cm^2/MeV). The parameters, A_0, B_0, C_0 in equation (3-4), are defined as:

$$A_0 = (g_V + g_A)^2, \quad B_0 = (g_V - g_A)^2, \quad C_0 = g_A^2 - g_V^2 \tag{3-5}$$

$$g_V = 2\sin^2\theta_W + \frac{1}{2}, \quad g_A = +\frac{1}{2} \quad \text{for } \nu_e \tag{3-6}$$

$$g_V = 2\sin^2\theta_W - \frac{1}{2}, \quad g_A = -\frac{1}{2} \quad \text{for } \nu_\mu \text{ or } \nu_\tau \tag{3-7}$$

where θ_W is the Weinberg angle and $\sin^2\theta_W = 0.2317$. The total cross section $\sigma_{\nu e}$ is calculated by integrating equation (3-4) for T_e from 0 to T_{max},

$$\begin{aligned}\sigma_{\nu e} &= \int_0^{T_{max}} \frac{d\sigma_{\nu e}}{dT_e} dT_e \\ &= \frac{G_F^2 m_e}{2\pi}\left[A_0 T_{max} + \frac{B_0 E_\nu}{3}\left\{1 - \left(1 - \frac{T_{max}}{E_\nu}\right)^3\right\} + \frac{C_0}{2}\frac{m_e T_{max}^2}{E_\nu^2}\right]\end{aligned} \tag{3-8}$$

where T_{max} is maximum kinetic energy for the recoil electron in (3-3),

$$T_{max} = \frac{E_\nu}{1 + \frac{m_e}{2E_\nu}} \tag{3-9}$$

The differential and total cross sections of ν-e scattering with radiative corrections are calculated by [33]. Some of the Feynman diagrams for the electro-magnetic one loop contributions are drawn in figure 3-1 and 3-2. These corrections reduce the total cross section by about 2%. For the highest energy ^{8}B neutrinos, the cross section is reduced by about 4%. In ν_μ-e scattering there is no contribution from charged current interactions at low energies. Total cross sections for ν_e-e and ν_μ-e scattering with radiative corrections as a function of incident neutrino energy are drawn in figure 3-3. The total cross section for the ν_e-e scattering is about 6 times larger than that for ν_μ-e scattering due to the contribution of the charged current interaction. Hence, if an electron neutrino is converted to another type of neutrino (ν_μ or ν_τ), the event rate of ν-e scattering decreases.

The differential cross section in the case of incident neutrino energy of 10MeV for ν_e+e$\rightarrow\nu_e$+e scattering is shown in figure 3-4 [33].

The recoil electron energy spectrum $F(T_e)$ is calculated to be:

$$F(T_e)dT_e = \left\{\int_0^{E_{\nu,max}} \frac{d\sigma_{\nu e}(E_\nu, T_e)}{dT_e}\phi(E_\nu)dE_\nu\right\} dT_e \tag{3-10}$$

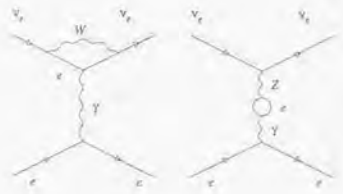

Figure 3-1: Feynman diagrams for one-loop electroweak radiative correction.

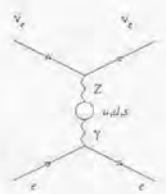

Figure 3-2: A Feynman diagram for one-loop QCD correction

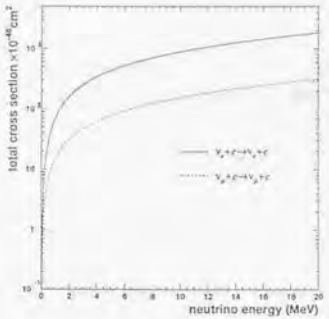

Figure 3–3: Total cross sections for ν_e-e and ν_μ-e scattering as a function of energy of an incident neutrino.

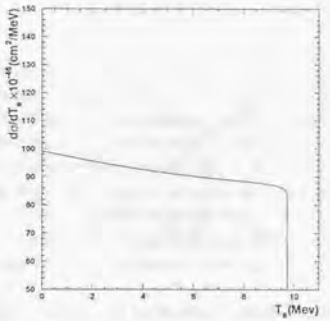

Figure 3–4: Differential cross section of ν_e+e→ ν_e+e scattering for an incident neutrino energy of 10MeV. The horizontal axis is the kinetic energy of a recoil electron.

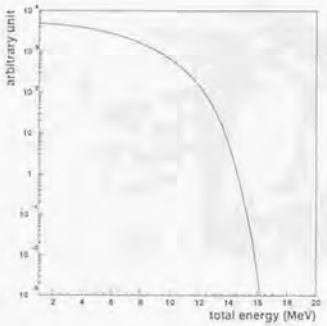

Figure 3–5: The energy spectrum of recoil electrons ^{8}B solar neutrino scattering. The horizontal axis is the total energy of the electrons.

where $\phi(E_\nu)$ is energy spectrum of the neutrinos and $E_{\nu,max}$ is the maximum neutrino energy. In the case of ^{8}B solar neutrinos, the energy spectrum of the recoil electrons is shown in figure 3–5.

The scattering angle θ is determined by the kinematical condition,

$$\cos\theta = \frac{1+\frac{m_e}{E_\nu}}{\sqrt{1+\frac{2m_e}{T_e}}} \tag{3-11}$$

When the neutrino energy is high enough compared with the electron mass, the scattering angle can be approximated by:

$$\theta \leq \sqrt{\frac{2m_e}{T_e}} \tag{3-12}$$

Therefore, the recoil electron keeps the information about incident neutrino's direction. However, because of multiple scattering in the water, the angular resolution is limited to about 27° for an electron energy of 10MeV.

The advantage of using water Cherenkov counters for the observation of solar neutrinos is that the detector can measure the precise time when an electron is scattered, and the energy and direction of the recoil electron. Hence, it is possible to measure how much the electron neutrino flux changes between day and night, or seasonally. Also the energy spectrum of the incident neutrinos can be inferred from the measured energies of the recoil electrons.

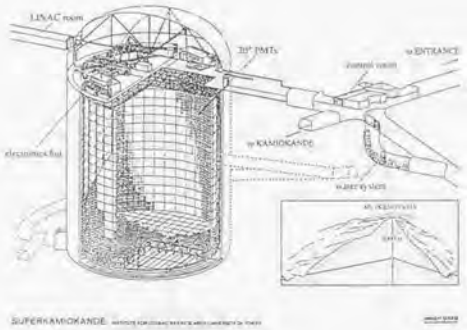

Figure 3–6: Super-kamiokande detector

3.2 The Super-Kamiokande detector

The SK detector consists of a cylindrical stainless steel tank holding 50000t of ultra pure water. The detector is divided into an inner and an outer detector. The water purification plant associated with the detector is located in a tunnel nearby. Figure 3–6 shows the SK detector and how the systems are arranged. The detector is located 36°25'N in latitude, 137°18'E in longitude, about 1000m underground (2700m water equivalent) in Mt. Ikenoyama in Kamioka town, Gifu prefecture, Japan. The 1000m rock reduce the flux of cosmic ray muons, which cause serious background for the observation of neutrinos, by about 5 order of magnitude.

This section describes the details of the SK detector.

3.2.1 Water tank, ID and OD

The cylindrical tank measure 42m in height and 39m in diameter and contains 50000t of ultra pure water. The tank is placed in a cavity of the rock. There is a domed hollow space on the top. It is about 10m high, and houses electronics and calibration systems. The tank is divided into two regions, one is the inner detector (ID) and another is the outer detector (OD). The ID is again a cylindrical volume surrounded on all sides by at least a 2.5m thick OD. ID and OD are separated by a water penetrative light barrier. The size of ID is 36.2m in height and 33.8m in diameter and encloses 32000t of water. 11146 50cm PMTs are evenly distributed over the surface of the ID, 40% of which is covered by their photo-cathodes. The remaining area is covered by black polyethylene terephthalate sheets so as to avoid the reflection of Cherenkov light and the leakage of light from or to the OD. On the back of the structure on which the

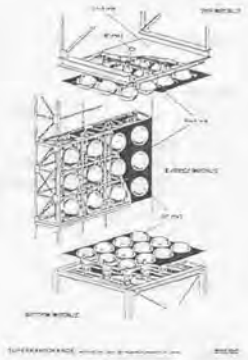

Figure 3–7: The structure of the frame supporting PMTs of ID and OD.

PMTs are mounted (figure 3–7), 1885 20cm PMTs view the surrounding OD. To enhance light collection these PMTs are equipped with square wave length shifter plates (60cm×60cm). The surface of the outer detector is covered with white Tyvek sheet in order to increase reflectivity. The purpose of the OD is to tag and reject any charged particle entering the ID from the outside. The thickness of the OD is 2.6m for top and bottom part, and 2.75m for barrel part. This distance from the rock to the ID corresponds to about 7.6 radiation length and 4.6 nuclear collision length. The PMTs are supported by stainless frame as shown in figure 3–7.

3.2.2 The water purification system

In order to observe solar neutrinos, impurities must be eliminated. They are dust, ions and bacteria causing strong attenuation of the Cherenkov light, and radioactive elements, particularly ^{222}Rn [1], which cause serious backgrounnd below energies of 7MeV. To achieve and maintain the purity of water to the level required for solar neutrino observation, a water purification system is installed. A schematic view of this system is shown in figure 3–8. The air above the purified water also must not contain ^{222}Rn which otherwise would dissolve into the pure water. Hence, a radon-free-air system is also necessary. A schematic view of the radon-free-air system is shown in figure 3–9

The source of water is mine water. The water is first passed through a 1μm filter to remove dust. Next, a heat exchanger removes the heat generated by the circulation pump. Since

[1] ^{222}Rn decays with a half life of 3.8days, ^{214}Bi is produced in it's decay chain. The ^{214}Bi decays via β decay with an emission of an electron whose end point energy is 3.26MeV. This causes serious background for solar neutrino observation.

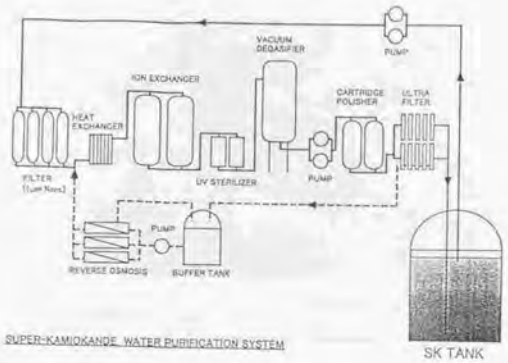

Figure 3–8: The schematic view of water purification system.

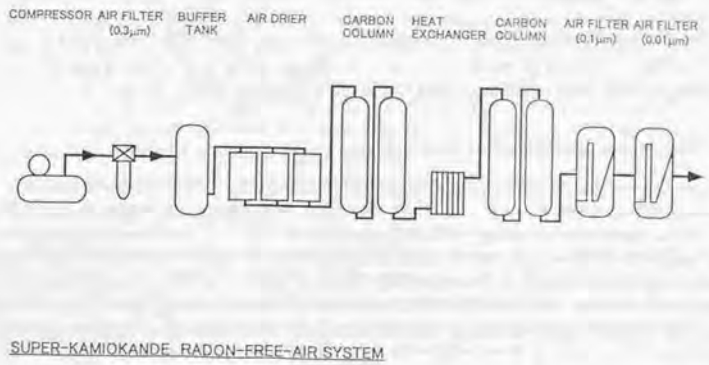

Figure 3–9: The schematic view of Rn free system.

increased temperatures cause bacteria to reproduce, the temperature is always kept at less than 14°C. The ion exchanger removes ions. A UV sterilizer kills bacteria, a vacuum degasifier removes dissolved oxygen and radon gas, cartridge polisher removes ion and heavy elements like uranium and thorium more powerfully. At last, the water passes the ultra filters which remove small dust particles with size greater than ~10nm and divides clean water and dirty water. The clean water is sent to the water tank. The dirty water which contains dust rejected by the ultra filter is stored in a buffer tank, and goes to a reverse osmosis system to remove the dust and cycle through the systems once again. The tank water is continuously circulated through the purification system with the flow rate of 50tons/hour.

The Rn free air is created from mine air. At first, the air is compressed to 7~8.5atm. The air is then sent through an air filter to remove dust particles larger than 0.3μm and stored in a buffer tank. An air drier removes CO_2 and moisture that would decrease the efficiency for rejecting Rn gas in charcoal columns. After the air passes two charcoal columns, 0.1μm and 0.01μm filters remove dust.

The above systems reduce the Rn concentration in the water and the air by a factor of about 10^6 and 10^5 (5.7mBq/m^3 for water[42]), respectively. Since about two months after SK data taking started on April 1st 1996, the transparency of the tank water as well as its radon content remained stable at the anticipated level.

3.2.3 50cm diameter PMT

The Cherenkov photons generated by charged particles which travel in the ID are detected by 11146 50cm-diameter-PMTs. This large PMT was originally developed for Kamiokande by the HAMAMATSU Photonics Company and in collaboration with physicists from the Kamiokande experiment. A schematic view of the PMT is shown in figure 3–10. The PMTs used in SK are improved with respect to those used in Kamiokande: A clear 1 photo-electron (p.e.) peak is now seen in the pulse height spectra (figure 3–11) [41] and the timing resolution (transit time spread) has become better at the 1p.e. level (5nsec→3nsec). These two points are important for the solar neutrino analysis, because the observed number of photo-electrons of each PMT in solar neutrino events is almost always one. This single p.e. efficiency is important for the energy determination while timing resolution at the single p.e. level limits the vertex resolution in the event reconstruction. The improved performance of the PMT is sufficiently adequate for solar neutrino observation at SK.

The glass body of the PMTs is made of Pyrex glass of 5mm thickness which is transparent for light down to 300nm in wavelength. The photo-cathode material is Bialkali (Sb-K-Cs) which is sensitive to light of 280nm~660nm. The quantum efficiency is a maximal 22% at 390nm, a region which is consistent with the wavelength spectrum of Cherenkov light after passing through water. The quantum efficiency curve is drawn in figure 3–12.

The dynode structure is the Venetian blind type with 11 stages. The bleeder circuit is shown in figure 3–13. The high voltage ratios are optimized to increase the collection efficiency for secondary electrons. The rate of dark noise caused by thermal electrons emitted from the photo-cathode is distributed as shown in figure 3–14. The average dark rate is stable around 3.4kHz after the first 2 months from the start of SK. Therefore, in a 200nsec timing window (about the

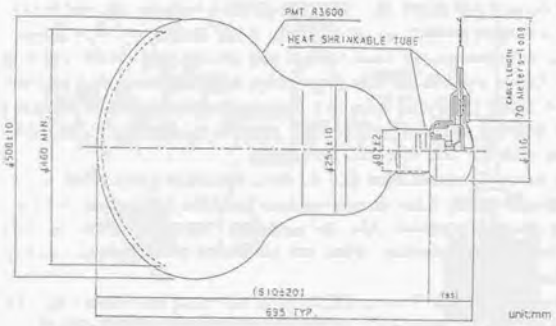

Figure 3–10: A schematic view of the 50cm-PMTs. Dimensions are denoted as mm.

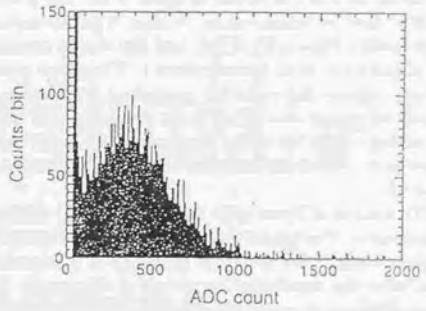

Figure 3–11: 1p.e. distribution of the new 50cm-PMTs.

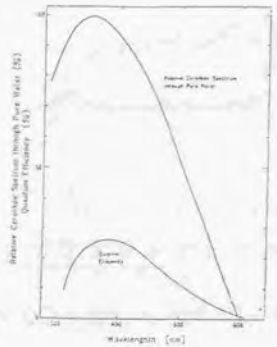

Figure 3–12: The quantum efficiency of the 50cm-PMT. The relative spectrum of Cherenkov photons after passing through pure water is also shown.

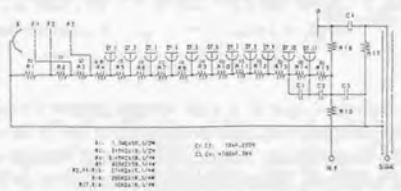

Figure 3–13: The bleeder circuit of the 50cm-PMTs

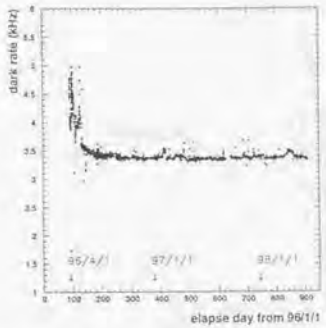

Figure 3–14: The time variation of dark rate.

time a Cherenkov photon needs to travel the diagonal of the detector) about 8 PMTs will have hits from random noise. The PMT is easily affected by an external magnetic field. The mean strength of the geomagnetic field in the tank is about 450mG. In order to compensate the earth magnetic field, Helmholtz coils are wrapped around the tank. Those reduce the magnetic field to about 50mG.

From the start of the observation, some PMTs have died due to a short circuit or other unknown reason. The time variation of the number of dead PMTs is shown in figure 3–15. A decrease of the number of dead PMTs is due to recovery of PMTs which had been candidates of flashing tubes [2]. After more than 2 years operation, the number of dead PMTs is only about 120 (1% of total number of PMTs) and the dead PMTs are distributed uniformly in ID.

The gain G of a PMT is given by,

$$G = aV^b \tag{3-13}$$

where a and $b(b \simeq 8.5)$ are constants, and V is high voltage applied to the PMT. The value of b and the high voltage value which corresponds to the gain of 10^7 were measured by HAMAMATSU for all PMTs. Using these values, one can set the high voltage value so as to get the gain that one wants. To get a uniform detector response, the gain of all PMTs must be equal. For that purpose, a Xe calibration system which is described in chapter 5 is employed. The transit time, which is the time between arrival of a Cherenkov photon on the photo-cathode and output of the electric signal at the anode, depends on the high voltage. A typical value for

[2]There are some PMTs which flash light into the detector and have to be switched off. The reason of its flashing is mainly due to a sparking between dynodes.

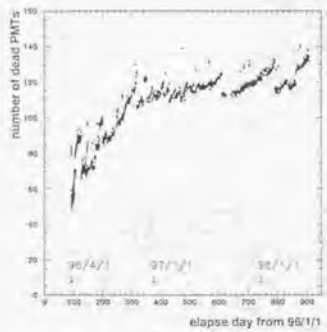

Figure 3–15: The time variation of the number of dead ID PMTs.

the transit time is about 100nsec for a high voltage of 2000V for a gain of 10^7. After adjusting the gain of all PMTs, the high voltage of each PMT is different, as is the transit time. The timing calibration (which net adjusts any delay for individual tubes) is done by a laser system described in chapter 5.

3.2.4 Data acquisition system for inner detector

The signal cables which come from PMTs of ID and OD are extended on the top of the tank, where the electronics systems are located. The analog PMTs signals of timing and charge are digitized. This section describes the electronics and the trigger system for ID readout. An overview of the data acquisition (DAQ) system is shown in figure 3–16.

Front end electronics

The ID PMT signal cables (70m) are fed into ATM (Analog Timing Module) modules in a TKO (Tristan-KEK-Online) system. A TKO crate contains a GONG module (GO NoGO, which distributes control signals as a master module to its slave modules), a SCH module (Super Controller Header, which is a bus-interface module between TKO and VME (Versa Module Europe)), and 20 ATM modules (which digitize analog signals from PMTs for timing and charge information and are controlled as slave modules by GONG). There exist 12 TKO crates in a electronics hut and 4 huts in total. Each electronics hut controls 1/4 of the ID. A central hut houses the trigger electronics. One ATM module handles 12 PMTs, hence, 934 ATMs are used in SK.

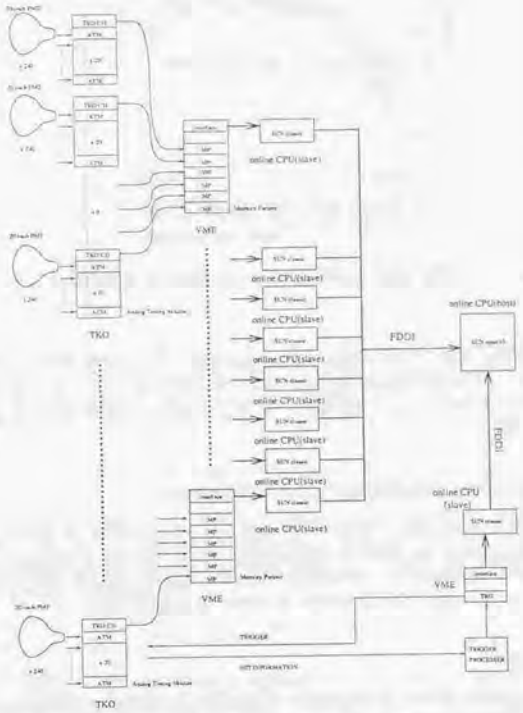

Figure 3–16: An overview over the DAQ system.

	data per 1 channel															
	15	14	13	12	11	10	09	08	07	06	05	04	03	02	01	00
1st word	0	0	event number (8bit)								AB	0	channel			
2nd word	0	1	0	0	TDC data (12bit)											
3rd word	1	0	0	0	ADC data (12bit)											

Table 3–1: The data structure of ATM for 1 channel.

In the first stage of an ATM module [34], the analog signal from a PMT is split into 4. One copy is used for external monitoring of analog signals, another copy is sent to a discriminator after an amplification by a factor 100, and the other copy are sent to the TAC/QAC [35] (Time to Analog Converter, charge to Analog Converter) circuits. If the amplified signal exceeds the threshold level of the discriminator, a rectangular signal of 200nsec width and -15mV amplitude is added to the HITSUM output of the ATM module. From the added output of all ATM modules ID trigger are derived. The threshold of the discriminator is set to the equivalent of 0.2p.e.. The two TAC/QACs for each channel enable the ATM to work dead-time free. This indicates that SK can handle μ-e decay events (the typical time difference is 2.2μsec) or high rate events (i.e. supernovae bursts; about 1kHz in the case of supernovae explosion at the center of the Galaxy). The TAC circuit translates time into an integrated charge, which is proportional to the time difference between the PMT hit and the timing of the global trigger, and the QAC circuit integrates the charge from the PMT within 400nsec. The integrated charges are held by capacitors. If the global trigger signal is not issued within about 1.3μsec after a PMT hit, the integrated charges are discharged automatically. If the global trigger signal is issued, the charges are digitized by an ADC (Analog to Digital Converter), and the digitized data are stored in a 1024 word FIFO (First In/First Out) memory. The ATM provides 1.3μsec full range in time with 0.3nsec resolution and 600pC full range in charge with 0.2pC ($\simeq$0.1p.e.) resolution. The association of a signal to an event is done by an event number. The event number is incremented by a TRG (TRiGger) module in the central hut which issues the global trigger signal, and the event number (16bit) is distributed with the trigger to the electronics huts. The GONG in each TKO crate receives the event number and distributes the lower 8bit of it to the ATMs. The data structure of one signal recorded in the FIFO of the ATM is shown in table 3–1, where AB indicates which of the two TAC/QACs was used and 'channel' is a unique channel number identifying the PMT and its electronics channel.

Trigger system

The all HITSUM signals issued by the ATMs are summed up in each electronics hut with summing modules, and the summed HITSUM signals from the four electronics huts are again summed up in the central hut. In this summation, the pulse height contributions from individual hits drop from -15 to -11 mV. The summed signal is AC-coupled into a discriminator to subtract the changing offset generated by the dark noise rate of the 11146 inner PMTs. A trigger is

Trigger bit	type of trigger
0	LE
1	HE
2	SLE and Fission Trigger(for Ni calibration)
3	OD trigger
4	Periodical Trigger
5	Calibration Trigger
6	Online Veto Start
7	Online Veto Stop

Table 3-2: The trigger ID. Periodical Trigger is a kind of random trigger issued every 6 seconds. Online Veto Start and Stop mark the duration of a possible online veto, which is issued if more than 64 events happen within 120μsec.

issued, when the HITSUM signal exceeds a discriminator threshold. The threshold level is set to -320mV, i.e. if the number of hit PMTs exceeds 29hits in a 200nsec time window, a global trigger is generated. This trigger level is called Low Energy (LE) trigger. The rate at which LE triggers are issued is about 10Hz. There are other kinds of similar triggers named Super Low Energy (SLE) trigger [3] and High Energy (HE) trigger. The trigger thresholds of SLE and HE are -260mV and -340mV, and the event rate of these are 100Hz and 3Hz, respectively. Since the rate of SLE trigger was too high to handle in the offline system, an intelligent online event reduction system is used to reject the events near the wall of ID which dominate the SLE trigger[4]. As a result of this trigger, the event rate from the SLE trigger is reduced to about 16Hz. The OD also generates its own trigger. The threshold of the OD trigger is 19hits in 200nsec time window and the rate is about 3Hz, which is almost entirely due to cosmic ray muons.

The global trigger is then fed to the TRG module (VME specification). The TRG increments the 16 bit event number and distributes the event number signal and the global trigger signal to all GONGs, records the time at which the global trigger was issued using an internal 50MHz 48bit clock. The TRG also records the trigger ID indicating which trigger was issued by an 8bit data word. The identification bit of trigger ID is shown in table 3-2. The method to issue the global trigger is drawn in figure 3-17.

3.2.5 Data acquisition system for outer detector

The DAQ system for the outer detector is completely different. The OD PMT signals are fed to QTC (Charge to Time Converter) module after separation from the positive HV by pickoff cards. The QTC module, which deals with 48 PMT signals and discriminates the signals with

[3]The data taking with SLE trigger started in May 1997

[4]A recent offline computer upgrade would allow to take the full SLE rate.

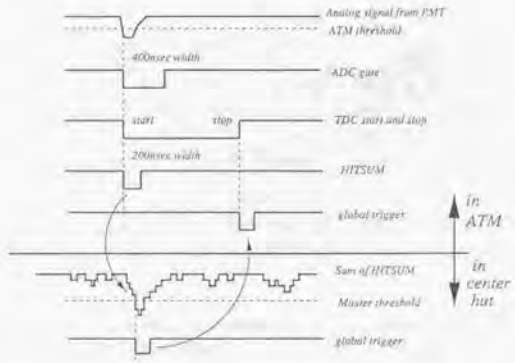

Figure 3-17: Trigger generation.

a threshold of 0.25p.e., generates rectangular pulses. Each pulse is put out with 200nsec delay after a signal comes and the width of the pulse is proportional to the charge integrated within a 200nsec gate. These pulses, which have timing and charge information, are sent to a FASTBUS TDC module. The QTCs also generate HITSUM signals, which are used to generate the outer detector trigger.

If a global trigger is issued, the QTC signals are digitized in the TDC modules. The TDC module, which can handle 96 channels, is able to record for time range of 32μsec. The recording range is tunable relative to the global trigger timing.

The readout of the digitized data is controlled by a FSCC (FASTBUS Smart Crate Controller). The data are sent to a DC2-DM115, which latches the TDC data into its memory, and written into a DPM (Dual Ported Memory) modules which plays a role like SMPs (see following section) in the DAQ of the ID. Finally the data are read out by a workstation.

3.2.6 The ID online system

The digitized PMTs data stored in the FIFO of the ATMs are read out through the SCH by a SMP (Super Memory Partner, VME specification), which possesses 2Mbyte internal memory. One SMP collects the data from one TKO crate in the fixed format shown in table 3-3. The data size per one channel is 12 bytes. Six SMPs are controlled by one workstation, S4/CL (Sun SPARCclassic), which is called 'slave machine'. There are 8 slave machines and each electronics hut has 2. Therefore, one slave machine controls the data from about 1400 PMTs. The 6 SMPs' data are read out by block transfer. The data of all slave machines are sent to a workstation, S4/10 (Sun SPARCstation 10), called 'host machine' via FDDI (high speed ring network with

address	data		
	31·····16	15·····0	
1	0000	16 bit event number	GONG
2	Module address	channel and 8bit event counter	ATM
3	Module address	TDC data	ATM
4	Module address	ADC data	ATM
5	Module address	channel and 8bit event counter	ATM
·	···	···	ATM

Table 3–3: The data format of SMP. The right side line means the origin of data. Module address is the address of an ATM in a TKO crate. 'address' is the data address in SMP.

optical fiber cable). The TRG is controlled by another workstation, S4/CL, called the 'trigger machine', and information related to the trigger are sent to the host machine through it. Yet another workstation, a S4/20 (Sun SPARCstation 20) collecting OD data, is called an 'anti slave', and its data are sent to the host machine via FDDI. The host machine builds the event from the slave machines on the basis of the event counter information. The reconstructed data are sent on to another workstation (UltraSPARC, 'reformat machine'), which changes the online format to an offline format (ZBS, Zebra Bank System), which is easy to handle in the analysis.

A workstation called 'Supernovae watcher' monitors the data stream for Supernovae events. If a Supernovae candidate is found, this machine analyzes the data immediately and notifies the shift people.

The workstation called 'slow control machine' monitors the the detector environment such as temperature in the electronics huts, the output of TKO power supplies, the current of the compensating coils, and the high voltage values of all PMTs, ID and OD. On the reformat machine, a process called 'Badsel' checks for dead PMTs and monitors the hit rate of all PMTs.

After reformat process finished, the data are sent via optical fiber to the offline computer system which is outside of the mine. The transfer rate of reformatted data is about 100Mbyte/10minutes.

3.2.7 The Offline system

The reformatted data are sent to the offline computer system. The system is composed of a VPX2105 called 'sukop' and 10 S4/20 workstations called 'sukeve(1~10)' with a MTL (Magnetic Tape Library) system, which has a capacity of 12Tbyte (until January of 1998). Since February 1998, the system is completely replaced. A summary of the replacement is tabulated in table 3–4. PetaSite made by SONY can store about 100Tbyte of data and the flow rate of data read out is enlarged 14 times as compared to the old MTL system (from 10.8MByte/s to 144Mbyte/s). The total computational power of sukop and sukeve is improved about 20 times.

The sukop machine transforms the ADC and TDC counts of the ATM data to the real charge (pC) and time (nsec), respectively, using the tables provided by various detector and

	~Jan,1998	Feb,1998~
Data Storage system	MTL	PetaSite
sukop	VPX2105	StarFire
sukeve	S4/20	AP3000

Table 3–4: A summary of the replacement of the offline system

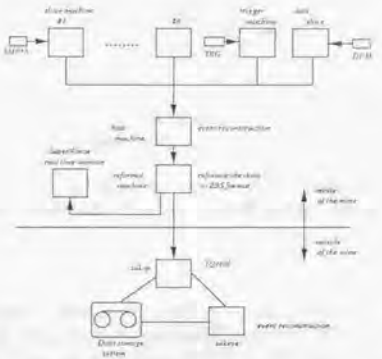

Figure 3–18: The summary figure of on and offline system.

electronics calibration. This process is called 'TQreal'. The size of data with real charge and time is 27Gbyte/day. These data are distributed to the 10 sukeve machines, on which the reconstruction of events (vertex, direction, energy, etc) are carried out for solar neutrino, atmospheric neutrino, and up-going muon events.

After reconstruction, these data are recorded on the Data Storage system. The data size for solar neutrino analysis is about 5G byte/day.

A figure summarizing the online and offline system is shown in figure 3–18.

3.3 Detector simulation

In order to investigate solar neutrino physics, the detector response for solar neutrino events has to be known. In order to understand the detector response, a Monte Carol (MC) simulation of the detector is carried out. The simulation program is based on GEANT which is developed at CERN (European laboratory for particle physics). The program reproduces the behavior of

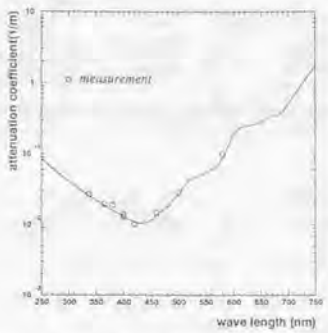

Figure 3–19: The water attenuation coefficient for the water in SK tank which is calculated from the tuned parameter. Open marks are the measured value (see chapter 5).

electrons and photons in materials faithfully with the consideration of physical processes such as Coulomb multiple scattering, ionization loss, bremsstrahlung, etc. for electrons, and Compton scattering, pair creation, etc. for photons in energy range of a few keV to a few TeV.

In the SK detector simulation, the production and propagation of Cherenkov photons generated by recoil electrons have to be considered also [36]. The production of these is based on equation (3-2). The propagation of these is slightly complicated. When the Cherenkov photons travel in water, they suffer Rayleigh scattering and absorption. Rayleigh scattering is dominated for short wavelength ($\lambda \leq$400nm) due to wavelength dependence of $\propto 1/\lambda^4$, and the absorption effect is dominant for long wavelength ($\lambda \geq$ 400nm). These effects are related to the water attenuation length. The theoretical wavelength dependence of Rayleigh scattering and absorption are calculated [37] separately, however, the magnitude of these effects is not known since these factors depend on the purity of water. Therefore, these parameters are tuned in the MC. These parameters with a collection factor (described later) are turned so that the simulation of the LINAC calibration (see chapter 5) reproduces the real data. In figure 3–19, the wavelength dependence of attenuation coefficient for light in the water in SK, which is calculated from the tuned parameters, is shown together with the results of a direct measurement[5].

The speed of Cherenkov light in water depends on the wavelength. The speed is the group

[5]A description of this direct measurement is given in chapter 5.

parameter	value
λ_a^2	0.018085
a_1	5.743534×10^{-3}
a_2	1.769238
a_3	-2.797222×10^{-2}
a_4	8.715348×10^{-3}
a_5	-1.413942×10^{-3}

Table 3–5: The values of parameters in equation (3-15).

velocity v_g which is given by:

$$v_g = \frac{c}{n(\lambda) - \lambda\frac{dn(\lambda)}{d\lambda}} \tag{3-14}$$

where $n(\lambda)$ is index of refraction as a function of wavelength λ and is parameterized as [38]:

$$n(\lambda) = \sqrt{\frac{a_1}{\lambda^2 - \lambda_a^2} + a_2 + a_3\lambda^2 + a_4\lambda^4 + a_5\lambda^6} \tag{3-15}$$

The unit of λ is μm and the parameters are tabulated in table 3–5. These values were obtained by fitting equation (3-15) to the results of measurements. This index of refraction and group velocity is also put into the detector simulation.

The Cherenkov photons are reflected by the surface of PMTs and black sheet. The reflectivities of PMT and black sheet are calculated under the law of optics[6] and the results are again put into the simulation. The polarization of Cherenkov photon is considered at the reflection step. The reflectivities of the PMT and black sheet are shown in figure 3–20 for p-wave and s-wave and the average of both polarization.

The PMT response to Cherenkov photons has to be considered. To begin with, the wavelength dependence of the quantum efficiency (see figure 3–12), which was measured by HAMAMATSU, is taken into account. For a solar neutrino event, most PMTs are given only 1 photo-electron, therefore it is important to know the output charge distribution of a PMT which is given by a single photo-electron, in order to choose the threshold on the analog signals at the ATM. This distribution is measured using the Ni-Cf source (Ni calibration, see appendix A). A typical distribution of output charges in response to single photo-electron hits is shown in figure 3–21. The output charge in the MC simulation is determined by random number distribution of figure 3–21. The time resolution of a PMT is also taken into account. The resolution is calibrated using the vertex resolution of LINAC data.

[6]The structure of the surface of a PMT is composed of 4mm thickness glass ($n = 1.47$) and 20nm thickness bi-alkali ($n = 3.50$)and the layer of bi-alkali is inside of the glass layer. The index of refraction of black sheet (polyethylene) is 1.6.

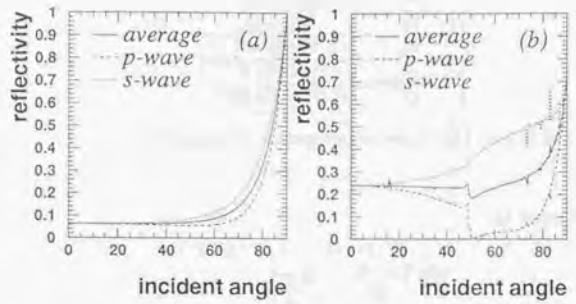

Figure 3–20: The reflectivity of the PMT and black sheet. Figure(a) is for black sheet and (b) for the PMT. The horizontal axis of each figure is the incident angle (degree) and the vertical axis is reflectivity.

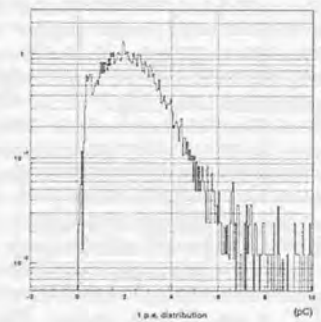

Figure 3–21: The charge distribution of a PMT after a single photo-electron hit.

Finally, the contribution of the dark noise is taken into account. PMT dark noise is simulated by distributing random hits according to the observed average dark rate of the ID PMTs. The charge for these hits is distributed according to the single photo-electron distribution. The dynode collection efficiency, which is the probability that an electron generated by the photo-electric effect reaches the dynode, is not known. Accordingly, this factor is also tuned in the MC simulation.

The ID-PMTs have two kinds of after-pulses. One after-pulse arrives about 15μsec after the signal. This kind of after-pulse happens when a large amount of Cherenkov photons (greater than 400p.e.) hit the PMT. The reason is that the many electrons generated by the photons ionize the remaining gas in the PMT on their way from cathode to dynode. The ions move to the cathode with a smaller velocity due to their large mass, and many electrons are generated again when the ions hit the cathode. Another after-pulse, which is more serious for solar neutrino observation, arrives about 100nsec after signal. This after-pulse is caused by an electron which is scattered by the first dynode elastically and goes back to the dynode with a time lag. As a result, the timing response of the PMT can be delayed by about 100nsec. In the detector simulation, this after-pulse is generated with 2% probability, which is measured by LINAC and Ni-Cf calibration, and a time delay which is distributed in a Gaussian of 10nsec width and a mean of 100nsec.

The result of the detector simulation is recorded in the same format as real data, and the same analysis is applied.

Chapter 4

Event reconstruction

In this chapter event reconstruction for the solar neutrino events will be discussed. After an event vertex is found, event direction and energy, which is observable relevant to solar neutrino analysis, can be reconstructed. A brief description of cosmic ray muon reconstruction is also included in view of its relevance to reducing the background to the solar neutrino event sample.

4.1 Vertex reconstruction

Figure 4-1 shows the definition of coordinates in the SK detector. The origin of the coordinate axes is at the center of the detector. The ranges of x and y axes in the ID are -1690cm to $+1690$cm with the constraint of $\sqrt{x^2+y^2} \leq 1690$cm, while z ranges from -1810cm to $+1810$cm. The reconstruction of the vertex where an event happens is based upon the timing information and the positions of PMTs hit by Cherenkov photons. For solar neutrino events, the recoil electron energy is at most 20MeV, hence the traveling length of the electrons is about $\sim$10cm, which can be regarded as point like. Let us denote the time of i-th hit PMT as $T_i(\boldsymbol{x}_i)$, the PMT position as $\boldsymbol{x}_i = (x_i, y_i, z_i)$. In determining the vertex position, only the relative timing of the hit PMTs is important. When an event happens at the potion $\boldsymbol{x}$, the time of flight for the unscattered Cherenkov photon will correspond directly to the distance between vertex and PMT, and a common time $T_i'(\boldsymbol{x}, \boldsymbol{x}_i)$ will be associated with the time of emission of the Cherenkov photons at the vertex, where:

$$T_i'(\boldsymbol{x}, \boldsymbol{x}_i) = T_i(\boldsymbol{x}_i) - \frac{R(\boldsymbol{x}, \boldsymbol{x}_i)}{c'} \tag{4-1}$$

and $R(\boldsymbol{x}, \boldsymbol{x}_i)$ is a distance between $\boldsymbol{x}$ and $\boldsymbol{x}_i$, and c' is the velocity of light in water. Unfortunately, not every hit satisfies this relation due to the scattering in water and reflection on the PMTs and black sheet. Furthermore, the PMTs have dark noise hits. For example, the number of PMTs hit by Cherenkov photons generated by an electron of 10MeV at the center of the detector is about 60, while the number of dark noise hits in the 200nsec time window is about 8. Hence, the first step to search for $\boldsymbol{x}$ is to extract the PMTs which are thought to be hit by Cherenkov photons.

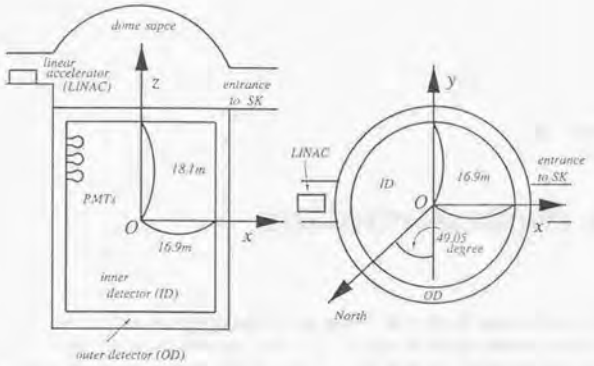

Figure 4–1: The definition of coordinates at SK. The origin O is at the geometric center of the cylindrical detector.

Figure 4–2 shows the display of a typical event. In this figure, the cylindrical ID tank is unfolded (upper left is the unfolded OD) and circles represent the position of hit PMTs. The radii of the circles reflect the magnitude of observed charge. A hazy Cherenkov ring can be seen.

Figure 4–3 shows the absolute times $T_i(\boldsymbol{x}_i)$ distribution of the PMT hits in the event of figure 4–2. The steps to extract the signal PMTs are as follows,

1. Set the location of a 200nsec time window in the time range of figure 4–3 so that it includes a maximal number of the hit PMTs. From here, this time range is called 'on-time' and the outside time range is called 'off-time'. The reason why the range of on-time is 200nsec is same as the reason that the width of the HITSUM signal is set to the time range, namely that this is the time light need to travel the diagonal of the ID.

2. Estimate the level of the PMT dark noise contribution. This contribution is estimated from the number of hits in a fixed time window in off-time, of width Δt_{off}, which is denoted as N_{off}^{bg}.

3. Provide 11 time windows whose time ranges are $\Delta t_{on,n} = 200n/11, \quad (n = 1, 2, \cdots, 11)$ in the on-time, which are set so as to maximize the number of included hits. The number of hits in the n-th window is denoted as $N_{on,n}^{all}$.

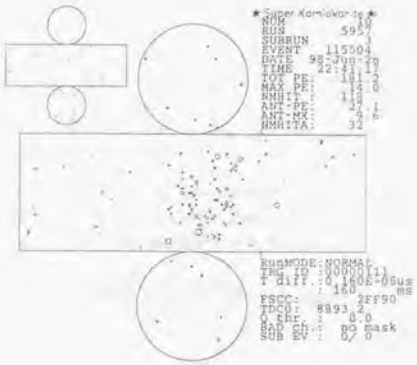

Figure 4–2: The view of a typical event

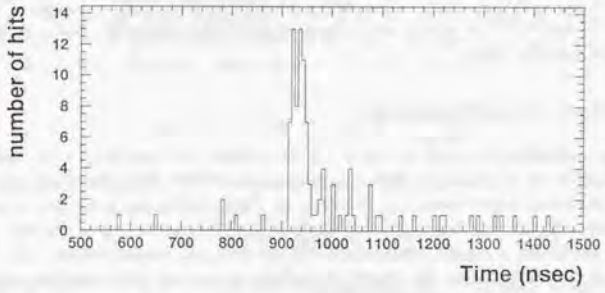

Figure 4–3: The time distribution of the hit PMTs in the event of figure 4–2. The horizontal axis is the absolute time and the unit is nano seconds.

4. Select the time window which maximize a significance S_n defined by:

$$S_n = \frac{N^{sig}_{on,n}}{\sqrt{N^{bg}_{on,n}}} \tag{4-2}$$

$$N^{sig}_{on,n} = N^{all}_{on,n} - N^{bg}_{on,n} \quad N^{bg}_{on,n} = N^{bg}_{off}\frac{\Delta t_{on,n}}{\Delta t_{off}} \tag{4-3}$$

In order to avoid losing signal hits, the widest time window which satisfy $S_n \geq 0.8 S_{max}$ is selected.

The PMTs included in the selected time window are used to reconstruct the vertex.

The reconstruction of the vertex point start with a grid search mapping out uniformly the ID. The vertex point is identified by a maximal goodness g_v, defined as:

$$g_v = \frac{\sum_{i=1}^{N_v} \frac{1}{\sigma^2} \exp\left(-\frac{(T'_i(x,x_i) - T'_c(x))^2}{2\sigma^2}\right)}{\sum_{i=1}^{N_v} \frac{1}{\sigma^2}} \tag{4-4}$$

where N_v is the number of selected PMTs, $T'_c(x)$ is the central value of the distribution of the $T'_i(x,x_i)$, and σ is the time resolution of the PMTs. In the ideal case, all $T'_i(x,x_i)$ are equal, hence, the goodness becomes 1. A typical distribution of the goodness of LINAC[1] calibration events (beam momentum is 10.78MeV/c, an injection point is $x = (-388.9\text{cm}, -70.7\text{cm}, +27\text{cm})$) is shown in figure 4–4. The grid size is about 180cm in the first step and is decreased down to 5cm as the trials approach the final vertex. In figure 4–5, vertex distributions of LINAC calibration at the position $x = (-388.9\text{cm}, -70.7\text{cm}, +27\text{cm})$ with the electron beam momentum of 10.78MeV/c are shown for x, y, z axes. The vertex resolution for an electron energy of 10MeV is about 70cm. The details of the energy dependence of the vertex resolution and a systematic vertex shift will be described later.

4.2 Direction reconstruction

The direction reconstruction is based on the hit PMT pattern. In the ideal case, the event pattern is expected to be a clear ring with opening angle of 42° about the direction of an electron. Again, the scattering in water and reflection on PMTs and black sheet smears out the ring. However, this effect is small compared to effect of multiple scattering of the low energy recoil electron in the water. Actually, the accuracy of the direction reconstruction, namely the angular resolution, is determined by the degree of multiple scattering. The multiple scattering angle θ_{multi}(radian) can be approximated by [39]:

$$\theta_{multi} \simeq \frac{13.6\text{MeV}}{\beta cp}\sqrt{\frac{x}{X_0}} \tag{4-5}$$

[1]The details of the LINAC calibration are described in chapter 5.

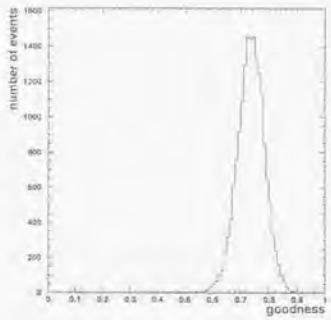

Figure 4–4: The typical distribution of the goodness of LINAC calibration events (beam momentum is 10.78MeV/c, injection point is $x = (-388.9\text{cm}, -70.7\text{cm}, +27\text{cm})$).

where $p, \beta c$ are the momentum, velocity, and $\frac{x}{X_0}$ is the thickness of the scattering medium in radiation length. The radiation length in water is 36.1cm. In the case of electron momentum of 10MeV/c, $\theta_{multi} \simeq 27°$. Hence, angular resolution for the solar neutrino measurements is limited by the multiple scattering.

PMTs hit within a 50nsec time window selected from the TOF (Time-Of-Flight) subtracted $T'_i(x_0, x_i)$ distribution are used to reconstruct the direction of the event. x_0 is the reconstructed vertex position. The reconstruction is done by a maximum likelihood method, i.e. a direction $d = (d_x, d_y, d_z)$ which maximizes logarithm of the likelihood function $L(d)$ is searched for:

$$\log(L(d)) = \sum_{i=1}^{N_{50}} \log\left(f(\cos\theta_i(d))\right)\frac{\cos\theta_i}{a(\cos\theta_i)} \tag{4-6}$$

where N_{50} is the number of PMTs hit in the 50nsec window and:

$$\cos\theta_i(d) = \frac{d\cdot(x_i - x_o)}{|d||(x_i - x_o)|} \tag{4-7}$$

is the angle between the direction d and the direction from the vertex point to the i-th PMT. θ_i is the incident angle of Cherenkov photons to the i-th PMT. The function $f(\cos\theta)$ is a probability density function for the angles into which Cherenkov photons are emitted with respect to the initial direction of a 10MeV electron in MC. It is shown in figure 4–6. In the ideal case, the function $f(\cos\theta)$ has a sharp peak at 42 degree. However, due to the scattering in water and reflection on the PMTs and the black sheet and multiple scattering of the electron, the function

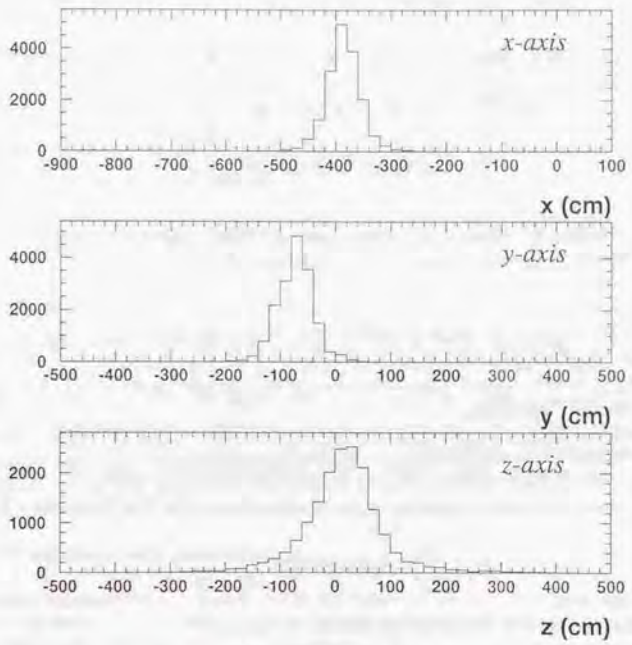

Figure 4–5: Projections of vertex distribution of the LINAC calibration at the position x = (−388.9cm,−70.7cm,+27cm) with the electron beam momentum of 10.78MeV/c.

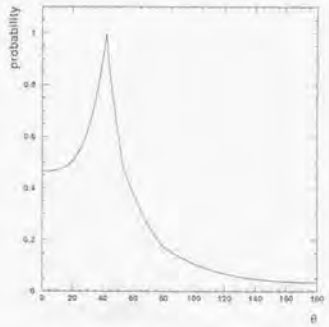

Figure 4–6: The unnormalized probability density function for Cherenkov photon directions with respect to initial electron direction for 10MeV/c electrons.

is smeared out. The function $a(\cos\theta)$ reflects the geometrical acceptance of the respective PMT as seen from the vertex position. This acceptance as a function of the incident angle to the PMT is shown in figure 4–7.

In order to get the direction which maximizes the likelihood function, again a grid search method is employed with the initial direction of the vector sum, $\sum(x_i - x_0)$. The grid size is 20° in the first step, and it decreases down to 1.6° as the likelihood function is nearing its maximum.

The performance of this direction fit is also tested by the LINAC calibration. The LINAC system can only inject electrons into the water tank downward in direction. Figure 4–8 shows the direction distributions projected to x, y, z axis. Figure 4–9 shows the distribution of θ and ϕ, where θ is the angle between the direction of the LINAC beam (downward) and the reconstructed direction, and ϕ is the angle in the plane perpendicular to this direction. The details of the angular resolution of SK detector are described later.

4.3 Energy reconstruction

As indicated in chapter 2, the measurement of the energy spectrum shape is the most important key to investigate the neutrino oscillation with solar neutrinos. Hence, the energy determination has to be done carefully. As discussed earlier, almost all hit PMTs catch only a single photo-electron in a solar neutrino event. The total charge of the event is not a good indicator for the energy of the recoil electron, because charge resolution at the single photo-electron level of

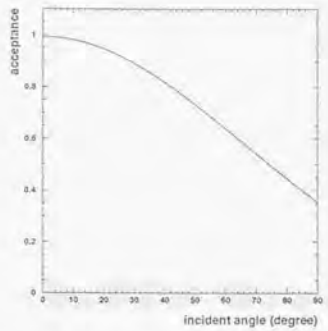

Figure 4–7: The acceptance function of the PMT.

a 50cm-PMT is not good (~50%) enough to estimate the total number of emitted Cherenkov photons. Accordingly, in SK, the energy is calculated from the number of hit PMTs within a 50nsec timing window (N_{50}). However, the number of hit PMTs is still not a good energy indicator, since it has large position dependence[2]. In order to give uniform response over the fiducial volume[3], various corrections are applied. The corrected number of hits, N_{eff}, is defined by:

$$N_{eff} = \sum_{i=1}^{N_{50}} \frac{N_{all}}{N_{alive}} (\alpha_i + \alpha_{tail} - \alpha_{dark}) S(\theta_i, \phi_i) e^{\frac{R(x_0, x_i)}{\lambda}} p_i \qquad (4\text{-}8)$$

The corrections are classified as follows.

Dead PMT correction

In order to reduce the effective difference of the energy scale caused by the variation of the number of available PMTs with time, a factor N_{all}/N_{alive} is used. Here N_{all} is the total number of PMTs in the inner detector of SK (i.e. 11146), and N_{alive} is the number of available PMTs in the detector and the remaining PMTs are dead ones (see figure 3–15).

[2]For example, the measured mean N_{50} using γ-rays from Ni(n,γ)Ni reactions is different by about 10% between the central position ($x = (0, 0, 0)$) and an edge position of the fiducial volume ($x = (0, 0, +16\text{m})$).

[3]The fiducial volume is the inner part of the ID, where the distance from the wall is greater than 2m. It contains 22.5ktons water.

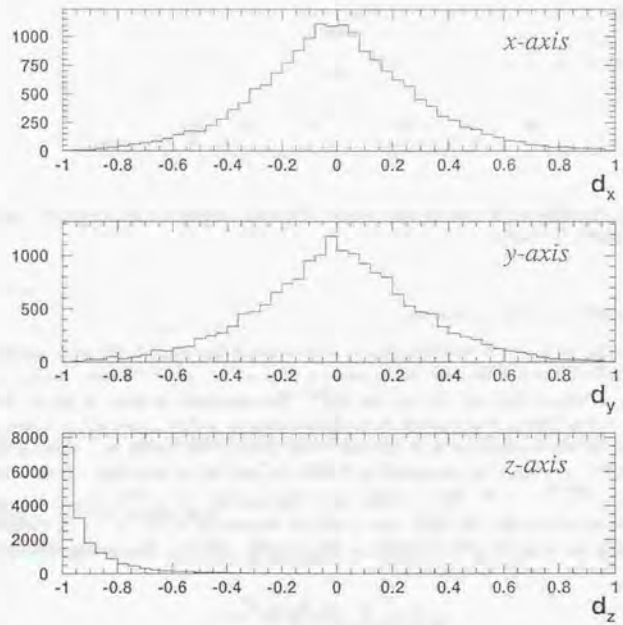

Figure 4–8: The direction distributions projected to the x, y, z axes for 10.78MeV/c electron from the LINAC.

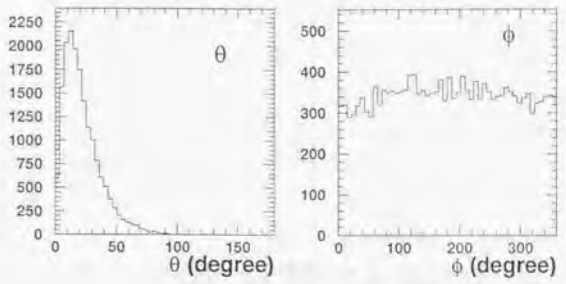

Figure 4–9: Angular distribution along and around the direction of electron injection from the LINAC for 10.78MeV/c electrons.

Multi photo-electron hits correction

If an event happens at near the fiducial volume edge toward the nearest ID wall, an observed number of hit PMTs become effectively small, since a Cherenkov ring of the event become small, which causes multi photo-electron hits on one PMT. The expected number of photo-electrons received by individual PMTs is estimated from the occupancy of the surrounding tubes. If the averaged number of photo-electrons is η_i per one PMT area in the region surrounding the i-th PMT, a probability, A_i, that the surrounding PMTs do not hit is calculated from a Poisson distribution: $A_i = \frac{\eta_i^0 e^{-\eta_i}}{0!} = e^{-\eta_i}$. For a while, when the number of hit PMTs and the number of alive PMTs surrounding the i-th PMT are n_i and N_i (normally $N_i = 3 \times 3 = 9$) respectively, the probability A_i is equal to $(N_i - n_i)/N_i = 1 - n_i/N_i$. Hence, the averaged number of photo-electrons in the area is computed to be:

$$\eta_i = \log\left(\frac{1}{1-\varepsilon_i}\right) \tag{4-9}$$

where $\varepsilon_i = n_i/N_i$. The total number of photo-electrons in the region is $N_i\eta_i$. Therefore, the expected number of photo-electrons received by the i-th PMT, α_i, is given by:

$$\alpha_i = \frac{N_i\eta_i}{n_i} = \frac{\log(1/(1-\varepsilon_i))}{\varepsilon_i} \tag{4-10}$$

If $\varepsilon_i = 1$, we set $\alpha_i = 3$, which is obtained by extrapolating ε_i to 1 in equation (4-10) as shown in figure 4–10.

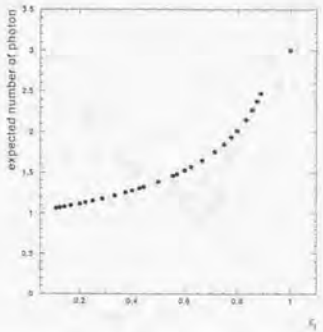

Figure 4–10: The expected number of photo-electrons received by one PMT as a function of ε_i.

Recovery for reflected Cherenkov photons

In order to recover the reflected Cherenkov photons which hit PMTs with a considerable time lag ($\lesssim$ 50nsec), a factor α_{tail} is multiplied, which is defined by:

$$\alpha_{tail} = \frac{N_{100} - N_{50}}{N_{50}} \tag{4-11}$$

where N_{100} is same as N_{50} except that the time window on the TOF subtracted timing is 100nsec.

Correction for dark noise hits

In order to drop contribution of dark noise hits from observed N_{50} [4], a following factor α_{dark} is subtracted:

$$\alpha_{dark} = \frac{N_{alive}R_{dark} \times 100 \cdot 10^{-9}}{N_{50}} \tag{4-12}$$

where R_{dark}(Hz) is the mean dark rate evaluated on a run to run basis (see figure 3–14).

Correction for effective photo-cathode coverage

$S(\theta_i, \phi_i)$ is the effective photo-cathode area from the view of θ_i, ϕ_i direction, where θ_i is the incident angle to the i-th PMT and ϕ_i is the azimuth angle. A ϕ dependence is caused by the arrangement of PMTs as shown in figure 4–11. The function $S(\theta, \phi)$ is shown in figure 4–12.

[4] The dark noise ($\sim$ 3.3kHz) contribute about 2 hits in a 50nsec window.

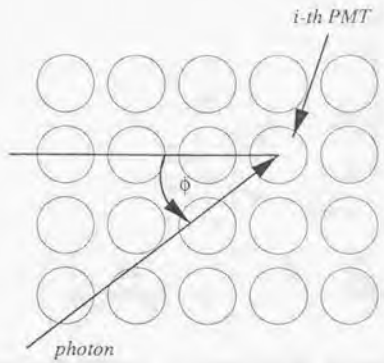

Figure 4–11: The arrangement of PMTs and the definition of the azimuth angle ϕ.

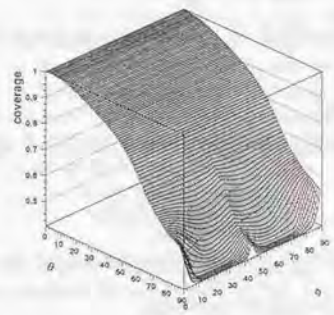

Figure 4–12: Effective photo-cathode area as a function of θ_i, ϕ_i direction.

Water transparency correction

In order to compensates changes in the attenuation of Cherenkov light in water and recovers the associated position dependence of the energy scale, a factor $e^{\frac{R(\vec{x}_0,\vec{x}_i)}{\lambda}}$ is multiplied, where λ is the water transparency measured from the Cherenkov light output of electrons from the decay of stopping muons. It is a function of time. The details of the calculation of λ are described in chapter 5.

Correction for quantum efficiency

The last term p_i is the quantum efficiency correction factor. 375 PMTs were produced in a pre-series to the main PMTs. The quantum efficiency of these PMTs is found to be larger[5]. The factor is given by:

$$p_i = \begin{cases} 0.833 & (375 \text{ PMTs}) \\ 1.000 & \text{the other PMTs} \end{cases} \tag{4-13}$$

The non-uniformity of N_{eff} in the fiducial volume is measured to be $\sim 1\%$ using γ-rays from Ni(n,γ)Ni reaction and monochromatic electron beam (LINAC).

A calculation of an MeV value from N_{eff} is discussed in subsection 5.4.3.

4.4 Reconstruction of cosmic ray muons

Cosmic ray muons are generated by the interactions of the primary cosmic ray particles high in the atmosphere. They penetrate 1000m rock and reach the ID at a rate of about 2Hz. The energetic muons often break ^{16}O nuclei and produce radioactive elements, which decay by emitting electrons or positrons or γ-rays with energies ranging up to about 20MeV. Since the energy of these events is similar to that of the recoil electrons from solar neutrinos, these events (spallation events) become a serious background. In order to reject spallation events, precise reconstruction of the muon tracks is crucial, because the vertex position of spallation events is strongly correlated with the track of the parent muon. In this section, brief explanations of muon fitting and quality of the reconstruction are given.

A muon event is defined as an event where the total number of photo-electrons is greater than 6000p.e.[6] and one PMT exists which recorded a charge greater than 200p.e.. Reconstruction of the muon event proceeds in two steps. The first step is called 'fast reconstruction'. This method finds the entrance point and the exit point of the muon as follows. The entrance position is defined as the position of the PMT which is hit earliest and has more than 2 neighboring hits within 5nsec. The exit point is defined as the center of gravity of the PMTs which detect more than 231p.e. (from now on these PMTs are called 'charge-saturated PMTs'). The track of the muon is the line connecting the entrance and exit points. The success or failure of the first reconstruction method is tested as follows. Two variables are defined: L_{ent}, which is the

[5]This fact was established from the occupancy distribution by Ni calibration measurement. See chapter 5.
[6]For reference, note that if a muon travels 1m in the ID, about 2300p.e. are observed.

minimum distance between each charge-saturated PMT position and the entrance point, and L_{exit}, which is the maximum distance between each charge-saturated PMT position and the exit point. If $L_{ent} > 300$cm and $L_{exit} < 300$cm, the reconstruction is regarded as success. This required condition rejects stopping muons (the muons which stop in the ID) and multiple muon events (more than 2 muons enter the ID at the same time). The events whose reconstruction fails go to the second reconstruction step.

When the number of the charge-saturated PMTs is large, the first reconstruction may have failed. Therefore, events with a residual charge Q_{res} greater than 25,000p.e. are always sent to the second reconstruction step even though the requirements on L_{ent} and L_{exit} in the first step are met. Q_{res} is defined by:

$$Q_{res} = Q_{total} - pL \tag{4-14}$$

and Q_{total} is the total photo-electrons observed in the event, L(cm) is the track length, and $p = 23$p.e./cm is the average number of observed photo-electrons per unit track length for muons.

The second step reconstruction is based on the vertex reconstruction method of solar neutrino events. The difference is that the track of a muon is not point-like. In this reconstruction method, the entrance point is same as that used by the fast reconstruction method and the exit point is searched for so as to maximize the goodness g_μ defined by:

$$g_\mu = \frac{\sum_i \frac{1}{\sigma_i^2} \exp\left\{-\frac{1}{2}\left(\frac{t_i - T}{1.5\sigma_i}\right)^2\right\}}{\sum_i \frac{1}{\sigma_i^2}} \tag{4-15}$$

$$t_i = T_i(x_i) - \frac{l_\mu(x_{exit})}{c} - \frac{l_{photon}(x_{exit})}{c'} \tag{4-16}$$

where x_{exit} is the exit point and T is the arrival time of the muon. $l_\mu(x_{exit})$ and $l_{photon}(x_{exit})$ are defined in figure 4-13. If $L_{ent} > 300$cm, $L_{exit} < 300$cm and $g_\mu > 0.88$, this muon fit is regarded as successful. Events which do not satisfy this condition are regarded as unfitted.

The efficiency of the muon event reconstruction is checked by visual inspection for 1000 muon events. For this purpose, muon events are classified as follows

- single muon events : events which contain only a single muon track
- stopping muon events : muon events stopping in the ID
- hard interaction events : events with $Q_{res} \geq$25000p.e.
- edge clipping events : muons with track length less than 5m
- multiple muon events : events which contain more than or equal to 2 muon tracks

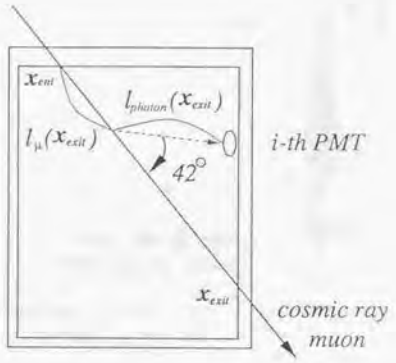

Figure 4-13: The definition of the variables used by the second muon reconstruction.

muon type	number of events	number of unfitted events
single muon	835	5
stopping muon	10	8
hard interaction	41	2
edge clipping	58	19
multiple muon	56	28
total	1000	62

Table 4-1: The fitting efficiency for the classified muon events.

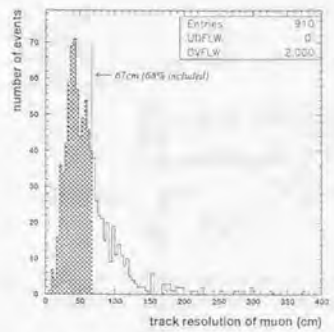

Figure 4-14: The track resolution. The resolution is evaluated to be 67cm.

Table 4-1 summarizes the fitting efficiency. About 6% of the muon events are not fit.

The precision of the muon track reconstruction is evaluated by comparing the results of above fitting and manual fitting, which is carried out by visual scan. This comparison is performed in the following way: (1) calculate the distance between the entrance points obtained by both program and manual fits (d_{ent}), (2) calculate the distance between exit points obtained by both fits (d_{exit}), (3) define the average distance between them ($(d_{ent}+d_{exit})/2 \equiv \overline{d}$). The distribution of $\overline{d}$ is shown in figure 4-14. The track resolution is defined as shown in figure 4-14; i.e. it is the distance which 68% of all entries fill below. It is evaluated to be 67cm.

Chapter 5

Calibration

In this chapter, details and results of the SK detector calibration are given. First of all, the fundamentals of the detector, namely uniformity of gain and timing adjustment for all PMTs, have to be investigated. For that purpose, a Xe light source, a Ni-Cf calibration source and a laser light source are used.

To know the water transparency in the SK tank is also very important, since it directly affects the energy scale. A direct measurement of the water transparency is carried out using a laser light source and a CCD camera. The water transparency depends on the performance of the water purification system. During data taking, the filters of the system were exchanged repeatedly. To monitor the variation, decay electrons from stopping μ are used.

In order to measure the energy spectrum of solar neutrinos, an absolute energy scale is needed that relates the energy of the recoil electrons in SK to the amount of Cherenkov light seen in detector. A liner accelerator for electrons (LINAC) is installed at the detector to calibrate the detector with electrons of energy 5~16MeV. Uniformity of the energy scale in direction and time is investigated by spallation events, the Ni-Cf source and the μ decay electron events.

Angular and vertex resolution measured in the LINAC calibration and the trigger efficiency obtained with the Ni-Cf calibration are also described.

5.1 PMT gain

Uniformity of gain for all PMTs is monitored by two methods, i.e. a Xe light source and a Ni-Cf γ-ray source.

5.1.1 Xe calibration

The gain of all PMTs has to be the same to make detector response uniform. As described in chapter 3, the relative gain of all PMTs is adjustable by changing high voltage $V(10^7$ gain) in equation (3-13). In order to check the relative gain of all PMTs and the stability of gain uniformity, a Xe calibration system is used. Figure 5-1 shows an overview of the Xe light system. An advantage to using a Xe-lamp is that intensity of the output light is stable within

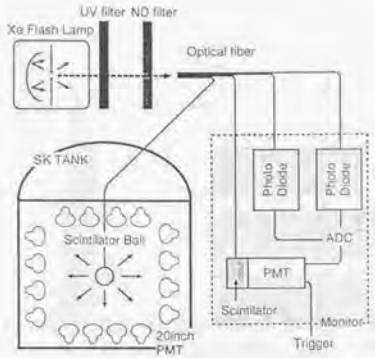

Figure 5–1: Overview of the Xe calibration system.

5%. The light generated by the Xe-lamp go through a UV-pass (Ultra-Violet) filter and an optical fiber and is sent to a scintillator ball in the tank. A role of the UV-pass filter is to pass only ultraviolet light which can be absorbed by the scintillator ball. The scintillator ball is a spherical acrylic ball mixed with BBOT wavelength shifter and MgO. BBOT absorbs the Xe light passing through the UV filter and emit 450nm wavelength light, which is similar to Cherenkov light wavelength. MgO is diffuser to emit the light uniformly. The intensity of the output light is monitored by two silicon photo-diodes and a 5cm PMT.

Charge observed in each PMT is corrected with PMT acceptance, light attenuation in water and non-uniformity of the scintillator ball, which are measured independently. Figure 5–2 shows distribution of the corrected charge for all PMTs. The gain of all PMTs is consistent within 7%. The stability of the overall gain for long time period is also studied and it is found to be stable within 2% for 5 measurements in one year.

5.1.2 Ni-Cf calibration

With the Xe calibration system the gain of all PMTs can be adjusted at large output charge (100~200p.e.). Hence, it is relevant for high energy events, such as cosmic ray muon events. For solar neutrino events, the uniformity for single photo-electron PMT response, namely single p.e. efficiency is essential. For that purpose a Ni-Cf calibration source is used. The source is also used to evaluate the systematic error of vertex reconstruction and obtain trigger efficiency[1]. A more detailed description of the source is given in appendix A.

[1]The Ni-Cf calibration source was also used to calibrate absolute energy before a LINAC calibration was carried out successfully.

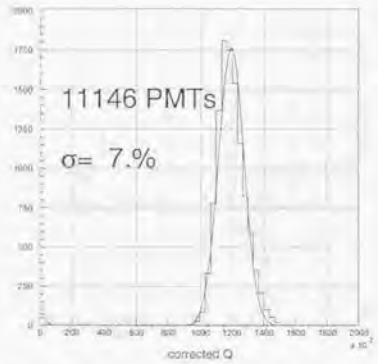

Figure 5–2: The distribution of the corrected charge for all PMTs

The Ni-Cf source emits γ-rays with a maximum energy of 9.00MeV. The γ-rays cause Compton-electrons, which emit Cherenkov photons. In this case, signal on hit PMTs is at the 1p.e. level. Hence, the peak value of the output charge of one PMT indicates the absolute gain. Figure 3–21 shows distribution of the output charge for single photo-electron response of a triggered PMT. Mean value of the distributions for all PMTs is 2.055pC/1p.e..

A parameter indicating the uniformity of the 1p.e. efficiency is represented by the occupancy with a correction for water transparency defined as (number of hits)/(number of total events) for each PMT. Distribution of the averaged occupancy for each layer of barrel part is shown in figure 5–3. Position that the layer number equal one is bottom part and 51 is top part. Figure 5–3 shows a clear increase of the occupancy at the bottom and at the top. This is due to the reflection of light on the PMTs and geometrical condition of the PMT arrangement, and is reproduced in the MC simulation.

The open marks in figure 5–3 are different from the other filled points by about 20%. The reason is that these layers include the PMTs (375PMTs) produced in earlier period which have higher 1p.e. efficiency. The Xe calibration adjusts the gain so that the output charge of all PMTs become same. Therefore high voltage values of these 375 PMTs are set lower. However, the occupancy measured by the Ni-Cf source reveals differences in the 1p.e. efficiency, because 1p.e. efficiency is independent of applied high voltage. The difference in the 1p.e. efficiency is taken into account in the calculation of electron energy as described in equation (4-8).

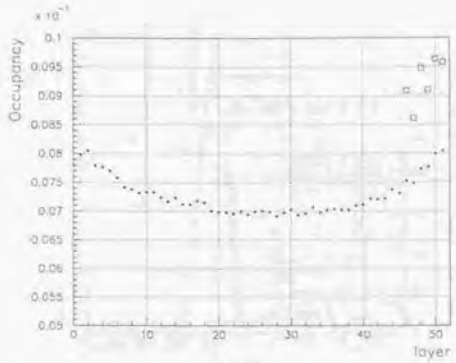

Figure 5–3: Distribution of the averaged occupancy for each layer of the barrel part.

5.2 Timing of PMTs

In order to get vertex position where an event occurs accurately, relative timing and timing resolution of all PMTs have to be known. If the relative timing is different PMT by PMT, an adjustment of the timing have to be performed. To do so, a light source of short time width, ~a few nano seconds, is required. Figure 5–4 shows a schematic view of a laser system which measures the timing response of all PMTs. The light source is a N_2 laser which can produce sufficiently intense light of 337nm wavelength, which width is moderately short (~3nsec).

The wavelength of the generated light is converted to 384nm by a DYE laser. Light intensity is controlled using an attenuation filter. The light is divided into two. One light is sent to a diffuser ball in the water tank through an optical fiber, the other is used for monitoring and triggering. The diffuser ball contains a TiO_2 tip and LUDOX. LUDOX is silica gel with 20nm glass fragments. The tip is located at the center of the LUDOX. The light is diffused by the tip and the LUDOX without an additional timing spread.

By changing the intensity of the light output, the charge dependence of the absolute timing and timing resolution of the PMTs is established. Figure 5–5 shows a so-called 'TQ map', which characterizes the timing response of a PMT. The horizontal axis is the number of observed photo-electrons and the vertical axis is the hit timing. The charge dependence of hit timing is mainly due to slewing in the discriminator on the ATM. The timing resolution also depends on the detected number of photo-electrons. The typical timing resolution for a 1p.e. signal is 3nsec.

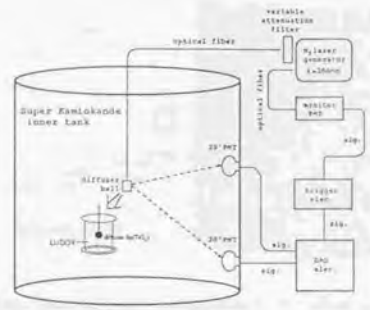

Figure 5–4: The schematic view of the laser system.

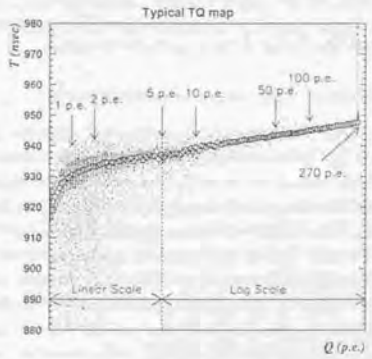

Figure 5–5: The TQ map of one PMT. The details of this figure are described in the text.

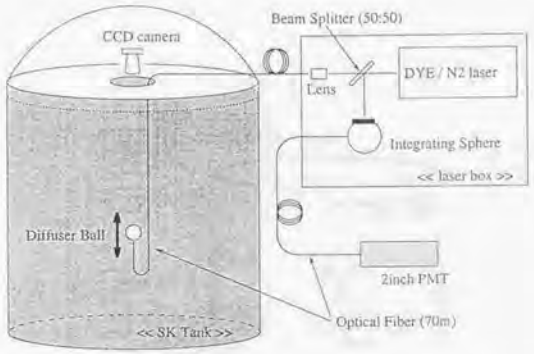

Figure 5–6: System for the direct measurement of the water transparency.

5.3 Water transparency

Water transparency in the SK tank is an important parameter to characterize the response of the detector to the solar neutrino events, since it determines the number of Cherenkov photons which arrive at the PMTs. There are two aspects of the measurement of the water transparency, i.e. one is wavelength dependence which is important for MC simulation in the step of the Cherenkov photon propagation, the other is its long term variation.

5.3.1 Direct measurement of the water transparency

A direct measurement of the water transparency is carried out with the system shown in figure 5–6. Source of light is a N_2 dye laser which is able to produce monochromatic light with wavelengths from 337 to 600nm. The light is split into two, one of which is sent to a diffuser ball in the water tank and the other is used to monitor intensity of the light output through an optical fiber with a 5cm PMT. The diffuser ball is a spherical acrylic ball with MgO. Intensity of the light emerging from the acrylic ball is measured by a CCD camera at the top of the tank. By varying the distance between the diffuser ball and the CCD camera, the water transparency can be extracted without knowledge of the absolute light output of the system. The water transparency λ_{tra} is given by:

$$I(d) = \exp\left(-\frac{d}{\lambda_{tra}}\right) I_0 \qquad (5\text{-}1)$$

where I_0 is the intensity of the light source, $I(d)$ is the measured intensity at the distance of d. Figure 5–7 shows the measured intensity I_{CCD} normalized to the output charge of the

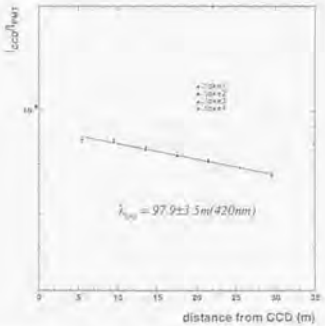

Figure 5–7: The measurement of the water transparency. I_{CCD}/I_{PMT} vs d is shown. The inverse of the slope in the figure is the water transparency; 97.9±3.5m at a wavelength of 420nm. Four different data sets are overlaid (take1∼4).

monitoring PMT I_{PMT} as a function of d at a wavelength of 420nm. The fit result for λ_{tra} is 97.9±3.5m. Figure 3–19 shows water attenuation coefficient defined as $1/\lambda_{tra}$ as a function of the wavelength. The open points are the results of measurements. The line is used in the SK detector MC simulation.

5.3.2 Monitoring water transparency using μ decay electrons

The water transparency is monitored continuously using μ decay electron events. Though this method can only measure the water transparency averaged over the Cherenkov spectrum, the time variation of the water transparency caused by change of filter performance of the water purification system can be measured day by day, since about 1500 μ decay events happen every day. Details of the μ decay electron events are given in appendix C. Figure 5–8 shows a schematic view of how the water transparency is calculated. To begin with, the relevant PMTs, which are within a 50nsec window after TOF subtraction (same as N_{50} defined in chapter 4) and seen under an opening angle with respect to the direction of the decay electron within 32∼52°, are selected. These PMTs are projected onto a sphere with radius R, and the center at the vertex position of the event. On the sphere, these PMTs come to lie on a ring. The ring is divided into 36 equal parts as shown in figure 5–8. The i-th segment on the sphere has effective

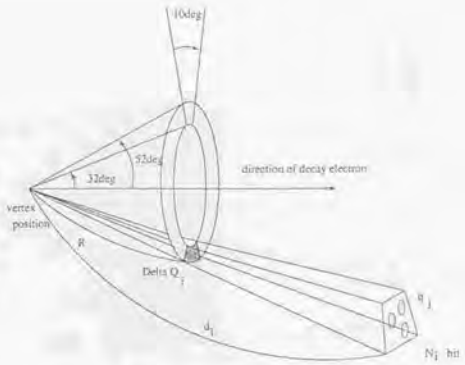

Figure 5–8: The schematic view of how to calculate the water transparency from a μ decay electron event.

charge ΔQ_i:

$$\Delta Q_i = \sum_{j=1}^{N_i} q_j \exp\left(\frac{d_j - R}{\lambda_e}\right) \tag{5-2}$$

where N_i is the number of PMTs included in the i-th segment, q_j is the acceptance corrected charge of the j-th PMT, d_j is the distance from the vertex position to the j-th PMT position, and λ_e is the water transparency to be calculated. In ideal case, all ΔQ_i $(i = 1, 36)$ should be equal:

$$\Delta Q_1 = \Delta Q_2 = \cdots = \Delta Q_{36} = \Delta Q \tag{5-3}$$

Since each segment can be regarded small, equation (5-2) can be rewritten:

$$\Delta Q = \exp\left(\frac{r}{\lambda_e}\right) q(r) \tag{5-4}$$

where $r \equiv \sum_{j=1}^{N_i} d_j/N_i$ is the mean distance, $q(r) \equiv \sum_{j=1}^{N_i} q_j$, and R is set to 0.

ΔQ is different from event to event since the energies of the μ decay electrons are different, following the Michel spectrum. $q(r)$ follows this energy distribution, leading to:

$$\overline{q(r)} = \exp\left(-\frac{r}{\lambda_e}\right) \overline{\Delta Q} \tag{5-5}$$

$$\log(\overline{q(r)}) = -\frac{r}{\lambda_e} + \log(\overline{\Delta Q}) \tag{5-6}$$

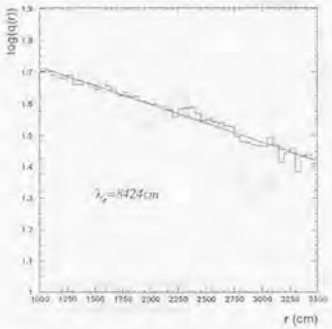

Figure 5–9: This figure shows $\log(\overline{q(r)})$ as a function of r. The slope measures the inverse of λ_e.

where the upper bar means an average over the corresponding variable. From $\log(\overline{q(r)})$ and r, λ_e can be calculated. Figure 5–9 shows $\log(\overline{q(r)})$ as a function of r. The slope is the inverse of λ_e. Figure 5–10 shows the time variation of the water transparency measured by this method. One point corresponds to one week. The first significant increase is due to a replacement of Ultra Filters and another increase is due to an exchange of the 1μm filters. The water transparency for each day is used in the energy calculation of equation (4-8).

5.4 Energy calibration by LINAC

The determination of the absolute energy scale is most important for the measurement of the energy spectrum of the recoil electrons scattered from solar neutrinos. In order to search for possible distortion of the energy spectrum by neutrino oscillations, for example the small angle solution of the MSW effect, the absolute energy must be calibrated with an accuracy of ~1%. A Ni-Cf calibration source was used for the absolute energy calibration at Kamiokande and beginning of SK for solar neutrinos. However it has systematic uncertainties by itself which are large enough to spoil the measurement of the energy spectrum distortion. Details of the Ni-Cf calibration source are described in appendix A. The main sources of uncertainty are the neutron capture cross sections and decay lines of ^{60}Ni and ^{62}Ni. A LINAC (LINear ACcelerator) system which can inject electrons, that energy is similar to that of the recoil electrons, to the detector directly is most suitable for that purpose, since it has smaller systematic uncertainties. In this section, details of the absolute energy calibration with the LINAC are described. Uncertainties

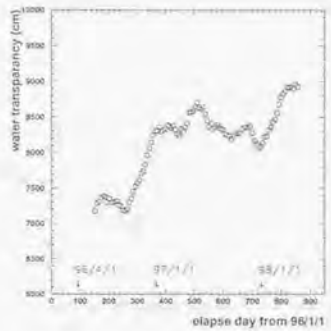

Figure 5–10: Measured time variation of the water transparency.

arising in the LINAC calibration are also discussed. More details of the LINAC calibration are given in [40].

5.4.1 The LINAC system

Figure 5–11 shows an overview of the LINAC calibration system. An electron LINAC is located 4.2m above and 13m away from the water tank in a mine tunnel. The LINAC was used at the hospital of Miyazaki Medical University as a cure for cancer. Electrons from an electron gun, which is specially improved in order to reduce the current to suitable level, allowing that only one electron is injected in to the tank, go through an acceleration tube in which the electrons are accelerated with microwaves of 2μsec width. The frequency of generation of the microwave is adjustable in a range of 10∼66Hz. The broad momentum of the electrons is determined by an input power to the acceleration tube, which is also adjustable. The electron energy range that the LINAC can generate is from 5MeV to 16MeV. Current of the electron beam can be changed by adjusting the output current of the electron gun. The accelerated electrons are bent by a magnet (D1 magnet) at the angle of 15 degrees. The electric current of the D1 magnet selects the momentum of the electrons fundamentally with two collimators near the magnet. Reduction factor of the electron current is about 10^{-6}. The selected electrons go through a beam pipe surrounded by rock as shown in figure 5–11. The rock plays a role to stop γ-rays generated by the collisions of the unselected electrons with the collimators or the beam pipe. By MC simulation, the probability that the γ-rays can penetrate the rock and OD is estimated to be less than 10^{-9}. The electron momentum is further selected by a collimator before the D2 magnet. The momentum spread after this collimator is 0.5% at FWHM. Again many γ-rays are

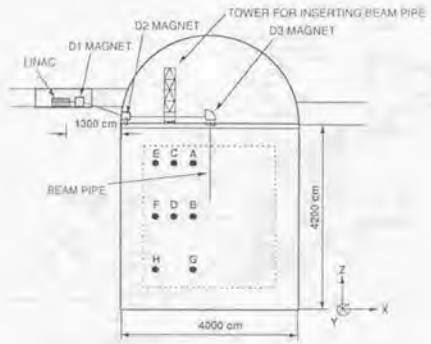

Figure 5–11: The overview of the LINAC calibration system.

generated by this collimator. Lead blocks located under the collimator stop the radiation. The electrons passing thought the collimator are bent 15 degrees back to the horizontal direction by the D2 magnet. The electron beam traveling horizontally on the tank is bent again 90 degrees by the D3 magnet and injected downward to the tank. Quadrupole magnets (Q-magnets) located before and after the D3 magnet focus the electron beam on the end point of the beam pipe. Energy loss by bremsstrahlung at the D3 magnet is negligibly small ($\sim 1.5 \times 10^{-8}$MeV for total energy of 10MeV).

Figure 5–12 shows the structure of the beam pipe end point. In left side in figure 5–12, upper scintillation counters are used for optimizing the beam profile at the end point and as a veto counter. A lower scintillation counter, with radius of 12mm and thickness of 1mm is used as a trigger counter. Last point of the beam pipe is covered by a 100 μm thick titanium window of 15mm radius which partitions the vacuum (10^{-4}∼$^{-5}$ torr) and water.

Electric currents of the D2 and the D3 magnet are set so that the electron beam hit the trigger counter maximumly. The current of the D1 magnet is set to a fixed value, selecting the electron momentum. Q-magnet current is calculated by a MC simulation of beam transportation. The beam intensity is adjusted to 0.1 electron per microwave in order to reduce the injection of more than 2 electrons in the tank water. The beam intensity can be also monitored on the water tank using monitoring scintillation counter located before the D3 magnet. By comparing the beam intensity on the tank and at the end cap, the degree of beam loss can be calculated. The loss gets worse as the beam momentum becomes small (about 80% at 5MeV/c electron momentum). The missing electrons have a possibility to induce a γ-ray background. Discussion related with the background problem is given later.

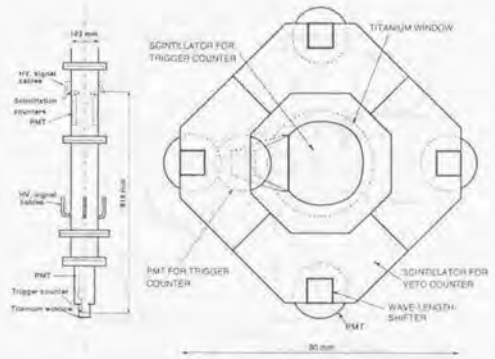

Figure 5–12: The end point of the beam pipe. Left figure shows side view and right figure shows top view.

5.4.2 Beam energy calibration

In order to calibrate the SK detector within 1% accuracy, the precise beam energy has to be known. The beam energy is measured by a Ge detector. The Ge detector has a germanium crystal of 57.5mm diameter and 66.4mm length. Energy resolution of the detector is 1.92keV for the 1.33MeV γ-rays of ^{60}Co. Reading out the output charge of the Ge detector and digitization of it is done by a Multi-Channel-Analyzer. After pulling up the vertical pipe in figure 5–11 and disconnecting the D3 magnet, the end-cap with the trigger counter is connected horizontally just before the D3 magnet. The Ge detector is located just after the end-cap. Relation between deposit energy in the crystal and digital counts is calibrated using γ-rays in energy range from 0.662MeV of ^{137}Cs to 9.000MeV of Ni(n,γ)Ni reaction. Linearity is kept within 0.03% error in the energy range.

The primary purpose of using a Ge detector is to measure energy of not electrons but γ-rays. In a case of electrons, they go through a thin beryllium window, which is the entrance window of it, and inactive region surrounding the Ge crystal before they reach the active region. As a result, the electrons lose some of their energy before being detected. In order to measure the energy loss, the Ge detector was calibrated using an air-core beta spectrometer at the Tanashi-branch of KEK. A view of the spectrometer is shown in figure 5–13. A radioactive element of β-rays used for that purpose is ^{207}Bi. A ^{207}Bi emits a monochromatic electron by internal conversion process with a half life of 38 years. Ratio of momentum spread to momentum $\Delta p/p$ at focus place is about 0.01% [46]. The 975.7 and 1682.2keV electrons are used to calibrate. Figure 5–14 shows comparisons between background subtracted data and MC simulation, where

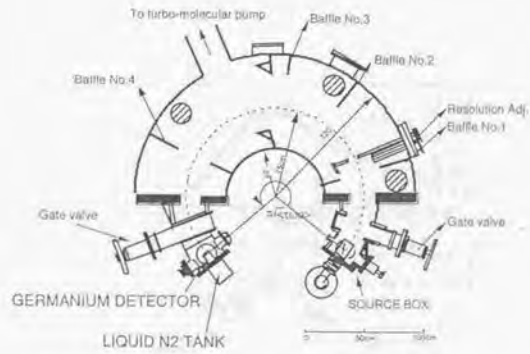

Figure 5–13: A view of the air-core beta spectrometer

the depth of the inactive layer and the thickness of the beryllium window are tuned to be 41μm and 500μm respectively.

With the knowledge of the energy loss at the Ge detector, energies of the electron beam injected into the water tank are measured for various D1 magnet electric current. Table 5–1 lists correlation of the D1 magnet current and the measured energy by the Ge detector. The beam energies in the beam pipe are evaluated by taking into account energy losses of the trigger counter, the Ti window, the Be window and the inactive region by MC simulation. The total energy in SK tank is calculated from the evaluated beam momentum and the energy loss of the trigger counter and the Ti window.

Figure 5–15 shows the energy spectrum measured by the Ge detector for various beam momentum with MC simulation. The measurements were done five times for three x positions. The uncertainty of the beam energy is evaluated by comparing different measurements and estimated to be $\pm$20keV for full width.

5.4.3 Energy calibration of SK detector

The injection of the electron beam to the SK detector was done at 8 positions. List of the 8 positions in terms of the detector coordinates defined in figure 4–1 is shown in table 5–2. A schematic view of the 8 positions is also shown in figure 5–11. At each position, an electron beam is injected with 6$\sim$7 different momenta and about 2×10^4 events hitting the trigger counter are taken. The trigger logic used for the LINAC calibration is drawn in figure 5–16. In order to get the measured energy in the SK detector, at first, events issuing LINAC trigger are selected. Further, multiple electron events, that have more than two electrons injected to the

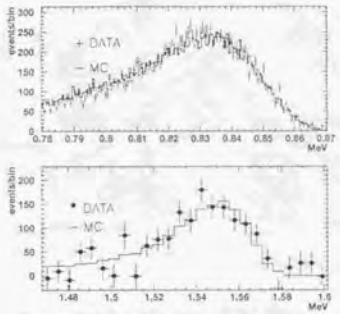

Figure 5–14: The results of the Ge detector calibration using the air-core beta spectrometer with the monochromatic internal conversion electron ray from ^{207}Bi. The upper figure is for 975keV and lower figure is for 1682.2keV electrons.

D1 magnet current (A)	Ge energy (MeV)	beam momentum (MeV/c)	energy in-tank (MeV)
6.0	16.31	15.44	16.09
5.0	13.65	12.80	13.44
4.0	10.99	10.14	10.78
3.2	8.86	8.03	8.67
2.5	7.00	6.17	6.79
2.15	6.03	5.21	5.84
1.8	5.08	4.25	4.89

Table 5–1: The correlation between the D1 magnet current and the measured energy by the Ge detector, the beam momentum in the beam pipe and the total energy in SK water tank.

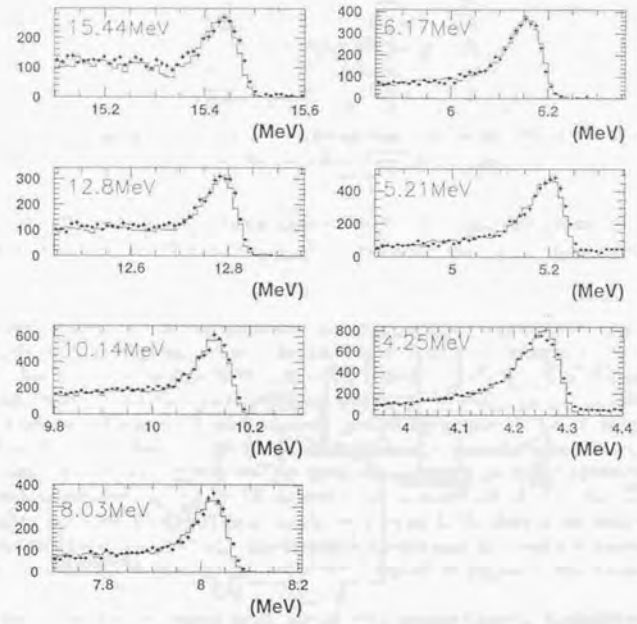

Figure 5–15: The measurement of the beam momentum by the Ge detector. The cross marks are data and histograms are MC simulation.

Position	x(cm)	y(cm)	z(cm)
A	−388.9	−70.7	1228
B	−388.9	−70.7	27
C	−813.1	−70.7	1228
D	−813.1	−70.7	27
E	−1237	−70.7	1228
F	−1237	−70.7	27
G	−388.9	−70.7	−1173
H	−1237	−70.7	−1173

Table 5–2: The list of the positions where LINAC data was taken.

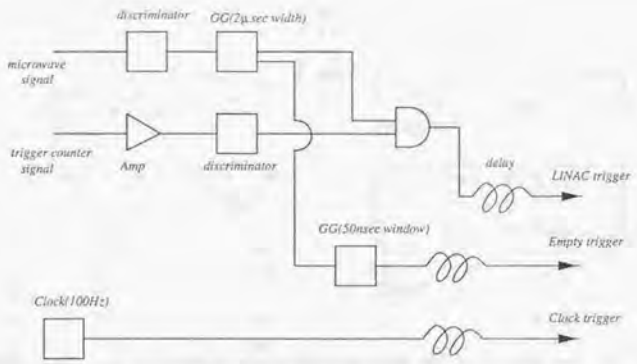

Figure 5–16: The trigger logic for the LINAC calibration. LINAC trigger is used for event selection. The other trigger is for study of beam correlated background.

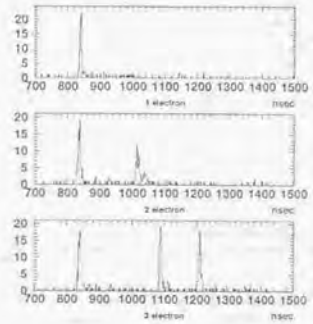

Figure 5–17: The TOF subtracted time distribution for the events selected as one, two, or three electron multiplicity. Each histogram represents one event that is representative of its class.

SK detector accidentally in one event, are rejected. These events can be eliminated easily by counting number of peaks in the TOF subtracted time distribution of the hit PMTs. For example, figure 5–17 shows the TOF subtracted time distributions for the events selected as having one, two, or three electron multiplicity. About 5% LINAC triggered events are dropped by this selection. Figure 5–18 shows scatter plot of reconstructed vertex distribution with histograms of its projections on the x and z axes for finally selected events. The injection point is x=(−388.9cm,−70.7cm,+27cm) and the beam momentum is 16.31MeV/c.

The measurement of the N_{eff} in SK detector is done as follows. At first the measured N_{eff} is plotted to one-dimensional histogram as shown in figure 5–19. Next, a Gaussian fit is applied to the distribution in a range from -1σ to $+2\sigma$.[2] A measured N_{eff} value is defined as a mean value of the Gaussian fit and energy resolution is defined as (sigma of the Gaussian fit)/(the mean).

In order to get absolute energy scale, namely the relation between N_{eff} and total electron energy, a MC simulation is used. A direct correlation between LINAC beam energy and the measured N_{eff} value is not useful for that purpose, because there exists ∼1% non-uniformity of N_{eff} in the fiducial volume and the LINAC calibration is done for only 8 positions with one (downward) direction, and the correlation cannot be easily extrapolated to the total fiducial

[2]Why this asymmetrical region is used to fit is historical reason. At beginning of the LINAC data taking, beam spread at the end point of the beam pipe was worse and lower energy tail affected the measured N_{eff}. In order to reject the effect, the fit range was selected to that range. When the fitting range is changed, the fluctuation of mean N_{eff} is found to be consistent with its statistical error (namely < 0.2%) for the LINAC data used in this description.

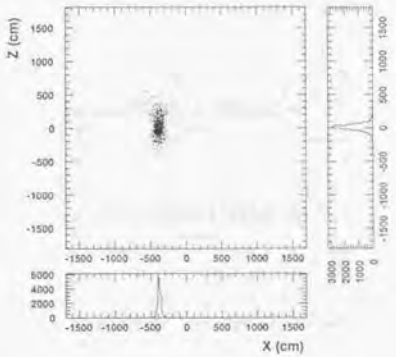

Figure 5–18: The scattered plot of the reconstructed vertex distribution with histograms of its projections on the x and z axes. The injection position is x=(−388.9cm,−70.7cm,+27cm) and the beam momentum is 16.31MeV/c.

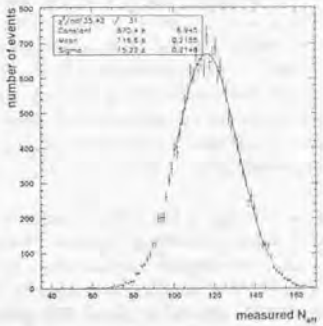

Figure 5–19: The measured N_{eff} distribution in the SK detector at the position of x=(−388.9cm,−70.7cm,+27cm) and beam momentum of 16.31MeV/c.

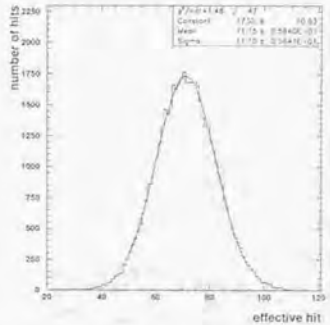

Figure 5–20: The distribution of the N_{eff} for the electron events of total energy of 10MeV. A Gaussian fit is applied to get the peak value of the distribution.

volume and all direction. A MC simulation which includes the LINAC system configuration (namely the beam pipe, the trigger counter, and the Ti window) is carried out for various tuning parameters (collection efficiency and coefficients of scattering and absorption of light in water: see chapter 3). The input electrons are injected in the beam pipe from before the trigger counter to a downward direction with the beam spread corresponding to the size of the trigger counter. MC simulation data are also analyzed as same way as the LINAC data, and measured N_{eff} values of both are compared. The tuned parameters for which the MC simulation best agrees with the LINAC data are selected.

With the best-tuned MC simulation, about 6×10^4 events are generated in the fiducial volume for electrons of total energy of 4, 5, 6, 7, 10, 15, 30 and 50MeV. The distribution of the N_{eff} for total energy of 10MeV is shown in figure 5–20. A Gaussian fit is applied to the distribution to reduce the distribution to a value. An MeV value for the total energy of the electrons is obtained by fitting a 4-th order polynomial function as shown in figure 5–21. A fitting accuracy is about ±0.1%. Thus the energy observed in SK, E_{SK} is defined by in our current MC simulation[3]:

$$E_{SK} = 0.80586 + 0.12982N_{eff} - 0.17176\cdot10^{-4}N_{eff}^2 + 0.19489\cdot10^{-6}N_{eff}^3 - 0.32113\cdot10^{-9}N_{eff}^4 \quad (5\text{-}7)$$

If higher order terms are ignored, the conversion from the N_{eff} to the energy is approximately represented as 1MeV≃7.71 effective hits.

[3]This function may be altered if the detector MC simulation parameters are further re-tuned.

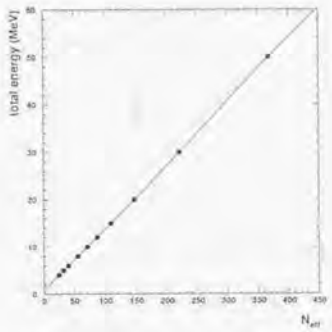

Figure 5–21: A 4-th order polynomial fit to the correlation between the peak values of the N_{eff} and the total energies of the electrons.

The measured energy distribution of the LINAC data and the MC simulation for seven beam energies at the position x=(−1237cm,−70.7cm,+1228cm) is shown in figure 5–22. Agreement is very good including width of the energy distribution[4]. Further, figure 5–23 shows an energy spectrum of 10.78MeV/c LINAC data summing the data of 8 positions (cross marks) with the corresponding MC (boxes, each box height corresponds to square sum of MC statistical error and energy resolution systematic error(2%), which is described later). As shown in the figure, the MC simulation reproduces the detector response to electrons even up to a 3σ tail of the spectrum.

The LINAC calibration data are used for tuning of the parameters in the SK detector MC simulation. However, there still remain systematic discrepancies between data and MC. Another useful aspect of the LINAC calibration data is to evaluate remaining systematic difference between the LINAC data and the MC simulation. Energy deviation between them for each beam energy and at each position is shown in figure 5–24. Error bars of all marks are statistical at each point and for each beam energy. From now on, the LINAC data is denoted as 'LINAC' and the MC simulation as 'MC'. The energy systematic difference is evaluated for two classifications, i.e. energy dependence and position dependence, and these are shown in figure 5–25. Figure 5–25 (a) and (b) shows position averaged and energy averaged deviation between data and MC, respectively. Outside error bars in figure 5–25(a) are systematic uncertainty of the LINAC calibration system itself described later. Inner error bars are statistically combined error and the rightest mark in figure 5–25(a) is combined difference for all momenta and at all positions.

[4]Note that the width of energy distribution (i.e. energy resolution) is not a tunable parameter.

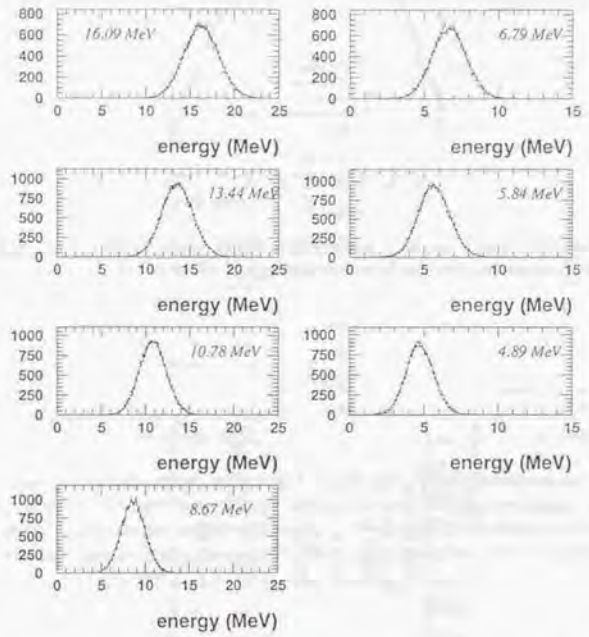

Figure 5–22: LINAC data and MC simulation measured energy distribution for seven beam energies at a position x=(−1237cm,−70.7cm,+1228cm). The cross marks are the LINAC data and histograms are the MC simulation.

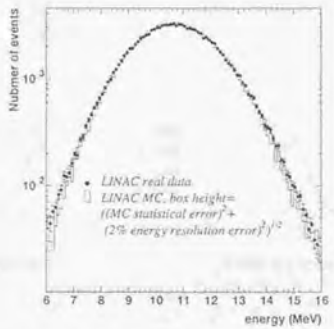

Figure 5–23: Summed energy spectrum for real data (cross marks) and MC simulation (boxes) over the LINAC 8 positions with the beam momentum of 10.78MeV/c.

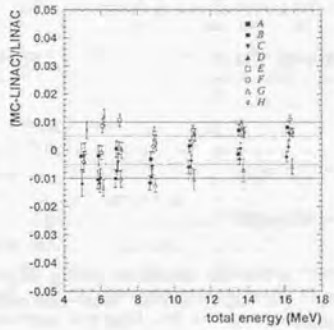

Figure 5–24: The energy deviation between the LINAC data and the MC simulation for seven beam energies and at 8positions. A∼H mean the positions defined in table 5–2.

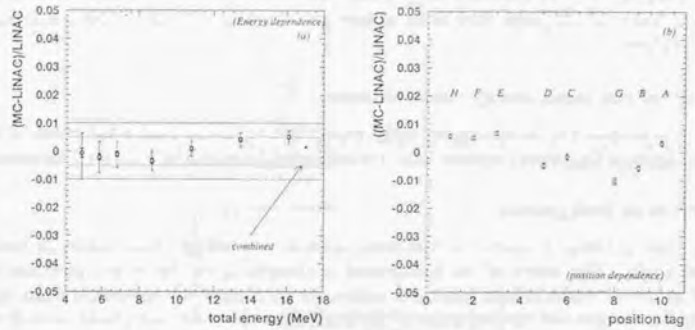

Figure 5–25: The systematic energy difference between the LINAC data and the MC simulation, (a) energy dependence (position averaged deviation) and (b) position dependence (energy averaged deviation). Outside error bars of figure(a) are the LINAC system systematic uncertainty described later. Inside error bars are the statistical error. Error bars of figure(b) are only statistical error.

These values are used for an evaluation of the systematic error of the solar neutrino flux and the measurement of the energy spectrum. The detailed discussion of it is given later. In figure 5-25(a), though the deviation have energy dependence, all points stay within ±0.5%. These figures are used for evaluating energy correlated systematic errors as described in section 7.2.

Energy resolution is also investigated. Figure 5-26 shows the energy resolution as a function of the electron total energy at each position for the LINAC data (a) and the MC simulation (b). Position averaged deviation of the energy resolution as a function of the electron total energy is also shown in figure (c). Although the energy resolution is not a tunable parameter, the deviation between the LINAC data and the MC simulation is consistent within 2%.

5.4.4 Systematic uncertainty of the LINAC system

In order to confirm that the absolute energy is determined within 1%, systematic uncertainty of the LINAC calibration system have to be considered. The source of the systematic error is classified as follows.

Uncertainty of the beam energy determination

This value is determined by measuring the beam energy five times and taking full width of the distribution for each D1 magnet current, and it is estimated to be ±20keV for all 7 momenta.

Beam correlated background

When the electron beam is injected to the tank, there is a possibility that beam correlated background exists. The source of the background is thought to be the γ-rays produced by the run off electrons, which hit the collimator before the D2 magnet or the vertical beam pipe between the D3 magnet and the end point of the beam pipe. In order to evaluate level of the background, data taking with "empty" (microwave) trigger and "random" (clock) trigger was done. The trigger logic of these trigger modes is shown in figure 5-16. As described above, since the injection rate of single electron is 0.1 per microwave, 90% microwave triggered data are empty with possible background. By comparing the background level of the empty trigger data and the random trigger data, the background level is estimated. Differences between the background level fluctuate around zero, and conservative estimation is done, i.e. averaging over the absolute values of these differences, and the systematic uncertainty of the beam correlated background is evaluated to be ±0.16%.

Reflectivity of the end point of the beam pipe

The most serious uncertainty of the LINAC system is reflectivity of the end point cap of the beam pipe. In the MC simulation, it is found that about 5% Cherenkov photons hit the end point at the electron momentum of 5MeV/c. Although the reflectivity of the end point was measured, it is found that there is a possibility that an air bubble is trapped in a hollow space enclosing the Ti window and the unknown size of the bubble changes the reflectivity of the end point. In order to estimate the effect, two set of MC simulations for the extreme case of no air

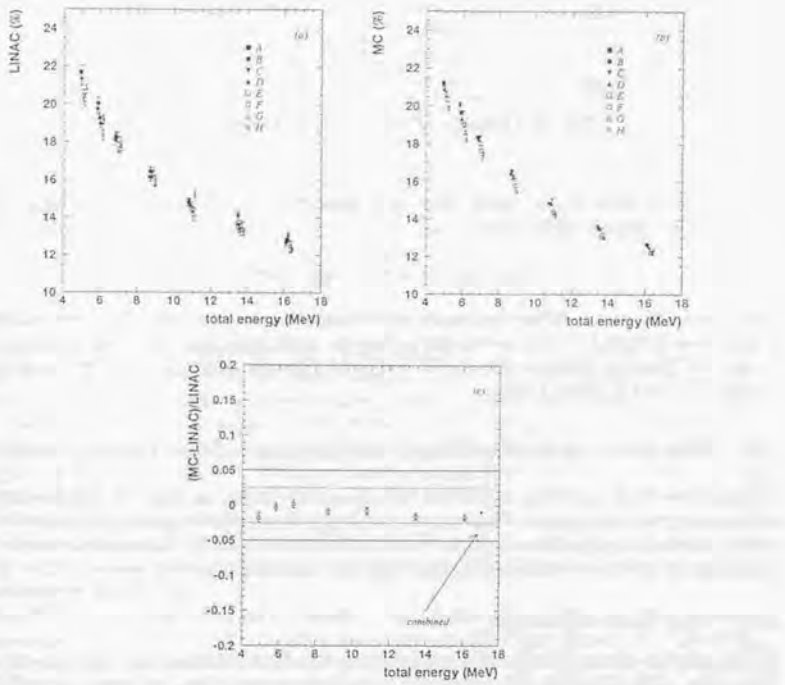

Figure 5-26: The energy resolution as a function of the electron total energy at each position for LINAC data(a) and MC simulation(b). Figure (c) shows the position averaged deviation of the energy resolution.

beam momentum (MeV/c)	fraction hitting beam pipe	error due to reflectivity	total systematic error
16.31	0.51%	±0.06%	±0.21%
13.65	0.67%	±0.08%	±0.24%
10.99	0.88%	±0.11%	±0.27%
8.86	1.3%	±0.18%	±0.33%
7.00	2.2%	±0.28%	±0.44%
6.03	3.3%	±0.40%	±0.55%
5.08	4.7%	±0.68%	±0.81%

Table 5-3: The list of the LINAC systematic error.

and maximum bubble size are carried out. And conservative uncertainty of this is estimated. The results are given in table 5–3.

Summary

Energy dependence of combined systematic uncertainty (the sum of square of all uncertainties) is also shown in table 5–3. The uncertainty is large for small beam momentum due to the larger fraction of Cherenkov photons that hit the end point. The systematic uncertainty is shown as outside error bars in figure 5–25(a).

5.5 The time and directional uniformity of the energy scale

There are two other important aspects for the energy calibration, i.e. the time and directional uniformity of the energy scale. The former is checked by the spallation events, the Ni-Cf γ-ray source, and the μ decay electron events. The latter is checked by only the spallation events. In this section, a description of these two aspects of the energy calibration is given.

5.5.1 The time uniformity

As mentioned in section 5.3, the water transparency have been changing since the beginning of data taking of SK. The time variation of the water transparency affects the energy scale of the detector strongly. In order to correct for the variation, the water transparency obtained by the μ decay electron events is substituted for the equation (4-8) event by event. In order to check the validity of the method, radioactive sources, such as the spallation events, the Ni-Cf γ-ray events and the μ decay electron events, are used.

The details of the spallation event is described in appendix B. These products emit β-rays whose energy are similar to that of the recoil electrons scattered by the solar neutrinos. Further, the elements are produced almost uniformly in space and time in the ID and emit β-rays with uniform direction. Hence, the spallation products are good calibrator to investigate

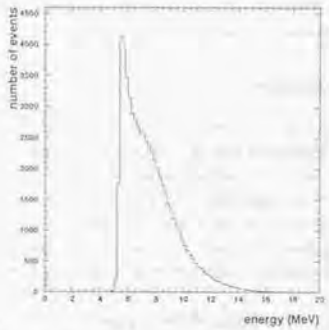

Figure 5-27: Energy spectrum of the spallation events.

the directional and time uniformity of the energy scale of ID. However, branching ratio of the spallation products generated by the interaction (B-1) is not known in detail, therefore it is difficult to use these radioactive elements as a calibrator for the absolute energy determination. Event selection of the spallation product candidates is described in appendix B. Figure 5–27 shows energy spectrum of the spallation events. In order to study the time variation of the energy scale using the spallation events, the following manipulation is done. At first, the total spallation sample is separated into time periods. For each period, the energy scale is changed artificially by multiplying a factor and the energy spectrum of the each period is compared with that of the whole sample. Comparison is done by a χ^2 test in a energy range of 6.5~15MeV[5]. Figure 5–28(a) shows the time variation of the factor. The figure shows that the energy scale is consistent within ±0.5%.

Though the Ni-Cf source has large systematic uncertainty by itself, this source is useful for this purpose, since only the relative energy scale is important. Unfortunately, the data taking with this source is not carried out frequently, therefore this source is used for an additional check. Figure 5–28(b) shows the time variation of averaged energy of recoil electrons scattered by the Ni-Cf γ-rays. This figure shows also that the energy scale is consistent within ±0.5%.

Third radioactive source is the μ decay electron events. The details of the μ decay electron events are described in appendix C. The μ decay electron events used here are the same as those used for the calculation of the water transparency. Advantages to using the events for this purpose are that statistics of the events are large and background contamination is

[5]The lower bound of 6.5MeV is determined by taking into account the trigger efficiency and Rn event contamination. The upper bound is set to 15MeV, because, above 15MeV, statistics of the spallation events become poor.

almost negligible. Figure 5-28(c) shows the time variation of energy of the events. One point corresponds to two weeks. The figure also shows that the energy scale is stable within ±0.5%.

In summary, three radioactive sources indicate that the time variation of the energy scale for long time period (~2 years) is stable within ±0.5%.

5.5.2 The directional uniformity

To know the directional uniformity of the energy scale and to extrapolate the precise energy calibration achieved by the LINAC calibration to all directions are quit important when studying the energy spectrum distortion and the day/night effect caused by the MSW effect. Unfortunately, the only reliable source to check the uniformity is the spallation events. The Ni-Cf calibration source has directional asymmetry caused by asymmetrical configuration of the Ni wire and material such a pulling stainless steel wire, a signal cable, etc. The μ decay electron events have direction dependent energy spectrum due to polarization of the parent stopping muon.

Figure 5-29 shows zenith angle dependence of the energy scale for the spallation events. The way of estimating the factor is the same as that used for the time variation investigation. The figure indicates that the directional dependence of the energy scale is consistent within ±0.5%.

5.6 Angular resolution

Angular resolution at SK detector is measured by the LINAC calibration. Though the LINAC system can measure the angular resolution for only one direction (downward), it provides a crucial test of the detector simulation. Figure 5-30 shows distributions of an opening angle between the direction of the beam injection and the reconstructed direction for LINAC data (cross) and MC simulation (histogram) at a position $\boldsymbol{x}$=(−1237cm, −70.7cm, +1228cm) for 7 electron momenta. Agreement is excellent. The angular resolution is defined as an angle which includes 68% of the reconstructed directions around the beam direction. Energy dependence of the angular resolution at 8 positions for LINAC data and MC simulation are shown in figure 5-31(a) and (b) respectively. Figure 5-31 (c) shows deviation between LINAC and MC for 7 momenta and at 8 positions. Though the angular resolution of MC simulation is larger than that of LINAC data and the deviation has some position dependence, almost all points are consistent within 5%. Error bars of figure 5-31(a),(b),(c) are only the statistical error. Figure 5-31(d) shows the position combined deviation. Error bars of 5-31(d) are variances at each beam momentum in figure 5-31(c). This slight disagreement between LINAC and MC causes a comparatively large systematic error for the measured solar neutrino flux value.

5.7 Vertex resolution and shift

The LINAC system can also calibrate vertex resolution. Figure 5-32 shows distributions of distance from the end point of the beam pipe to the reconstructed vertex position at a beam

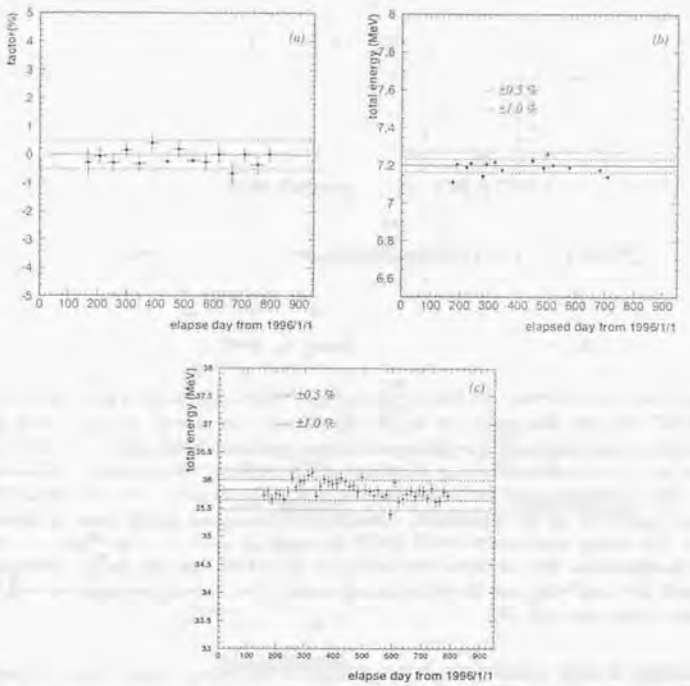

Figure 5-28: The time variation of the energy scale for three calibration sources. (a) the spallation events, (b) the Ni-Cf source, (c) the μ decay electron events

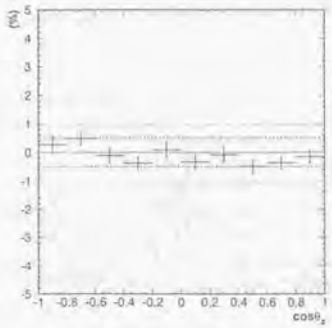

Figure 5-29: The directional dependence of the energy scale.

injection position x=(−1237cm,−70.7cm,+1228cm) for 7 beam momenta. Again cross marks are for LINAC data and histograms are the MC simulation. Vertex resolution is defined as a spherical radius which includes 68% reconstructed vertex position around the end point. Figure 5-33 shows (a) the vertex resolution as a function of the electron total energy at 8 positions for LINAC data, (b) same as (a) but for the MC simulation, (c) deviation between (a) and (b), (d) deviation combined for the 8 positions. Error bars of the figures are the same as those of figure 5-31. The timing resolution of the ID PMTs for single photo-electron response in the MC simulation is adjusted so that the vertex resolutions of the LINAC data and the MC simulation are consistent for 8 positions, and the value is determined to be 2.4nsec, which agrees with the independently measured value [41].

It it important to know a shift of the vertex position in the vertex reconstruction, since the vertex shift causes a change of the fiducial volume size, i.e. the target number of the solar neutrinos. In order to estimate the vertex shift, the Ni-Cf calibration source is used. The details of the Ni-Cf calibration source is described in appendix A. An advantage to use the Ni-Cf γ-ray source is that the source can emit γ-rays to almost uniform directions. The vertex shift is defined as a vector from an averaged position of the reconstructed vertex of the data to that of a corresponding MC simulation. Table 5-4 shows the vertex shift at some source positions. These values are used to obtain systematic error for the measured solar neutrino flux.

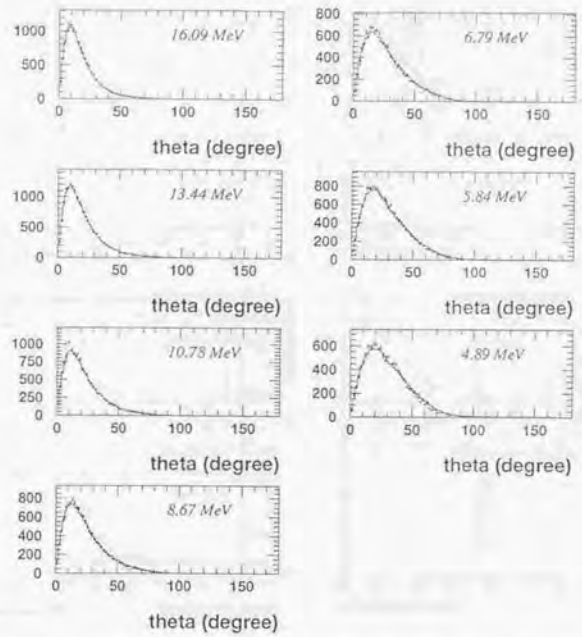

Figure 5-30: An opening angular distribution at x=(−1237cm,−70.7cm,+1228cm) for 7 electron momenta. The cross marks are the LINAC data and histograms are the MC simulation.

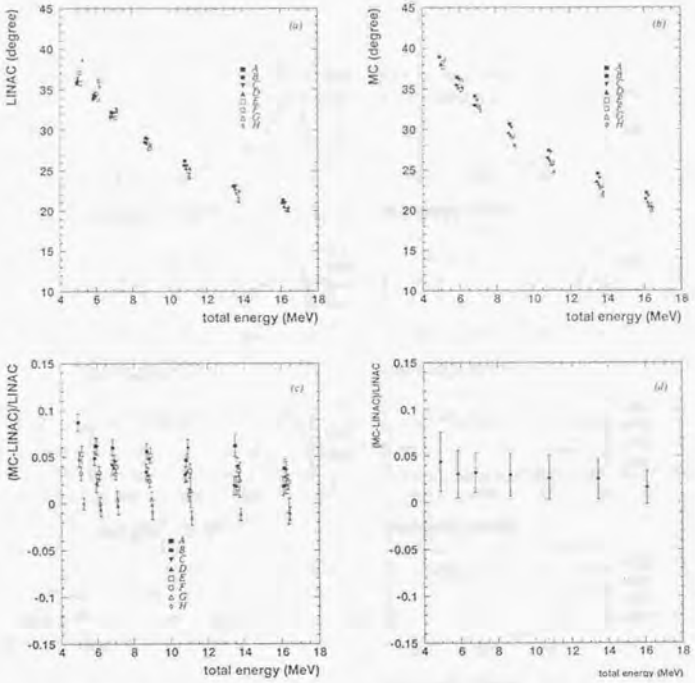

Figure 5–31: Angular resolution as a function of the electron total energy. (a) is for LINAC data, (b) is for MC simulation, (c) is the deviation between LINAC and MC at 8 positions and 7 momenta and (d) is the position combined deviation. Explanations of error bars of the figures are given in text.

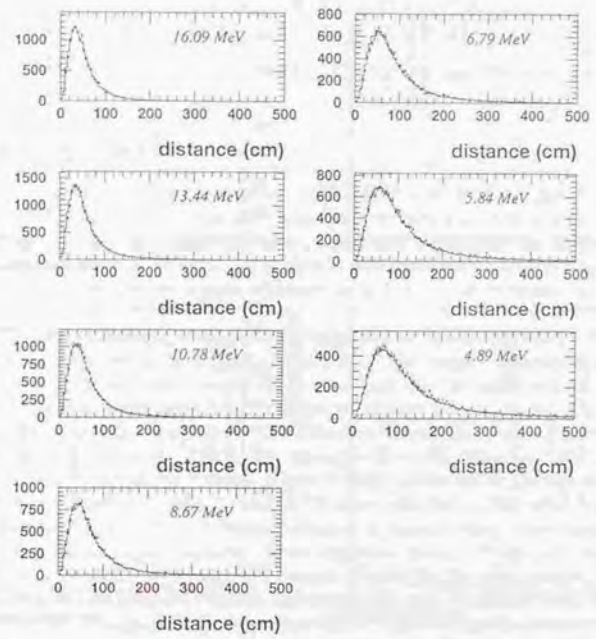

Figure 5–32: Distributions of distance from the end point of the beam pipe to the reconstructed vertex position at a beam injection position x=(−1237cm,−70.7cm,+1228cm) for 7 beam momenta for LINAC data (cross) and MC simulation (histogram)

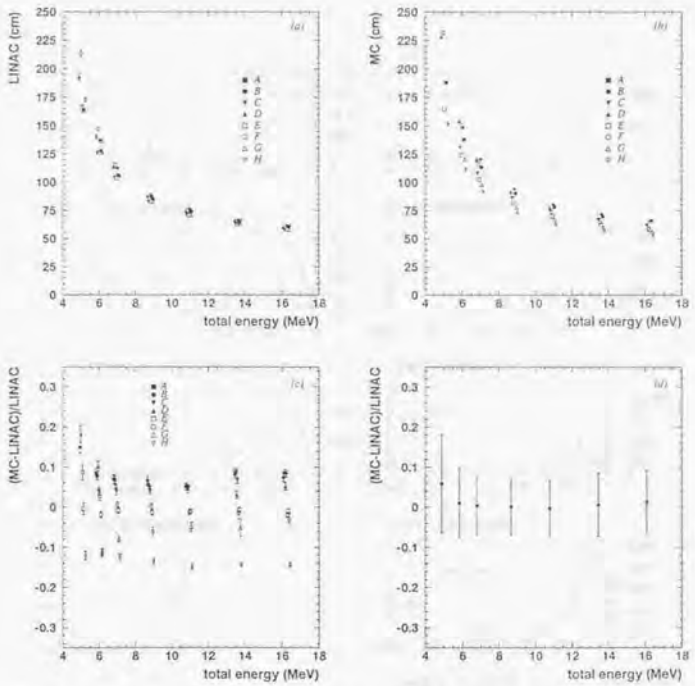

Figure 5–33: Vertex resolution as a function of the electron total energy. (a) is for LINAC data, (b) is for MC simulation, (c) is deviation between LINAC and MC at 8 positions and 7 momenta and (d) is the position combined deviation. Explanations of error bars of the figures are given in the text.

Source position	Δx	Δy	Δz
(35.3,−70.7,−1200.)	−0.3	−2.7	−3.0
(35.3,−70.7,0.)	0.7	−0.5	−1.9
(35.3,−70.7,+1200.)	−1.0	−0.7	−1.0
(35.3,−70.7,+1600.)	−0.6	−2.8	−10.0
(35.3,−1201.,−1200.)	−3.4	7.0	−7.0
(35.3,−1201.,0.)	−1.1	16.0	−1.1
(35.3,−1201.,+1200.)	0.6	10.0	2.0

Table 5–4: The vertex shift measured by the Ni-Cf source. The unit is cm

5.8 Trigger efficiency

As described in chapter 3, when the number of hit PMTs exceeds 29, a global trigger (L.E trigger) is issued. It is important for the solar neutrino observation to know how much measured energy is necessary in order to issue the trigger. In order to investigate the trigger efficiency, again the Ni-Cf source is used. As described in appendix A, the Ni-Cf source can emit sufficiently low energy γ-rays, by which the trigger efficiency as a function of measured energy can be obtained.

In the Ni-Cf source calibration, an additional trigger, whose threshold is 150mV (corresponds to about 14 hits) and called a 'Ni trigger', is provided. The trigger efficiency is obtained by calculating a ratio of the number of events which issue both the Ni trigger and the L.E. trigger to the number of events which issue the Ni trigger for several energy regions. Figure 5–34(a) shows energy spectrum obtained by the Ni-Cf calibration. Blank histogram is for events issuing Ni trigger and hatched histogram is for events issuing both the Ni trigger and the L.E. trigger. A range of the energy bin is set to 0.5MeV. Figure 5–34(b) shows the trigger efficiency derived from figure 5–34(a). Filled marks are for the Ni-Cf source real data. This curve is obtained by dividing the hatched histogram by the blank histogram in figure 5–34(a). Open marks in figure 5–34(b) are results of a trigger simulator, which simulates issuing of the L.E. trigger in the corresponding MC simulation. The trigger simulator is used for the solar neutrino analysis as described later. As shown in figure 5–34(b), the trigger efficiency is almost 100% above 7MeV and it decreases as the energy is decreasing below 7MeV. The discrepancy between the Ni data and the trigger simulator is dealt with as systematic difference. The trigger efficiency has also position and time dependence. The dependence is caused mainly by water attenuation length of Cherenkov light and investigated by locating the Ni-Cf source at various positions and by carrying out the Ni-Cf calibration periodically. Table 5–5 gives the trigger efficiency value at two positions, $\boldsymbol{x} = (+35.3,-70.7,0)$ and $(+35.3,-70.7,+1200)$ in the detector coordinates, which is obtained on 3rd of June in 1997.

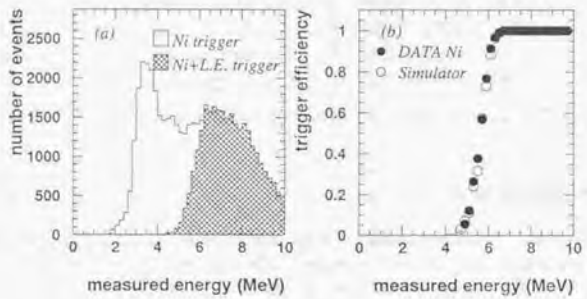

Figure 5-34: Figure (a) shows the energy spectrum obtained by the Ni-Cf calibration for the Ni triggered events (blank), and the Ni and L.E. triggered events (hatched). Figure (b) shows the trigger efficiency curve. Filled marks are obtained by dividing the hatched histogram by the blank histogram in figure(a). Open marks are obtained by the trigger simulator in the corresponding MC simulation.

Energy range(MeV)	(+35.3,−70.7,0)	(+35.3,−70.7,+1200)
5.0-5.5	20.2%	36.5%
5.5-6.0	63.8%	76.2%
6.0-6.5	94.0%	96.0%
6.5-7.0	99.8%	99.8%
7.0-	100.0%	100.0%

Table 5-5: The trigger efficiency values as a function of measured energy at two positions which are obtained on 3rd of June in 1997.

Chapter 6

Data reduction

This chapter describes the data reduction steps used to obtain solar neutrino signals. SK experiment started on 1st of April, 1996. Since purity of the tank water was not so good and Rn concentration in the water was high in the first 2 months, the solar neutrino analysis uses data taken after this period. In this thesis, data taken from May 31, 1996 to March 25, 1998 are used. In this period, 87% of time was consumed for normal data taking and most of the remaining time was used for the calibration of the SK detector. Figure 6-1 shows the live time of the normal data taking as a function of elapsed day from 1st of January, 1996. 11.4% of normal runs are rejected because of bad qualities, such as high rate due to flash tube events or noise events. Criteria to cut the bad runs will be described later. Finally, the total live time used for the analysis is 503.8days.

The L.E.trigger event rate is about 10Hz. About 2Hz is caused by cosmic ray muons and most of the remaining events are due to radioactive decays of Rn or γ-rays coming from outside of the detector or material on the ID wall. Total number of events in the live-time of 503.8 days is about $\sim 6 \times 10^8$. In order to extract solar neutrino events from this enormous number of events, various cuts are applied. This section describes the data reduction in due order.

6.1 Selection of low energy events

First step of the reduction is to select low energy events. The rejected events are cosmic ray muon events, flash tube events, noise events, and so on. Inefficiency of the solar neutrino events of following reductions is evaluated using the MC simulation (see table 6-1 in page 124).

6.1.1 Total photo-electron cut

First of all, high energy events, such as cosmic ray muon events (deposit energy $\sim$ 8GeV), atmospheric neutrino events (deposit energy $\sim$ 1GeV), are eliminated. Figure 6-2 shows total photo-electron number distribution in logarithmic scale. A clear peak of higher side in figure 6-2 is the high energy events. The cut criterion is

- total number of photo-electrons in the ID $\leq$ 1000p.e.

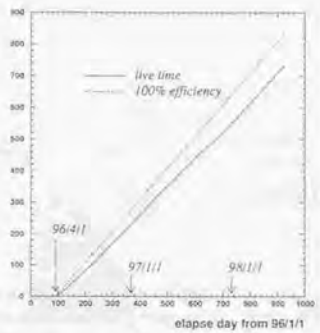

Figure 6–1: Live time of the normal data taking as a function of elapsed day from 1st of January, 1996.

This photo-electron number (i.e. 1000p.e.) corresponds to about 130MeV for an electron event, which is sufficiently high for the solar neutrino events, and therefore the inefficiency of the cut for the solar neutrino events is negligible.

6.1.2 L.E. trigger event

As described in chapter 3, there are three kinds of triggers, namely SLE trigger (24hits threshold, from May 1997), LE trigger (29hits threshold), and HE trigger(31hits threshold). In this thesis, only the events which fire the L.E. trigger are used for the solar neutrino analysis. The analysis with SLE triggered data is now under study. The trigger simulator which was described in chapter 5 is applied to the MC simulation.

6.1.3 Time difference cut

In order to eliminate μ decay electron events, after-pulse events, etc, a time difference cut is applied. Figure 6–3 shows distribution of the time difference from previous event. A peak around 1μsec are due to ringing events[1] and the second peaks around 15μsec is due to after-

[1]When a high energy penetrating muon event happens, almost all PMTs of ID catch large photo-electrons. The large output signals from the PMTs are reflected on ATM side due to impedance imsmatch between signal cable and the ATM input side. If the signal is sufficiently large, the reflected signals are further reflected back on PMT side due to same reason and the reflected signal comes back to ATM again. Length of the cable between the PMT and the ATM is about 70m, hence the time that the signal needs to take to travel ATM-PMT-ATM is about 700nsec. However, each channel of ATM opens 900nsec veto window after it was hit. Therefore, the first

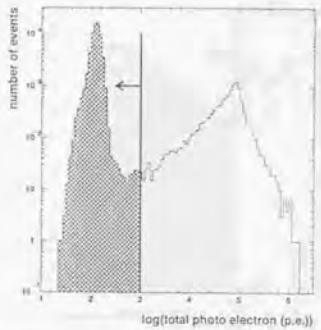

Figure 6–2: Distribution of total photo-electron number in logarithmic scale. The criterion of the total photo-electron cut is also shown.

pulse events described in chapter 3. Interval events between two peaks are stopping μ decay electron events. The cut criterion to reject these events is

- time difference from previous event $> 50\mu$sec

Dead time caused by the cut is 1.8×10^{-4}, which is negligible for the solar neutrino observation.

6.1.4 Outer detector event cut

In order to reject remaining cosmic ray muon events which hit OD PMTs, following cut is imposed.

- OD trigger does not issue and number of hits in the OD ≤ 20

6.1.5 Noise event cut

In the electronics system used by the SK experiment, electronic noise sometimes happens. Sources of the noise are suspected to be PMT flashing, turning on-off of fluorescent lights, and so on. Figure 6–4 shows an example event display of the noise event. A characteristic point

reflected signal is discarded. However the second reflected signal which comes after $\sim$1.4μsec is recorded by the ATM. These events are called ringing events.

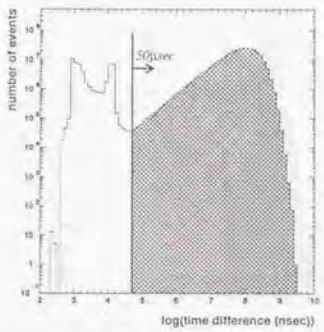

Figure 6–3: Distribution of time difference from previous event.

of this kind of event is that noise hit channels have small charge. Then, a following variable is defined,

$$N/S = \frac{\text{number of hit channels}(|Q_{PMT}| < 0.5\text{p.e.})}{\text{total number of hit channels}} \quad (6\text{-}1)$$

where $|Q_{PMT}|$ is the absolute charge value of hit ATM channel. Figure 6–5(a) shows distribution of the N/S. A higher side peak is due to the noise events. The cut criterion of the N/S cut is

- $N/S < 0.4$

Further, these noise hit channels are often clustered in one ATM board. Then, following cut is also applied for the noise event cut,

- $ATMratio \equiv \max\left(\frac{\text{number of hit in one ATM board}}{\text{number of channel in one ATM board}}\right) < 0.95$

Distribution of the $ATMratio$ is shown in figure 6–5(b). The inefficiency of this cut for the solar neutrino events is estimated by the MC simulation as described later.

6.1.6 Flasher event cut

The 'flasher events' are caused by light emission from a PMT resulting from electrical discharge between dynodes. Figure 6–6 shows an event display of the typical flasher event. Most of the flashers can be found by an instantaneous increase of trigger rate (strong flasher). In this case shift crew identify the flashing PMT and high voltage of the PMT is switched off. However, in case of flashers of lower rate and lower light emission, the flasher events remain in the reduced

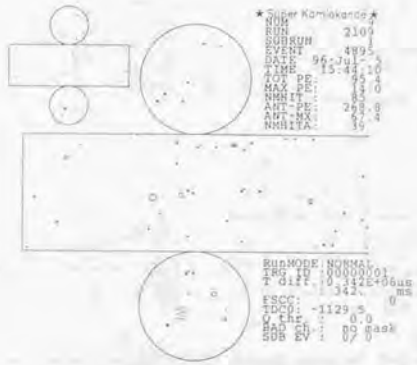

Figure 6–4: An event display of the typical noise event.

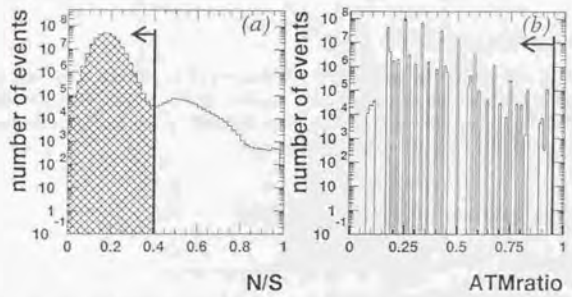

Figure 6–5: (a) shows N/S distribution and (b) shows $ATMratio$ distribution.

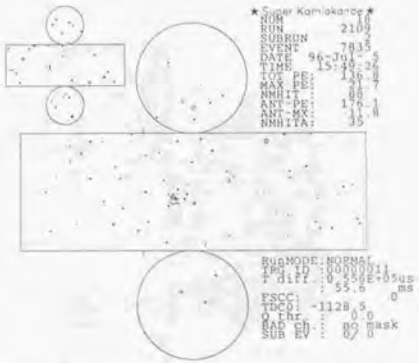

Figure 6–6: An event display of the typical flasher event.

data. They are rejected by a following criterion. When a PMT is flashing, the flashing PMT often detects a large pulse height and the PMTs surrounding the flashing PMT have signals. Figure 6–7(a) shows a scatter plot of maximum charge of one PMT (Q_{max}) versus number of hit PMTs surrounding the PMT which gives Q_{max} ($0 \leq mx \leq 24$), for a typical run including flasher events, and figure 6–7(b) shows same as (a) but for a typical normal run. The cut criterion is:

- events which are in the indicated region shown in figure 6–7 are rejected.

6.1.7 Very low energy event cut

After the above cuts, the remaining events are reconstructed to obtain a vertex, direction and energy as described in chapter 4. When the number of hit PMTs used for the vertex reconstruction (N_v, see equation 4-4) is too small, it is difficult to get enough accuracy of the vertex position. Hence, events with $N_v \leq 10$ are rejected.

- $N_v > 10$

This cut corresponds to an energy cut of 2MeV threshold.

6.1.8 Goodness cut

In addition to the above "very low energy cut", a goodness cut is also applied. If a goodness g_v (see equation 4-4) value of an event is low, the reconstructed vertex position of the event is suspected to be wrong. Therefore, a following cut criterion is imposed:

- goodness ≥ 0.4

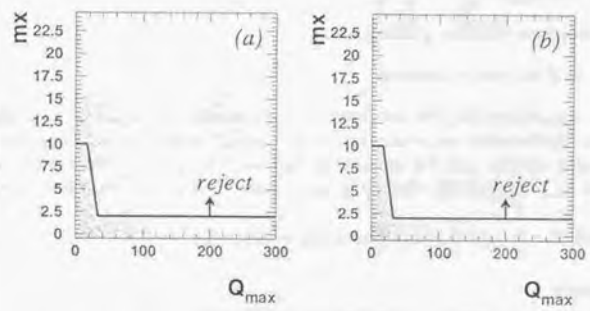

Figure 6–7: Scatter plots of Q_{max} vs mx. The events which are in the indicated region are rejected as the flasher events.

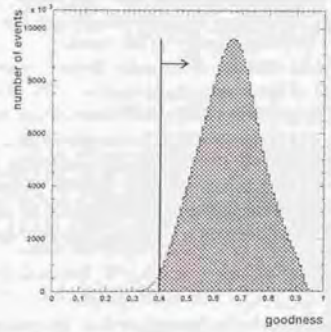

Figure 6–8: The goodness distribution. The cut criterion is also drawn.

6.1.9 Bad runs

The previous sections describe the rejection of bad events, such as flasher events and noise events. If the rate of bad events is high, we reject all events in the particular "sub-run[2]". The following sub-runs are rejected.

- total run time of one sub-run $\leq$ 30seconds,
- total live time of one run $\leq$ 5minutes.

These criteria are imposed at first, because more than 30seconds are needed to count the event rate of bad events. Further, the sub-runs that the bad quality event (flasher, noise, and so on) rate is extremely high are rejected. For example, if the rate of flasher candidate events becomes larger than 0.15Hz in a sub-run, the sub-run is eliminated. In this bad run selection, 65.2days data are rejected.

The bad run selection is carried out at first in the event reduction.

6.1.10 Summary

This section described the selection of low energy events. Table 6–1 (page 124) shows the numbers of remaining events at each reduction step for real data and the solar neutrino MC simulation (^{8}B+hep neutrino events).

6.2 Further reduction of the low energy events

This section describes data reduction using the reconstructed vertex and direction. First of all, events with $d_{wall} > 1.5$m and $E > 4$MeV are selected after the above reduction (pre-cut) and the following selections are applied, where d_{wall} is a distance from reconstructed vertex position to the nearest wall of ID and E is measured energy of the event.

The second cut is called the noise cleaner. The noise cleaner, which is composed of two algorithms, reevaluates the validity of the vertex reconstruction. For example, figure 6–9 shows an event display of one remaining events with the reconstructed vertex and direction. This kind of event, that has hit PMTs clustering in one position, is thought to be a γ-ray event originating from the ID wall material (for example, PMT)[3] and has the possibility that the reconstructed vertex position is completely wrong and comes into the fiducial volume. A large fraction of remaining events below 7MeV are mis-reconstructed γ-ray events as shown in figure 6–9. In order to test the correctness of the reconstruction, following two cuts are applied.

6.2.1 Vertex test

In order to reevaluate the validity of the vertex reconstruction, the following algorithm is used. At first, two variables, Δl_{ij} and Δt_{ij}, are introduced. Δl_{ij} and Δt_{ij} are the distance and time

[2]The data taking in SK is subdivided into "sub-run"s. Each sub-run is about 10 minutes.
[3]Actually, similar events can be generated using the MC simulation.

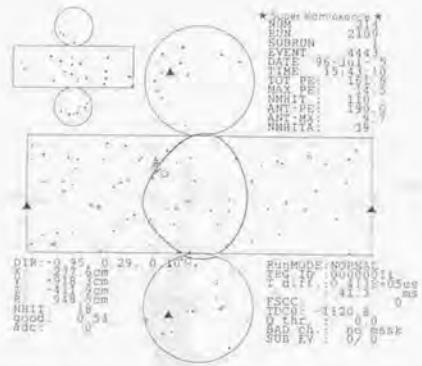

Figure 6–9: An event display of the typical clustering event. Triangles indicate the reconstructed vertex position and closed line is the reconstructed direction.

difference between the i-th and j-th hit PMTs, respectively. If the i-th and j-th hit PMT are originating from the same Cherenkov light source, they should satisfy causality, $c' \leq \Delta l_{ij}/\Delta t_{ij}$, where c' is light velocity in water. To put it the other way around, dark hit PMTs, which are hit randomly, do not satisfy the causality except for accidental dark hits which happen with very close timing near the real event. In order to reduce the dark noise contribution to the vertex reconstruction, the PMTs which satisfy the following relations are further selected from N_v PMTs.

$$\Delta l_{ij} \leq l_{limit} \quad \Delta t_{ij} \leq t_{limit} \tag{6-2}$$

l_{limit} and t_{limit} are optimized to 700cm and 35nsec respectively by analyzing 5MeV LINAC data. The number of survival PMTs is 75%. If the original vertex is mis-reconstructed with a large dark noise contribution, the distance between original and new vertex positions (d_{vertex}), which is reconstructed using the PMTs satisfying the condition (6-2), is large. Therefore, the vertex position of an event which has large d_{vertex} is suspected to be wrong. Figure 6–10 shows d_{vertex} distribution for real data and the solar neutrino MC in energy ranges of 6.5$\sim$7MeV and 7$\sim$20MeV respectively. The cut criterion is set to:

- $d_{vertex} < 500$cm

As shown in figure 6–10, the lower the energy of the events, the larger the fraction of rejected events.

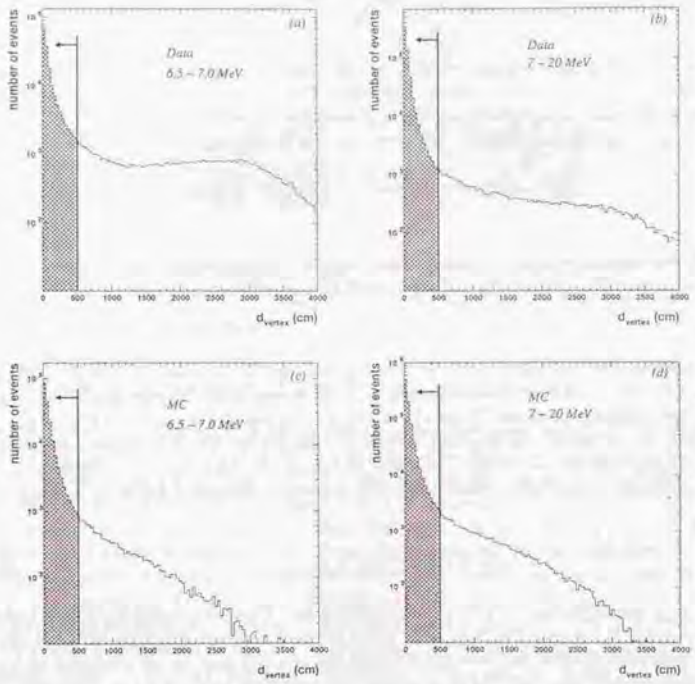

Figure 6–10: Distribution of d_{vertex}. (a)real data(6.5~7.0MeV), (b)real data(7~20MeV), (c)MC data(6.5~7.0MeV), (d)MC data(7~20MeV).

6.2.2 Directional test

In addition to the vertex test, there is another re-evaluation using the reconstructed direction. If the reconstructed vertex position is near the true position, the hit PMTs distribute uniformly about the reconstructed direction. However, if the reconstructed vertex is far away from the true vertex, the PMT hit distribution is non-uniform. In order to test uniformity of the hits, a Kolmogorov-Smirnov (KS) test is applied. Figure 6–11 shows an example of the test. The left figures in figure 6–11 are for a well-reconstructed event. The lower figure shows correlation between i-th PMT among the N_{50}, which is the number of hit PMTs in 50nsec window, and an azimuth angle of the PMT with respect to the reconstructed direction. In ideal case, all PMTs should be on the broken line. Now, let us define a variable *Dirks* which is full width of azimuth angle deviation from the ideal case, divided by 360. In the bad case as with the right figures, the *Dirks* becomes large. Figure 6–12 shows correlation between *Dirks* (horizontal the axis) and Δr (distance from a generated position in MC simulation to the reconstructed position) for solar neutrino MC events. Obviously, the events with larger *Dirks* have large Δr. Figure 6–13 shows *Dirks* distributions for the real data and the solar neutrino MC simulation in energy ranges of 6.5~7.0MeV and 7~20MeV, respectively. The events with *Dirks* > 0.4 are rejected. As shown in the figure, the fraction of the rejected events is larger for lower energy.

6.3 Spallation cut

The large fraction of the remaining events are spallation products. Energetic cosmic ray muons sometimes interact with ^{16}O nuclei and generate radioactive elements called spallation products. The β-decays of the spallation products are serious background for the solar neutrino observation, since the energies of the spallation events are similar to that of recoil electrons scattered by the solar neutrinos.

In order to reject spallation events, time and spatial correlation between the low energy events and preceding muons are used. The originating muons often deposit a large pulse height in the ID. A "spallation likelihood"(L) is defined using these correlations. Details of the likelihood is described in appendix B. Figure 2-6 in appendix B shows the likelihood distribution of real data and random sample events[4]. Events with $L > 0.98$(for reconstructed muon events) and $L > 0.92$(for non-reconstructed muon events) are rejected as the spallation events. The dead time of the spallation cut is investigated using a random sample of events. The dead time is position dependent. Figure 6–14 shows the position dependence of dead time as a function of distance from top (left figure) and barrel (right figure). Blank marks are obtained dead time at each position and lines are results of fitted polynomial functions. The position dependence is taken into account in the solar neutrino MC simulation.

[4]The definition of random sample events is described in appendix B

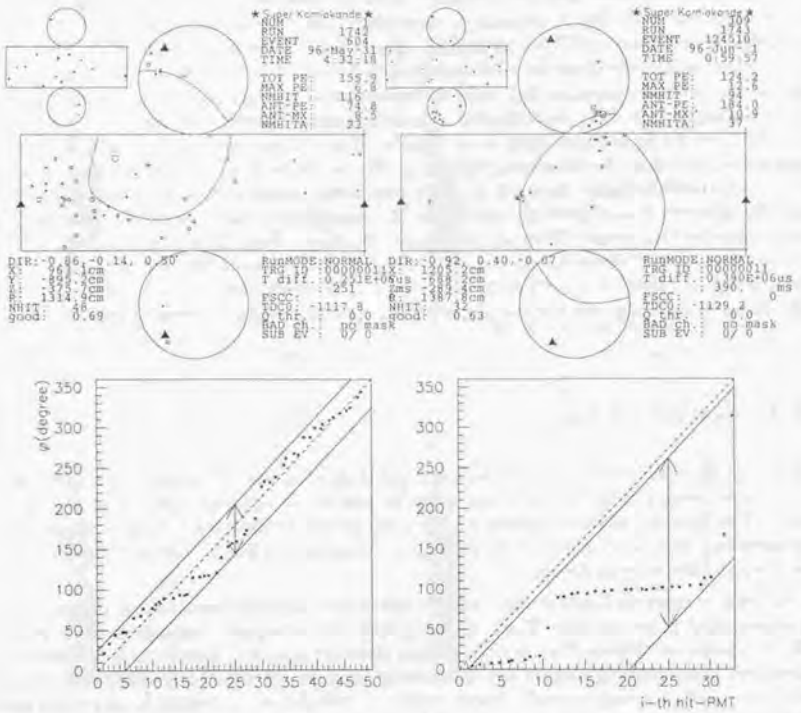

Figure 6–11: An example of the directional test. Left figures are for a well-reconstructed event and right figures are for a bad reconstructed event.

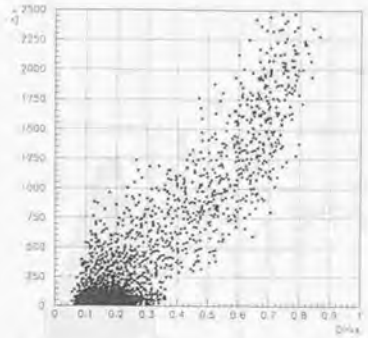

Figure 6–12: The validity check of *Dirks*. The horizontal axis is *Dirks* and the vertical axis is Δr. Points are the solar neutrino MC simulation events above measured energy of 6.5MeV.

6.4 Final cuts

Finally, the following cuts are applied to increase signal to noise ratio after fiducial volume cut is performed ($d_{wall} \geq$200cm).

6.4.1 γ cut

Figure 6–17 shows the vertex and direction distribution (blank histograms) of the events in the fiducial volume. There is an excess of events near the edge of the fiducial volume and the direction distributions (particularly d_z distribution) are not uniform. The excess and non-uniformity are caused by γ-rays from the surrounding rock and ID wall materials. Then, 'γ cut' is applied. A characteristic of the γ-ray events is that they have small 'effective distance' to the wall, d_{eff}, which is defined in figure 6–15. Figure 6–16 shows a distribution of d_{eff} for the real data and the solar neutrino MC simulation for the energy range of 6.5~20.0MeV. The clear excess around $d_{eff} \sim$ 300cm is seen for the real data. The cut criterion of the γ cut is determined so that significance, (number of remaining events of MC)/ $\sqrt{\text{(number of remaining events of DATA)}}$, becomes maximal. The criterion is determined to be:

- $d_{eff} \geq$ 450cm

Figure 6–17 shows the vertex and direction distributions before and after the γ cut for real data for the energy range of 6.5~20.0MeV. As shown in the figure, application of the γ-cut makes the vertex and direction distribution uniform.

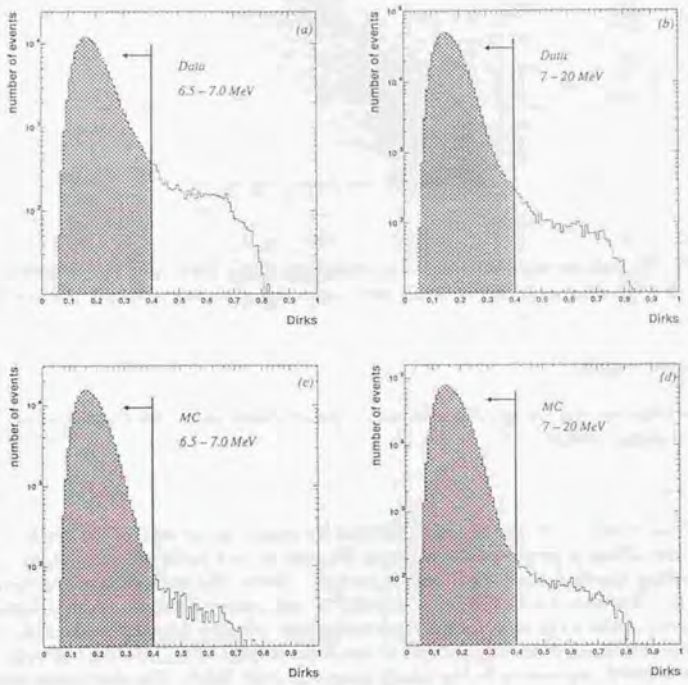

Figure 6–13: Distributions of *Dirks*. (a)real data(6.5~7.0MeV), (b)real data(7~20MeV), (c)MC data(6.5~7.0MeV), (d)MC data(7~20MeV).

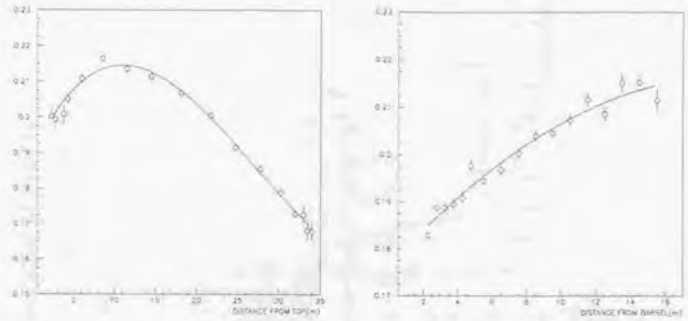

Figure 6–14: Position dependence of the dead time induced by the spallation cut. Left figure shows z dependence and right figure shows r dependence of the dead time (vertical axis of each figure).

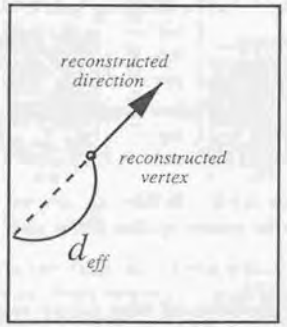

Figure 6–15: The definition of the effective distance d_{eff}.

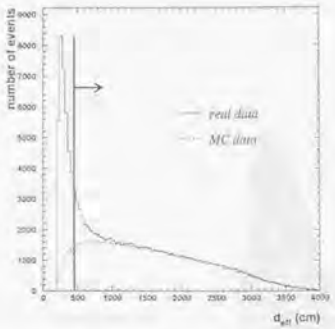

Figure 6–16: A distribution of the effective distance d_{eff}. Line histogram is data and broken line histogram is the solar neutrino MC simulation in the energy range of 6.5~20.0MeV.

6.4.2 Second flasher cut

It is found that specified flasher events, which still remain after the above flasher cut, can be rejected using information from the goodness and the *Dirks*. These flasher events make tiny peak for d_z distribution around $d_z \simeq -0.7$ as shown in figure 6–18(a) (blank histogram). The following cut can reject the peak:

- goodness ≥ 0.6 and $Dirks < 0.25$

The hatched histograms in figure 6–18 are the d_z distribution after applying the cut.

6.4.3 Scan cut

After the events whose energies are in $6.5 \sim 20.0$MeV are selected, the remaining events above 12MeV are eye-scanned. In the scan, remaining clear flasher and noise events are rejected. 22 (0.03%) events are cut.

6.5 Monte Carlo simulation of the solar neutrino events

In order to estimate the reduction efficiency of the solar neutrino signal, the whole analysis chain was applied to the solar neutrino MC events. The solar neutrino MC events are generated 10 events per minute for ^{8}B neutrinos and hep neutrinos, which corresponds to 52 times of the event rate predicted by BP98, in the inner volume (32kton). Total number of the generated

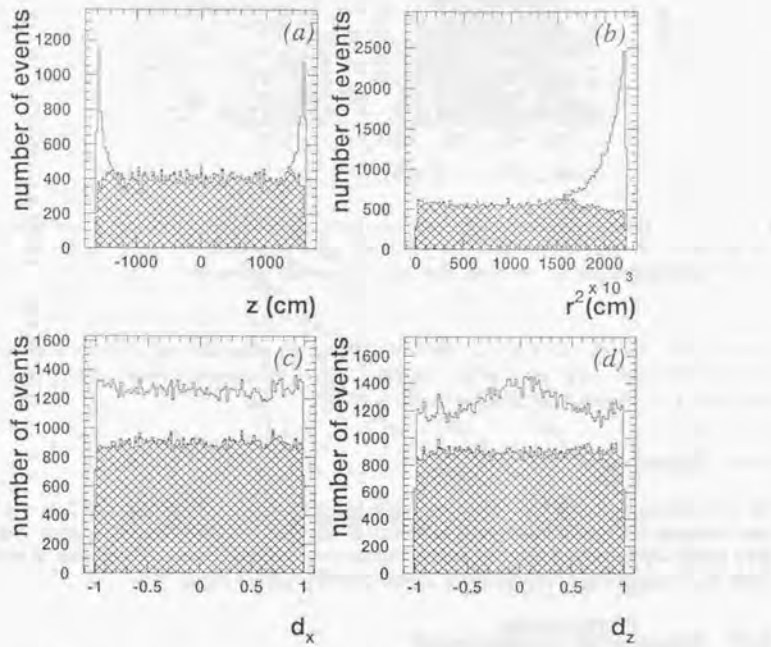

Figure 6–17: The vertex and direction distribution before (blank histograms) and after (hatched histograms) the γ cut. Figure(a) shows vertex z ($r < 1000$cm) distribution, (b) shows r^2 ($|z| < 1000$cm), (c) shows direction of d_x axis, and (d) shows direction of d_z axis.

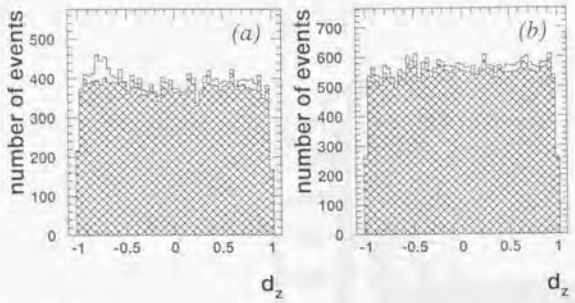

Figure 6-18: The d_z distribution for runs (a) including and (b) not including the specified flasher events (blank histograms). There is a tiny peak around $d_z \simeq -0.7$ in figure (a). The hatched histograms are the resultant ones after the second flasher cut.

events is 7479610. The 4th column of table 6-1 shows the reduction rate of the solar neutrino MC events for the energy range of 6.5~20.0MeV and in the fiducial volume (22.5ktons). The total reduction efficiency of the signal events is 69.6%.

6.6 Summary

Table 6-1 shows the number of remaining events at each reduction step for the real data and the solar neutrino MC events (the energy range is 6.5~20.0MeV in 22.5kt fiducial volume). Figure 6-19 shows energy spectrum of the real data after each reduction step. The number of events which have passed the all cuts is 86637 for 6.5-20.0MeV (final sample).

6.7 Remaining background

The possible sources of the background are remaining spallation events, the radioactive elements originated from Rn, and remaining γ-ray events.

The origin of the spallation event remnant is attributed to an inefficiency of the muon track reconstruction. Especially, multiple muons could be mis-reconstructed.

The Rn concentration in the water is measured to be 5.7mBq/m^3[42]. Though the spectrum endpoint of the ^{214}Bi, which is decay product of the ^{222}Rn, is 3.26MeV, due to the finite energy resolution of the detector, the β-decay events are observed even if the analysis energy threshold

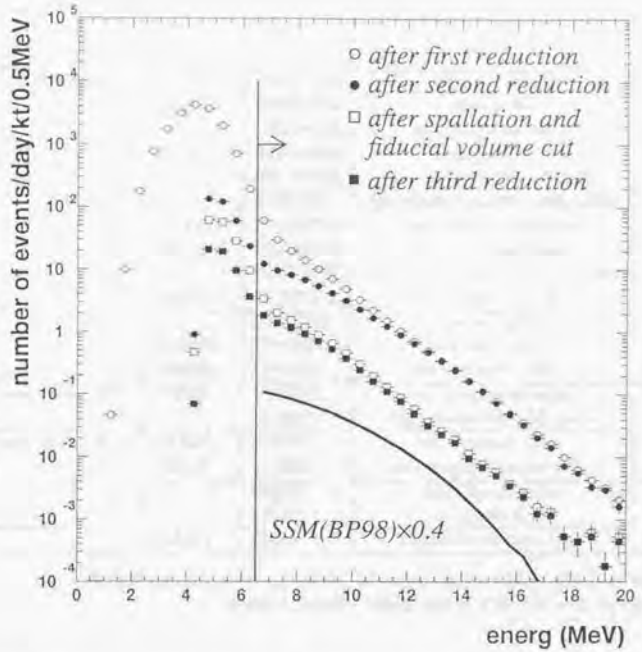

Figure 6-19: Energy spectrum after each reduction steps. See also table 6-1 for the definition of 'first', 'second', and 'third' reduction. Theoretical prediction (BP98×0.4) is also shown (solid line).

	Reduction step	Real Data	MC data	remark
first reduction	all events	574152687	1065579	
	after total p.e. cut	452982631		
	L.E. triggered	378536066	1062542	
	after time difference cut	310028576		
	after outer detector event cut	278136719		
	after noise event cut	277333672	1062425	
	after flash event cut	276067686	1049646	
	after very low energy event cut	275222131		
	after goodness cut	273755790	1049641	
second reduction	after pre-cut	12283890		
	after vertex test	5419261	1006608	
	after direction test	4967048	997136	
	after spallation cut	3523255	799374	20% dead time
	after fiducial volume cut	1904199		
third reduction	after gamma cut	855675	742593	7.2% dead time
	after second flasher cut	696426	741646	
	after energy cut	86659		
	after scan cut	86637		
	final number of events	86637	741646	

Table 6–1: The table of the reduction steps. 'MC data' is the solar neutrino MC simulation in the energy range of 6.5~20.0MeV in the 22.5kt fiducial volume.

is 6.5MeV.

Another possible background is γ-rays coming from the surrounding rock or material on ID wall. The contamination of these events to the final sample events is estimated to be ~12%, if we assume that all excess of the real data events in the d_{eff} distribution in figure 6–16 is the γ-ray events.

Chapter 7

Results

In this chapter, results of the solar neutrino observation, i.e. solar neutrino flux, flux time variations (day/night and seasonal), and energy spectrum of recoil electrons are described. Systematic errors of the measurements are also described.

7.1 Results of solar neutrino observations

7.1.1 Extraction of solar neutrino signals

Extraction of the solar neutrino signals from the final sample is basically carried out using directional correlation of the events with respect to the direction of the sun, since the recoil electrons keep the directionality of the neutrino coming from the sun as described in chapter 3. Let us define an angle between the reconstructed direction and the direction of the sun as θ_{sun} as shown in figure 7–1. Figure 7–2 shows the $\cos\theta_{sun}$ distribution of the data. A peak at $\cos\theta_{sun} = 1$ is direct evidence that neutrinos really come from the sun. The flat component is the remaining background discussed in the previous section. The excess above the flat level is due to the solar neutrinos.

In order to count number of the solar neutrino events, a maximum likelihood method is employed. Let us define a variable x, which is a ratio of the solar neutrino signals to the total number events of the final sample. A probability function used in the maximum likelihood method is given by:

$$P(\cos\theta_{sun,i}, E_i, x) = xP_{sig}(\cos\theta_{sun,i}, E_i) + (1-x)P_{bg}(\cos\theta_{sun,i}, E_i) \qquad (7\text{-}1)$$

where E_i is the event energy, $P_{sig}(\cos\theta_{sun,i}, E_i)$ is a probability density function of the solar neutrino signals, and $P_{bg}(\cos\theta_{sun,i}, E_i)$ is a probability density function of the background. $P_{sig}(\cos\theta_{sun}, E_i)$ is shown in figure 7–3 for various electron energies, which are obtained by the MC simulation. The energy dependence of smearing from $\cos\theta_{sun} = 1$ is due to the finite angular resolution of the detector as shown in figure 5–31. The background probability density function is obtained from the data. In the ideal case, the function does not depend on $\cos\theta_{sun}$

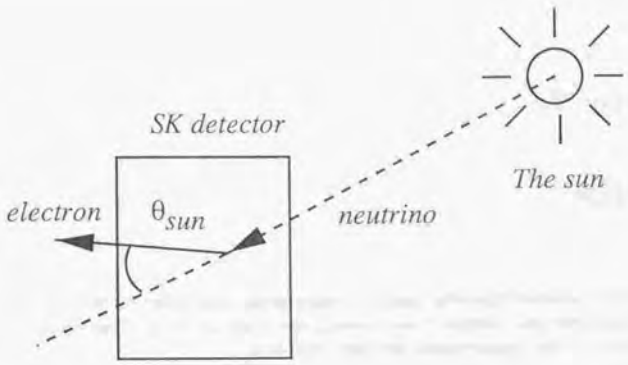

Figure 7–1: Definition of $\cos\theta_{sun}$.

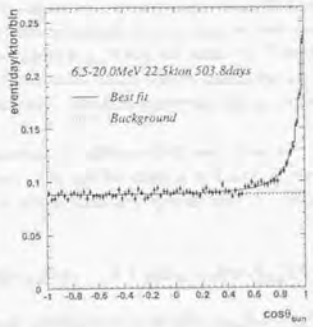

Figure 7–2: The $\cos\theta_{sun}$ distribution for the final sample events. The histogram is the best fit derived from the maximum likelihood method described in the text.

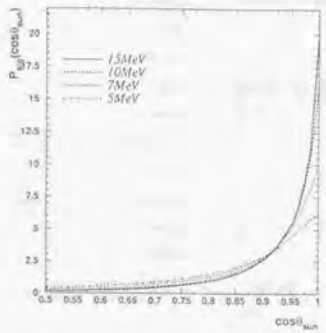

Figure 7–3: Probability density functions $P_{sig}(\cos\theta_{sun}, E)$ for various energies.

and therefore,

$$\int_{-1}^{1} P_{bg}(\cos\theta_{sun}, E)d(\cos\theta_{sun}) = 1 \tag{7-2}$$

$$\text{therefore} \quad P_{bg}(\cos\theta_{sun}, E) = \frac{1}{2} \tag{7-3}$$

However, remaining background may have non-uniform $\cos\theta_{sun}$ distribution, because backgrounds, such as γ-rays, may have strong directionality in the detector coordinate. In order to obtain the probability function of the background, $\cos\theta_z$ distribution of the final sample is fitted by an 8-th order polynomial function for 3 energy intervals (i.e. 6.5∼7.0MeV, 7.0∼10.0MeV, 10.0∼20.0MeV). Figure 7–4 (a) shows the $\cos\theta_z$ distribution in the energy range of 7.0∼10.0MeV with the fitted function. The shape of the $\cos\theta_z$ distribution was mapped to the direction of the sun assuming the uniform azimuthal dependence and $P_{bg}(\cos\theta_{sun}, E)$ is made for each energy interval. Figure 7–4 (b) shows the obtained $P_{bg}(\cos\theta_{sun}, E)$ for three energy ranges.

The variable x is energy dependent. Therefore, the likelihood function is made for each energy range of 0.5MeV interval: 6.5∼7.0, 7.0∼7.5, $\cdots$, 13.5∼14.0, and 14.0∼20.0MeV. The probability function is redefined as:

$$P(\cos\theta_{sun,i}, E_i, x_j) = x_j P_{sig}(\cos\theta_{sun,i}, E_i) + (1 - x_j) P_{bg}(\cos\theta_{sun,i}, E_i) \tag{7-4}$$

and x_j is the ratio of number of solar neutrino signals ($xN^{DATA}\frac{N^{MC}}{N^{MC}}$), to the number of events

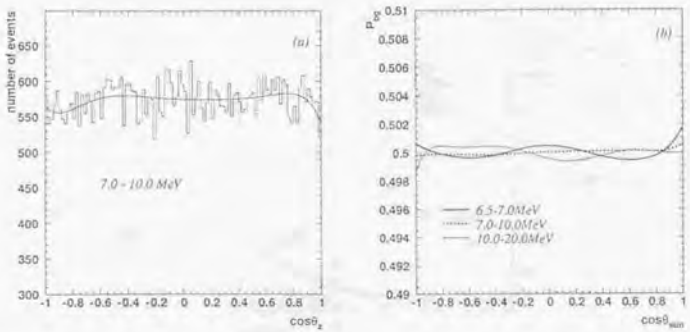

Figure 7–4: Non-flat background distribution. Figure (a) shows $\cos\theta_z$ distribution in the energy range of 7.0~10.0MeV. Figure(b) shows the obtained $P_{bg}(\cos\theta_{sun}, E)$ for three energy ranges.

(N_j^{DATA}) in the j-th energy region:

$$x_j = \frac{N^{DATA}}{N_j^{DATA}} \frac{N_j^{MC}}{N^{MC}} x \tag{7-5}$$

where $N^{DATA}(=\sum_j N_j^{DATA})$, $N^{MC}(=\sum_j N_j^{MC})$ are the total number of final sample events and the solar neutrino MC simulation, and N_j^{MC} is the number of MC simulation events in the j-th energy bin, and x is now an averaged ratio with statistical weights of energy bins. The likelihood function $L(x)$ for getting the solar neutrino flux is given by:

$$L(x) = \prod_{j=1}^{16} \prod_{i=1}^{N_j^{DATA}} P(\cos\theta_{sun,i}, E_i, x_j) \tag{7-6}$$

or

$$\log(L(x)) = \sum_{j=1}^{16} \sum_{i=1}^{N_j^{DATA}} \log(P(\cos\theta_{sun,i}, E_i, x_j)) \tag{7-7}$$

The parameter x which maximizes the likelihood function is searched for with a grid size of 10^{-4}. The measured number of solar neutrino signal N_{signal} is given by:

$$N_{signal} = x_{max} N^{DATA} \tag{7-8}$$

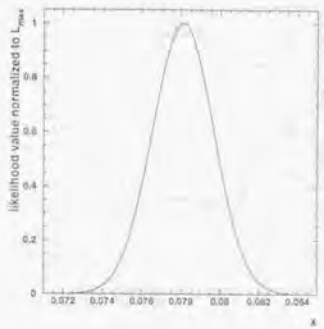

Figure 7–5: The likelihood value as a function of x.

where x_{max} is the x which gives a maximum likelihood value (L_{max}). Figure 7–5 shows the likelihood value as a function of x. Then, N_{signal} is measured to be:

$$N_{signal} = 6768^{+138}_{-130}(\text{stat.})^{+236}_{-196}(\text{syst.}) \tag{7-9}$$

The statistical one standard error is defined as the difference between x_{max} and the x which gives $e^{-0.5}L_{max}(=0.61L_{max})$. The systematic error is described in a following section.

7.1.2 ^{8}B neutrino flux

The SSM (BP98) predicts an event rate of elastic neutrino-electron scattering as 3.331×10^{-3} events/sec in 32ktons detector volume. In the MC simulation, 741646 events remain after the reductions described in chapter 6 out of 7479610 events generated in the 32ktons volume, therefore the efficiency is 741646/7479610. The live time of the solar neutrino observation is 503.8days. Hence, the expected number of solar neutrino events in the energy range of 6.5~20.0MeV in the 22.5ktons fiducial volume is:

$$3.331\times10^{-3} \times \frac{741646}{7479610} \times 503.8 \times 24 \times 3600 = 14377\text{events} \tag{7-10}$$

Hence, a ratio of the observed number of events to predicted, $Data/SSM_{BP98}$, is:

$$\frac{Data}{SSM_{BP98}} = 0.471^{+0.010}_{-0.009}(\text{stat.})^{+0.017}_{-0.014}(\text{syst.}) \tag{7-11}$$

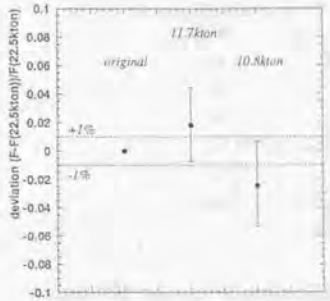

Figure 7–6: Differences of the solar neutrino flux calculation at various conditions. The vertical axis is a flux deviation from the measured value in 22.5kton volume. From the left side, the points reflect original, 11.7kton volume measurement (d_{wall} >5m), 10.8kton volume measurement (2m< d_{wall} <5m). The error bars are only statistical error.

The predicted ^{8}B neutrino absolute flux is $5.15(^{+0.98}_{-0.72}) \times 10^6/\mathrm{cm}^2/\mathrm{s}$ (BP98), therefore, the observed ^{8}B neutrino flux F is obtained to be:

$$F = 2.43 \pm 0.05(\mathrm{stat.})^{+0.09}_{-0.07}(\mathrm{syst.})^{+0.46}_{-0.34}(\mathrm{theo.})(\times 10^6/\mathrm{cm}^2/\mathrm{s}) \tag{7-12}$$

where (theo.) is the theoretical error. In order to check the possible detector bias for the flux measurement, the flux is obtained for inner 11.7kton volume (d_{wall} >5m) and outer 10.8kton volume (2m< d_{wall} <5m). Figure 7–6 compares the fluxes for those volumes. They are consistent with each other within statistical errors. This result concludes that the significant deficit of the ^{8}B neutrino flux is also observed at SK.

7.1.3 Time variation of ^{8}B neutrino flux

The real-time observation of the solar neutrinos in SK enables us to discuss the possible time variation of the solar neutrino flux such as day/night variation. The measurement of the flux time variation has an advantage that uncertainties of the absolute value, such as neutrino flux and cross section, cancel out.

If the MSW effect happens in the earth with the specific parameter region of Δm^2 and $\sin^2 2\theta$, it would be seen that the measured count rate at night is greater than that at day, because muon or tau neutrinos, which are converted from electron neutrinos in the sun, may be re-transformed back to electron neutrinos, which are more easily detected because of the larger cross section.

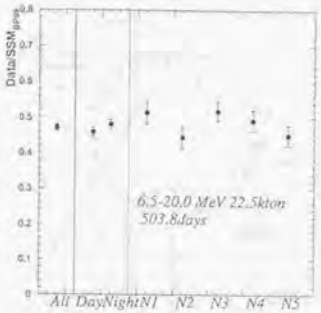

Figure 7–7: The time variation of the solar neutrino flux at all day, day, night, and at night the data is further divided to five zenith angle ranges (see also figure 7–8).

Figure 7–7 compares solar neutrino flux for day-time and night-time. The night-time data is further divided into five zenith angle ranges as shown in figure 7–8 in order to investigate possible zenith angle dependence of the MSW effect in the earth. The measured solar neutrino fluxes for day F_{day} and night F_{night} are:

$$F_{day} = 2.36 \pm 0.07(\mathrm{stat.})^{+0.08}_{-0.07}(\mathrm{syst.})(\times 10^6/\mathrm{cm}^2/\mathrm{s}) \tag{7-13}$$

$$F_{night} = 2.47^{+0.07}_{-0.06}(\mathrm{stat.})^{+0.09}_{-0.07}(\mathrm{syst.})(\times 10^6/\mathrm{cm}^2/\mathrm{s}) \tag{7-14}$$

and the difference, which has smaller systematic error, is:

$$\frac{F_{day} - F_{night}}{F_{day} + F_{night}} = -0.024 \pm 0.020(\mathrm{stat.}) \pm 0.014(\mathrm{syst.}) \tag{7-15}$$

The flux difference is consistent with zero within one standard deviation. In order to test the flux difference between day and night (5 bin), a chi square is calculated:

$$\chi^2_\nu = \frac{\chi^2}{dof} = \frac{7.4}{6-1} = 1.5 \tag{7-16}$$

where χ^2_ν is a reduced chi square and dof is a degree of freedom, and only statistical error is considered in the calculation. Hence, the flux time variation is consistent with none with a probability of 19.2%.

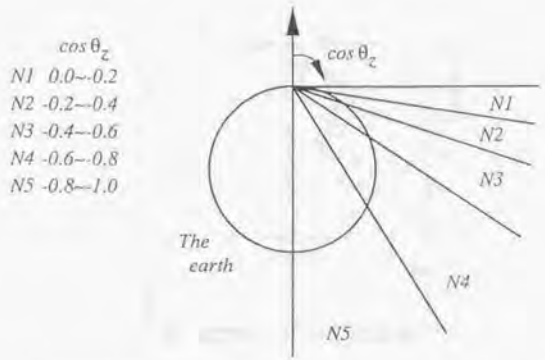

Figure 7–8: Definition of the zenith angle division at night.

7.1.4 Energy spectrum

In addition to the advantage of making real time solar neutrino observations at the SK detector, there is another strong merit to the SK detector. It is the energy spectrum measurement of the solar neutrinos. The observation of an energy spectrum distortion from the expectation would be firm evidence of neutrino oscillations. The energy spectral shape of the ^{8}B solar neutrinos is well known by terrestrial experiments. In order to perform meaningful measurement of the spectral shape, the absolute energy scale of the SK detector needs to be calibrated within 1% accuracy. The determination of the absolute energy scale is achieved by the LINAC calibration as described in chapter 5. Figure 7–9(a) shows the measured energy spectrum of the solar neutrino events and figure 7–9(b) shows the ratio of the measured to the predicted (BP98) as a function of the energy. Figure 7–10 and 7–11 shows the $\cos\theta_{sun}$ distribution of each energy range with the result of the likelihood fit. Inner and outer error bars in figure 7–9 are statistical and systematic errors, respectively (edge of the outer error bar is (statistical)+(systematic) error). The systematic errors are classified into energy correlated errors and energy un-correlated errors. Table 7–1 shows numbers of the solar neutrino events, statistical error, systematic errors (energy un-correlated and energy correlated) for each energy bin. The energy correlated systematic error should be handled with special care when the distortion of the energy spectrum is discussed. Details of the systematic errors are described in the following section.

The measurement of the energy spectrum is also done in the 11.7kton volume (d_{wall} >5m) and in the 10.8kton volume (2m< d_{wall} <5m). Figure 7–12 shows those spectra. Error bars are only statistical error. The two energy spectra are compared using a chi square method. A reduced chi square value is estimated to be 0.59 with 16 degrees of freedom, which corresponds

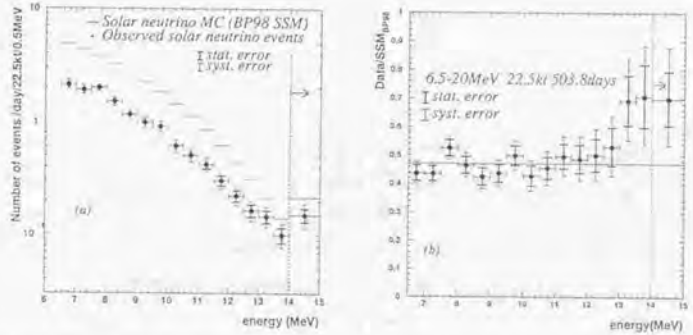

Figure 7–9: Figure (a) shows the measured energy spectrum of the recoil electrons scattered by the solar neutrinos and (b) shows the ratio of the measured to the predicted of the SSM (BP98) as a function of the energy. Explanations of the error bars are written in the text.

energy range (MeV)	number of signal and statistical error	systematic error energy un-correlated(%)	systematic error energy correlated(%)
6.5~ 7.0	1076^{+70}_{-66}	+2.3 −1.7	+1.4 −1.2
7.0~ 7.5	962^{+61}_{-58}	+1.7 −1.7	+1.5 −1.3
7.5~ 8.0	1006^{+56}_{-54}	+1.7 −1.7	+1.7 −1.6
8.0~ 8.5	763^{+50}_{-46}	+1.7 −1.7	+2.0 −2.0
8.5~ 9.0	585^{+43}_{-40}	+1.7 −1.7	+2.4 −2.4
9.0~ 9.5	499^{+36}_{-35}	+1.7 −1.7	+2.9 −2.8
9.5~10.0	459^{+32}_{-31}	+1.7 −1.7	+3.4 −3.3
10.0~10.5	309^{+26}_{-25}	+1.7 −1.7	+3.9 −3.8
10.5~11.0	255^{+22}_{-21}	+1.7 −1.7	+4.5 −4.3
11.0~11.5	211^{+19}_{-18}	+1.7 −1.7	+5.2 −4.8
11.5~12.0	153^{+16}_{-15}	+1.7 −1.7	+5.9 −5.4
12.0~12.5	112^{+13}_{-13}	+1.7 −1.7	+6.6 −6.0
12.5~13.0	83^{+11}_{-10}	+1.7 −1.7	+7.4 −6.6
13.0~13.5	73^{+9}_{-9}	+1.7 −1.7	+8.3 −7.3
13.5~14.0	50^{+8}_{-8}	+1.7 −1.7	+9.3 −8.0
14.0~20.0	77^{+10}_{-10}	+1.7 −1.7	+11.9 −9.9

Table 7–1: Table of number of signals and systematic errors at each energy bin.

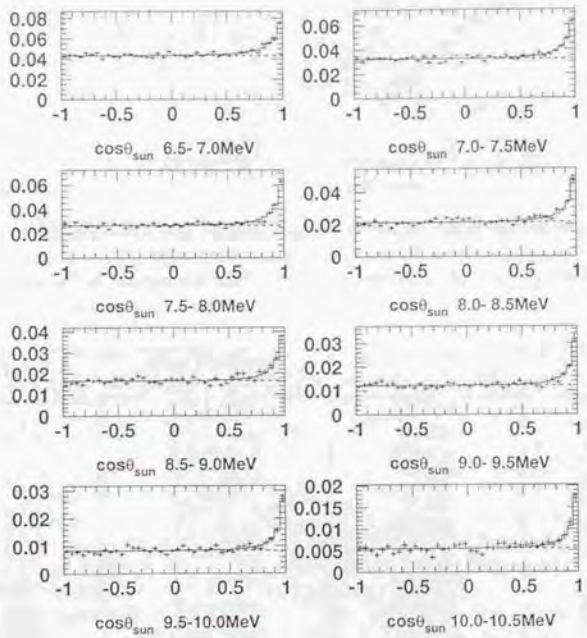

Figure 7–10: The $\cos\theta_{sun}$ distribution for each energy region (6.5∼10.5MeV) with the result of the likelihood fit. The unit of vertical axis is (events/day/kton/bin).

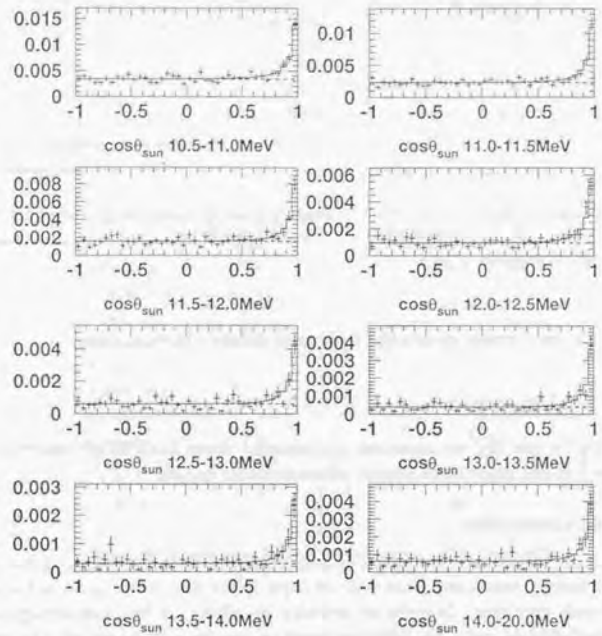

Figure 7–11: The $\cos\theta_{sun}$ distribution for each energy region (10.5∼20.0MeV) with the result of the likelihood fit. The unit of vertical axis is (events/day/kton/bin).

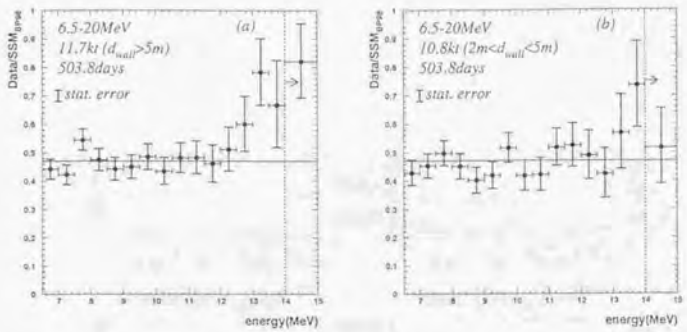

Figure 7–12: The energy spectra in different volume. Figure(a) shows for 11.7kton volume measurement (d_{wall} >5m) and figure(b) shows for 10.8kton volume measurement (2m< d_{wall} <5m). Error bars are only statistical error.

to a 90% C.L.. The two energy spectra are consistent within statistical error.

7.2 Systematic errors

Systematic errors, for the flux measurement and spectral shape analysis are described in this section. Summary of the possible systematic errors is shown in table 7–2.

Energy scale and resolution

It is very important to evaluate systematic errors coming from uncertainties of the absolute energy scale and energy resolution, since they strongly affect the energy spectral shape of the solar neutrino recoil electrons. In order to evaluate its effects on flux and energy spectrum measurements, calculations using the following equation are done with and without artificially changed energy scale and resolution.

$$\mathcal{F}(E_{SK})dE_{SK} = \left\{ \int_0^{E_{max}} F(E_e)R(E_e, E_{SK})\varepsilon(E_{SK})dE_e \right\} dE_{SK} \qquad (7\text{-}17)$$

where E_{SK} is visible energy in the SK detector, $\mathcal{F}(E_{SK})$ is the calculated energy spectrum at the SK detector, E_e is total energy of recoil electrons, and $F(E_e)$ is the energy spectrum of the recoil electrons calculated in equation (3-10). $R(E_e, E_{SK})$ is a detector response function

sources of systematic errors	Flux	Day/Night	Energy spectrum
Energy scale and resolution	$^{+2.2}_{-2.1}$	$^{+1.2}_{-1.1}$	correlated error see figure 7–9
^{8}B neutrino spectrum error	$^{+1.2}_{-1.1}$	–	
Trigger efficiency	$^{+0.3}_{-0.1}$	< 0.1	6.5 – 7.0:$^{+1.7}_{-0.4}$ 7.0 – 20.0:±0
Reduction	±0.7	±0.1	±0.7
Direction	+2.2	–	±1.0
non-flat B.G.	±0.1	±0.4	±0.1
Spallation dead time	±0.2	±0.6	–
Vertex shift	−1.3	–	±1.0
Cross section	±0.5	–	±0.5
Live time	±0.1	±0.1	–
Total	$^{+3.5}_{-2.9}$	$^{+1.4}_{-1.3}$	see figure

Table 7–2: Summary of systematic errors. The unit is %.

(energy resolution function), namely a probability that a recoil electron of energy E_e appears to be E_{SK} in visible energy. $\varepsilon(E_{SK})$ is a detection efficiency function. The energy scale uncertainty is estimated to be $\pm 0.8\%$ at electron energy of 10MeV, which is quadratic sum of following uncertainties.

- $\pm 0.5\%$ due to position dependence of energy scale deviation in figure 5–25(b). It is calculated by multiplying volume weight to the deviation of the energies for each point.
- $\pm 0.5\%$ due to direction dependence. The LINAC calibration can inject electrons only downward direction, therefore in order to extrapolate the energy scale adjustment to whole direction, we have to use the spallation events, and the uncertainty is estimated to be $\pm 0.5\%$ as shown in figure 5–29.
- $\pm 0.22\%$ due to energy scale stability as a function of time. The LINAC calibration was carried out only at a definite time, therefore we have to use figure 5–28 to obtain the energy scale time stability, and the spreads of mean values are estimated to be 0.22% in rms.
- $\pm 0.3\%$ due to the systematic uncertainty of the LINAC calibration system (see table 5–3). This uncertainty has energy dependence as shown in table 5–3, which are incorporated into the energy scale systematic error energy by energy.

Energy dependence of the energy scale deviation in figure 5–25 (a) is also incorporated into the energy scale shift, however it does not contribute to the systematic error so much (net contribution is $< 0.1\%$) when compared with previous uncertainties. The systematic uncertainty of energy resolution is estimated to be 2% as quoted in figure 5–26. In figure 5–26 (c), though the energy resolution of LINAC data is worse than that of corresponding MC about 2%, we assign the systematic error as $\pm 2\%$ conservatively. Figure 7–13 shows a deviation of energy spectrum from the central value with systematically shifted (a) energy scale and (b) energy resolution. Since the energy scale and resolution shift change the calculated solar neutrino flux by $^{+2.2}_{-2.1}\%$, we assign this number as systematic error of the ^{8}B neutrino flux. For the flux ratio of day and night, only directional and time dependence of the energy scale contribute the systematic error, which is estimated to be $^{+1.2}_{-1.1}\%$

^{8}B neutrino spectrum

The uncertainty of the expected ^{8}B neutrino spectrum described in reference [15] is also taken into account in the systematic error. From the "$\pm 3\sigma$" uncertainty given in the reference (and also shown in figure 2–7), $\pm 1\sigma$ energy spectrum deviation is calculated as shown in figure 7–14, where we assume $\pm 1\sigma$ error is one third of the "$\pm 3\sigma$" error. This uncertainty gives $^{+1.2}_{-1.1}\%$ systematic error to the flux.

Trigger efficiency

The trigger efficiency is obtained by the Ni-Cf source calibration as described in section 5.8. In order to estimate the systematic error, the difference between the calibration data and the

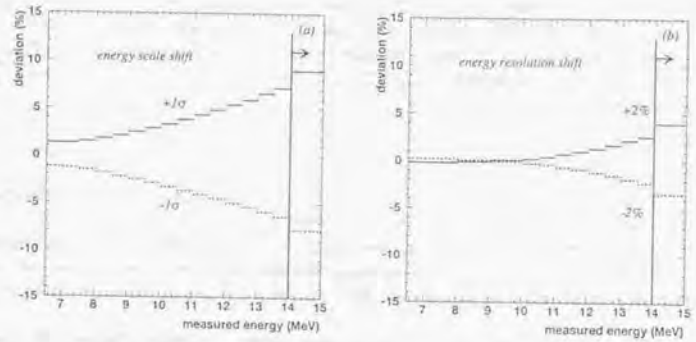

Figure 7–13: The deviations of energy spectrum which is shifted artificially for (a) energy scale and (b) energy resolution from that without shift.

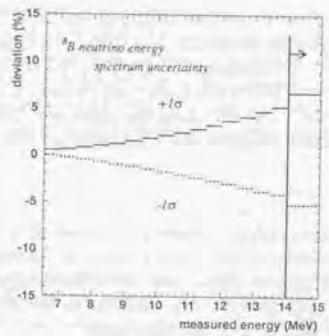

Figure 7–14: Systematic error coming from theoretical ^{8}B neutrino energy spectrum uncertainty.

corresponding MC simulation of the trigger simulator is compared. Above 7MeV energy, the trigger efficiency is 100% for both the data and the MC simulation, hence the difference is negligible. The trigger efficiency for 6.5-7.0MeV depends on the position and direction of events and variation of the water transparency. The dependence is taken into account in the MC simulation, but maximum deviation between data and MC is $^{+0.4}_{-1.7}$%. By changing the efficiency function $\varepsilon(E_{SK})$ in equation (7-17), the systematic error coming from the trigger efficiency uncertainty is estimated. It is evaluated to be $^{+0.3}_{-0.1}$% for the total flux measurement and $^{+1.7}_{-0.4}$% for the energy bin 6.5~7.0MeV.

Reduction

Main sources of the systematic error in the data reduction are the flasher cut (see subsection 6.1.6), and the vertex and directional (VD) test cut (see subsection 6.2.1 and 6.2.2).

Uncertainty of the flasher cut reduction efficiency is studied using the Ni-Cf calibration source and is estimated to be ±0.2% for the solar neutrino flux measurement. Since flasher cut may have a directional anisotropy, the error is also taken into accounnt in the day/night analysis as ±0.1%.

The uncertainty of the VD test cut is evaluated using spallation events[1]. Figure 7-15 shows the reduction efficiency of the spallation events and the solar neutrino MC simulation as a function of energy. Difference of the reduction efficiency has energy dependence as shown in figure 7-15. However, the MC simulation well reproduce the efficiency. Maximum difference above 6.5MeV is 0.7%, which is consistent with the statistical fluctuation, and this value is conservatively taken into account in the systematic error.

Direction

As described in chapter 5, angular resolution is estimated by the LINAC calibration. In order to estimate the uncertainty of the angular resolution, real data and MC simulation of the LINAC calibration are compared. Figure 5-31 (d) shows difference of angular resolution between the real data and the MC simulation. The difference is energy dependent. The difference is corrected in flux and spectral measurements. The estimated-flux difference between with and without correction is +2.2%, and this value is assigned as the systematic error.

Non-flat background

As described in the section 7.1, the $\cos\theta_{sun}$ distribution is fitted with the non-flat background. For the estimation of the uncertainty of flux coming from the background shape, the signal extraction is done using two background shapes, one using flat background and another using the non-flat background. The uncertainty is evaluated to be ±0.1% for the measured solar neutrino flux and ±0.4% for the flux ratio of day and night.

[1]The spallation events used for this purpose are ones selected with a very tight spallation cut, i.e. $Q_{max} > 5\times10^5$p.e. and $DT < 200$msec. DL is not used for the spallation event selection, in order to get non-biased data for the test.

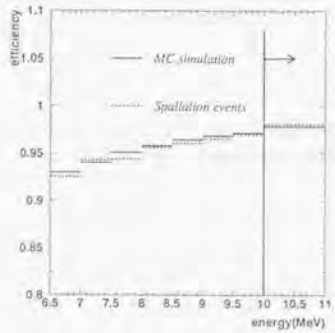

Figure 7-15: Reduction efficiency of the vertex-direction (VD) test cut as a function of energy for spallation events data and the solar neutrino MC simulation. Maximum difference above 6.5MeV is 0.7%.

Spallation dead time

Uncertainty of the dead time of the spallation cut (see appendix B) is studied from two respect, i.e. position dependence and time dependence of the dead time. A measurement of position dependence of the dead time is investigated by comparing the dead time in figure 6-14 with that of constant case, and the difference is estimated to be 0.05%. The time variation of the dead time is evaluated by comparing the dead times for each season and day and night. Consequently the systematic error is estimated to be ±0.2% for the total solar neutrino flux and ±0.6% for the flux ratio of day and night. For the energy spectrum shape analysis, this uncertainty is negligible.

Vertex shift

As described in chapter 5, reconstructed vertex positions for Ni-Cf calibration real data and the corresponding MC simulation are slightly shifted (see table 5-4). This shift may cause a systematic error in the effective volume of the detector. In order to evaluate the systematic error originating from the vertex shift, a shape of the target volume is changed artificially according to table 5-4, and the volume difference is calculated. As a result, the systematic error is estimated to be -1.3% for the solar neutrino flux. For the energy spectrum, the error is assigned conservatively to ±1.0%.

Cross section

The uncertainty of the neutrino-electron scattering cross section mainly comes from the uncertainty of the Weinberg angle θ_W. We use the uncertainty quoted in the reference [33]. The estimated systematic error is $\pm 0.5\%$.

Live time

Live-time is calculated by a few different methods, which use raw data, muon data, or low energy data. The difference between these methods is 0.1% at most.

Chapter 8

Discussions

This chapter presents discussions on the results of solar neutrino measurements given in chapter 7. Contents are interpretations of the recoil electron energy spectrum, implications on neutrino oscillations, and solar core temperature. Future prospect of the solar neutrino measurement is also discussed.

8.1 Interpretations of the recoil electron energy spectrum

This section gives a discussion of interpretations of the recoil electron energy spectrum.

8.1.1 Significance of the distortion

Significance of the energy spectrum distortion is evaluated taking into account the statistical and systematic errors described in the previous chapter. A χ^2 for the test of the distortion is given by:

$$\chi^2 = \sum_{i=1}^{16} \frac{\{R_i - \alpha / f_i(\varepsilon_e, \varepsilon_r, \varepsilon_b)\}^2}{\sigma_i^2} + \varepsilon_e^2 + \varepsilon_r^2 + \varepsilon_b^2 \tag{8-1}$$

where R_i is the observed number of events divided by the expected number of events predicted by the SSM (BP98) for i-th energy bin, α is an arbitrary flux normalization factor. σ_i^2 is square sum of the statistical error and the energy un-correlated systematic error. $\varepsilon_e, \varepsilon_r$ and ε_b are uncertainties in energy scale, resolution and ^{8}B neutrino energy spectrum, respectively. $f_i(\varepsilon_e, \varepsilon_r, \varepsilon_b)$ is a response function for i-th energy bin defined by:

$$f_i(\varepsilon_e, \varepsilon_r, \varepsilon_b) = (1 + a_i\varepsilon_e)(1 + b_i\varepsilon_r)(1 + c_i\varepsilon_b) \tag{8-2}$$

where a_i, b_i and c_i are correlated systematic errors of energy scale, energy resolution and ^{8}B neutrino energy spectrum for i-th energy bin, which are shown in figure 7–13 and 7–14. In order to evaluate the degree of distortion, the parameters $\alpha, \varepsilon_e, \varepsilon_r$ and ε_b are scanned to obtain minimum χ^2. It is obtained to be:

$$\chi^2_\nu = 24.4/(16 - 1) = 1.6 \tag{8-3}$$

Thus, the energy spectrum shape in figure 7–9 is consistent with a flat (expected) distribution with a probability of 5.9%.

8.1.2 Uncertainty of the hep neutrino flux

Recently it is suspected that the excess of the event rate at higher recoil electron energy (13~20MeV, see figure 7–9) is due to the contribution of hep neutrinos created by the reaction (2-8)(for example, see reference [43], [44]). The hep neutrino flux is proportional to the cross section factor of the reaction (2-8). The cross section factor $S_{13}(0)$ has been calculated by many author and most recent best estimated value is

$$S_{13}(0) = 2.3 \times 10^{-20}\text{keV b [13]} \tag{8-4}$$

Though there is no satisfactory way to determine a rigorous error of the value, an error of a factor of 2.5, which spans the entire range of theoretical estimations, is often used in solar neutrino studies.

In order to investigate how much hep neutrino flux is needed to reproduce the excess at higher energy, χ^2 test is applied. The definition of χ^2 is:

$$\chi^2 = \sum_{i=1}^{16} \frac{\left\{ \left(\frac{Data}{F_{^8B}+F_{hep}} \right)_i - \left(\frac{\alpha F_{^8B}+\beta F_{hep}}{F_{^8B}+F_{hep}} \right)_i / f_i(\varepsilon_e,\varepsilon_\tau,\varepsilon_b) \right\}^2}{\sigma_i^2} + \varepsilon_e^2 + \varepsilon_\tau^2 + \varepsilon_b^2 \tag{8-5}$$

where $F_{^8B}$ and F_{hep} are ^{8}B and hep neutrino fluxes predicted by the BP98 model respectively, and α and β are free normalization parameter. The minimum χ^2 value and best fit α and β are:

$$\chi^2_\nu = 15.2/(16-2) = 1.1 \tag{8-6}$$

$$\alpha = 0.436 \pm 0.014 \qquad \beta = 21.7^{+8.5}_{-7.5} \tag{8-7}$$

Figure 8–1 shows the measured energy spectrum and the spectrum $\frac{\alpha F_{^8B}+\beta F_{hep}}{F_{^8B}+F_{hep}}$ with the best α and β. Hence, hep flux needs to be about 20 times larger than the expectation in order to reproduce the excess at the higher energy.

Reference [43] suggests that a ratio, r, of the number of detected events in the 14-16MeV bin to that in the 16-20MeV bin can be used to test the hep neutrino contribution. If the hep neutrino flux predicted by the BP98 model is correct and ^{8}B neutrino flux is normalized to the measured value, $r = 10.4$ is expected, while in the case of 20 times hep neutrino flux, $r = 5.1$. So, the energy bin 14~20MeV is further divided into three energy bins 14-15MeV, 15-16MeV, and 16-20MeV, and r is calculated. Figure 8–2 shows $\cos\theta_{sun}$ distributions for the three energy bins. Table 8–1 shows number of observed events in each energy bin with the ratio to the number of events predicted by the BP98. The measured r is:

$$r = 6.4^{+3.1}_{-2.8} \quad \text{statistical error only} \tag{8-8}$$

It is consistent both with SSM-predicted hep and with 20 times hep assumptions at the present statistical level. We need more statistics for testing the hep contributions.

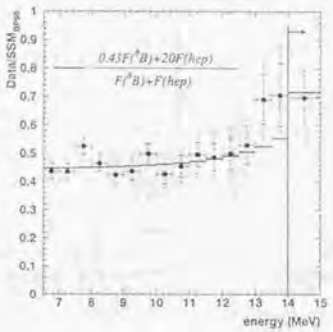

Figure 8–1: The measured energy spectrum divided by the standard energy spectrum (cross marks) and the expected energy spectrum of large (20 times) hep flux case (solid line).

energy range (MeV)	number of events	Data/SSM
14-15	$38.9^{+7.5}_{-7.0}$	$0.532^{+0.102}_{-0.096}$
15-16	$26.4^{+5.8}_{-5.5}$	$1.062^{+0.233}_{-0.220}$
16-20	$10.1^{+4.6}_{-4.0}$	$0.962^{+0.436}_{-0.376}$

Table 8–1: Number of observed events above 14MeV and the ratio to the predicted one by BP98. The errors are only statistical error.

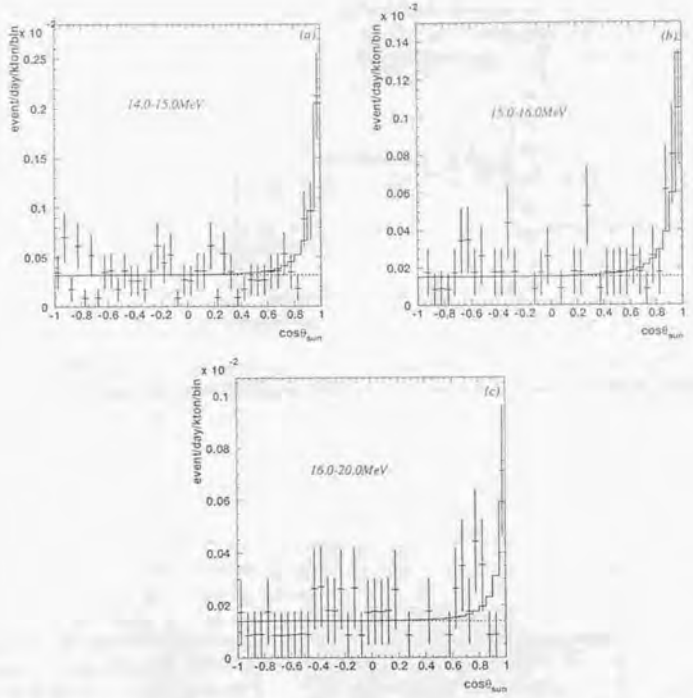

Figure 8-2: Distributions of $\cos\theta_{sun}$ for the three energy regions above 14MeV. Figure (a) is for 14-15MeV, (b) is for 15-16MeV, and (c) is for 16-20MeV.

Summary

The spectral shape comparison between the observed spectrum and the expectation gives a confidence level of 5.9%. An excess of energy spectrum is observed at higher energy end of the spectrum. If one try to fit the spectrum with a hypothetical large flux of hep neutrinos, the flux need to be $21.7^{+8.5}_{-7.5}$ times larger than the SSM prediction.

8.2 Neutrino oscillation study

As described in chapter 2, the solar neutrino problems can be solved by introducing neutrino flavor oscillations. In this section, the observed data are discussed with two flavor neutrino oscillations, and only the outline and results are given.

The neutrino propagation in matter is represented by the time development of the equation of flavor eigenstate as shown in equation (2-39). Technical details are given in appendix D. Here, in order to clarify that the survival probability depends on Δm^2, $\sin^2 2\theta$, and neutrino energy E_ν, the calculated probability in equation (D-15) is rewritten as $p(E_\nu, \Delta m^2, \sin^2 2\theta)$. The recoil electron energy spectrum of equation (3-10) is rewritten as following:

$$F(T_e)dT_e = \left\{ \int_0^{E_{\nu,max}} p(E_\nu, \Delta m^2, \sin^2 2\theta) \frac{d\sigma_{\nu_e+e}(E_\nu, T_e)}{dT_e} \phi(E_\nu) dE_\nu \right\} dT_e + \left\{ \int_0^{E_{\nu,max}} (1 - p(E_\nu, \Delta m^2, \sin^2 2\theta)) \frac{d\sigma_{\nu_\mu+e}(E_\nu, T_e)}{dT_e} \phi(E_\nu) dE_\nu \right\} dT_e \quad (8\text{-}9)$$

where $\phi(E_\nu)$ is sum of ^{8}B ([15]) and the hep ([47]) neutrino energy spectrum predicted by BP98. The expected flux and energy spectrum with neutrino oscillations at SK are calculated using equation (7-17).

For Cl or Ga experiments, the expected count rate $N(\text{Cl or Ga})$ is given by:

$$N(\text{Cl or Ga}) = \int_{E_{th}}^{E_{\nu,max}} p(E_\nu, \Delta m^2, \sin^2 2\theta) \sum_a \phi_a(E_\nu) \sigma(E_\nu; \text{Cl or Ga}) dE_\nu \quad (8\text{-}10)$$

where E_{th} is neutrino interaction energy threshold, i.e. 0.814MeV for Cl and 0.2332MeV for Ga experiments. $\phi_a(E_\nu)$ is the energy spectrum of a-th type neutrinos, where a means pp, pep, ^{7}Be, ^{8}B, ^{13}N, ^{15}O, ^{17}F and hep neutrinos. $\sigma(E_\nu, \text{Cl or Ga})$ is the cross section of the reaction (2-14)[15] for Cl and (2-19)[48] for Ga experiments. In the calculations of expected count rate for Cl or Ga experiments, in the case of Just-so solution, the live time weights $\Delta t_{se,m}$ in equation (D-17) are assumed to be constant, i.e. $\Delta t_{se,m} = 1/N_V$. $\Delta t_{earth,n}$ in equation (D-15) and (D-17) are calculated using latitudes of the GALLEX, SAGE and Homestake experimental sites.

In order to get allowed regions on Δm^2 and $\sin^2 2\theta$ map using the measured results of Cl experiment (2.56±0.23SNU [22]), Ga experiments (72.3±5.6SNU, which is combined value of the results of GALLEX[25] and SAGE[26]) and SK($2.427^{+0.098}_{-0.084}$($\times 10^6$/cm^2/s) for ^{8}B neutrino flux) with the constrainment from the flux prediction in BP98, we follow the method given in reference

[49] with the updated theoretical uncertainties (Cl cross section[15], Ga cross section[48] and diffusion[11]), which uses a following χ^2_{flux}:

$$\chi^2_{flux} = \sum_{i,j=1,3} (R_i^{exp} - R_i^{osc}) V_{ij}^{-1} (R_j^{exp} - R_j^{osc}) \tag{8-11}$$

where R_i^{exp} is the measured count rate (or flux) of i-th experiment (Cl, Ga, SK), R_i^{osc} is the theoretically expected count rate (or flux) with the neutrino oscillations. V_{ij}^{-1} is the error matrix, which is a function of theoretical uncertainties (nuclear reaction cross section, the solar luminosity, heavy element abundances, opacity, the solar age, diffusion (for these uncertainties, see reference [12]), and cross section of neutrino interaction with the experiment target) and experimental statistical and systematic errors.

For the fit using the observed fluxes of all solar neutrino experiments (global fit), the parameter region of $10^{-8}\text{eV}^2 \leq \Delta m^2 \leq 10^{-3}\text{eV}^2$ and $10^{-4} \leq \sin^2 2\theta \leq 1$ is divided into 101×81 and the region of $10^{-11}\text{eV}^2 \leq \Delta m^2 \leq 10^{-9}\text{eV}^2$ and $0 \leq \sin^2 2\theta \leq 1$ into 201×401. Figure 2–16 shows the calculated allowed regions for the MSW solution region and the Just-so solution region, where the allowed region is defined as the region where $\chi^2_{flux} < \chi^2_{flux,min} + 9.21$ (99%C.L.). The minimum χ^2 value and best fit parameter values of (Δm^2, $\sin^2 2\theta$) are obtained to be 0.74 at ($5.62\times10^{-6}\text{eV}^2$, 5.62×10^{-3}).

In order to discuss neutrino oscillations using the spectral shape of the SK measurement, the following χ^2_{espe} is used.

$$\chi^2_{espe} = \sum_{i=1}^{16} \frac{\{R_i^{meas} - \alpha R_i^{osc}/f_i(\varepsilon_e, \varepsilon_\tau, \varepsilon_b)\}^2}{\sigma_i^2} + \varepsilon_e^2 + \varepsilon_\tau^2 + \varepsilon_b^2 \tag{8-12}$$

where α is a free parameter, R_i^{meas} is the measured event rate in i-th energy bin and R_i^{osc} is the estimated event rate with neutrino oscillations, which is a function of Δm^2 and $\sin^2 2\theta$. The excluded region is defined as the region where $\chi^2_{espe}/15 > 2.04$(99%C.L.). Figure 8–3 shows thus obtained excluded region together with the allowed region obtained by the global fit.

The flux comparison between day and night is an another quantity which is able to constraint the oscillation parameters. The definition of χ^2 for day/night analysis is:

$$\chi^2_{dn} = \sum_{i=1}^{6} \frac{\{R_i^{meas} - \alpha R_i^{osc}\}^2}{\sigma_i^2} \tag{8-13}$$

where the index i of the sum means day and N1∼5 (see figure 7–8) and α is a free parameter. Figure 8–4 shows an excluded region obtained by the day and night comparison with a 99%C.L.. As shown in figure 8–4, a lower part of the large angle solution is excluded. For related discussions of the day/night flux variation, see [50] and [51].

Combination of the measured energy spectrum and day/night comparison is also applied to the neutrino oscillation analysis. In order to calculate the allowed regions which satisfy the the measured recoil electron energy spectrum and day/night flux variation, following χ^2_{skall} is

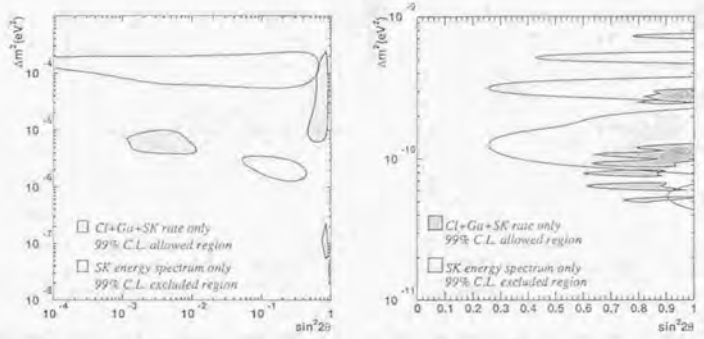

Figure 8–3: The allowed region and the region excluded by the measured energy spectrum with a 99%C.L. for MSW solution and Just-so solution area.

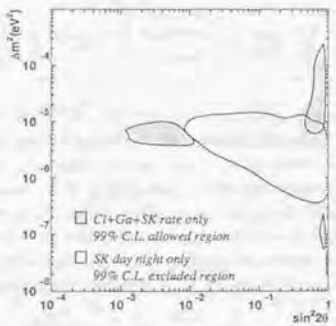

Figure 8–4: The region excluded by the measured day and night flux variation with a 99%C.L..

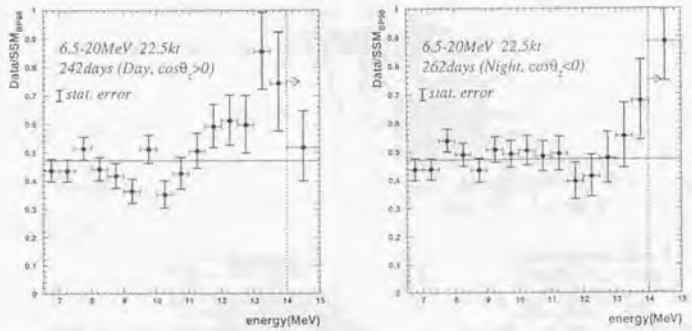

Figure 8–5: The measured energy spectrum at day (left) and night (right). The error bars are only statistical error.

defined:

$$\chi^2_{skall} = \sum_{i=D,N}\sum_{j=1}^{16} \frac{\left\{R^{meas}_{ij} - \alpha R^{osc}_{ij} \Big/ f_j(\varepsilon_{e,i}, \varepsilon_r, \varepsilon_b)\right\}^2}{\sigma^2_{ij}} + \sum_{i=D,N} \varepsilon^2_{e,i} + \left(\frac{1 - \dfrac{\varepsilon_{e,N}}{\varepsilon_{e,D}}}{\sigma_{ud}}\right)^2 + \varepsilon^2_r + \varepsilon^2_b \qquad (8\text{-}14)$$

where R^{meas}_{ij} is the measured energy spectrum for day ($i = D$) and night ($i = N$), which is shown in figure 8–5. $\varepsilon_{e,i}$ is the correlated systematic error of energy scale at day and night, which is constrained by the third term in equation (8-14), where $\sigma_{ud} = 0.005$ is possible systematic energy scale difference between day and night described in chapter 5 (see figure 5–29). R^{osc}_{ij} is the expected event rate with neutrino oscillations and σ_{ij} is a square sum of statistical error and energy un-correlated systematic error for day or night in j-th energy bin, respectively. Figure 8–6 shows the allowed region of oscillation parameters obtained using χ^2_{skall}. The minimum chi square value is obtained to be 39.5 (31 degrees of freedom) at $(\Delta m^2, \sin^2 2\theta) = (4.27\times10^{-10}\mathrm{eV}^2, 0.978)$.

As described above, the large hep neutrino flux can distort the recoil electron energy spectrum for higher energy side (> 13MeV). Here, we try to investigate that how much the large hep neutrino flux affect the allowed region in figure 8–6. An almost same analysis is carried out except that the hep neutrino flux is set to free, i.e. the term αR^{osc}_{ij} in equation (8-14) is replaced

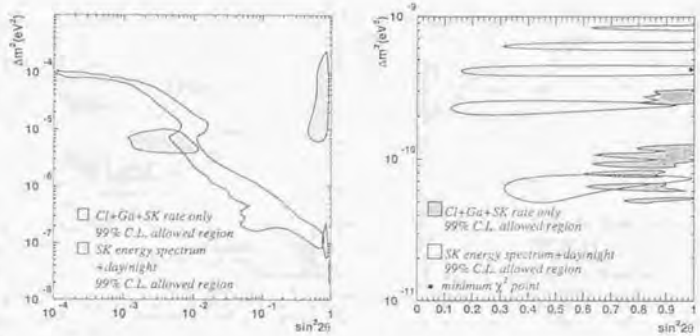

Figure 8–6: The allowed region obtained from combination of measured energy spectrum, flux variation at day and night at 99%C.L..

as follow:

$$\alpha R^{osc}_{ij} \to \alpha R^{osc(^8B)}_{ij} + \beta R^{osc(hep)}_{ij} \qquad (8\text{-}15)$$

where $R^{osc(^8B)\mathrm{or}(hep)}_{ij}$ is the expected event rate with neutrino oscillations for ^{8}B or hep neutrinos, and α, β are free parameters. In the free hep neutrino flux case, we cannot obtain the allowed region, and the obtained excluded region is shown in figure 8–7.

Finally, all measured quantities, i.e. the flux obtained by Cl, Ga and SK, and the day/night flux variation and the recoil electron energy spectrum measured by SK, are used to obtain allowed regions. Definition of χ^2_{all} for this purpose is give by:

$$\chi^2_{all} = \sum_{i,j=1,3} (R^{exp}_i - R^{osc}_i) V^{-1}_{ij} (R^{exp}_j - R^{osc}_j) + \sum_{i=D,N}\sum_{j=1}^{16} \frac{\left\{R^{meas}_{ij} - \alpha R^{osc}_{ij} \Big/ f_j(\varepsilon_{e,i}, \varepsilon_r, \varepsilon_b)\right\}^2}{\sigma^2_{ij}} + \sum_{i=D,N} \varepsilon^2_{e,i} + \left(\frac{1 - \dfrac{\varepsilon_{e,N}}{\varepsilon_{e,D}}}{\sigma_{ud}}\right)^2 + \varepsilon^2_r + \varepsilon^2_b \qquad (8\text{-}16)$$

Figure 8–8 shows the allowed regions with a 99%C.L.. Minimum chi square value is 49.2 at $(\Delta m^2, \sin^2 2\theta) = (5.62\times10^{-6}\mathrm{eV}^2, 6.31\times10^{-3})$ with degree of freedom of 34 (=35-1). The chi square values are acceptable with a 4.4%C.L..

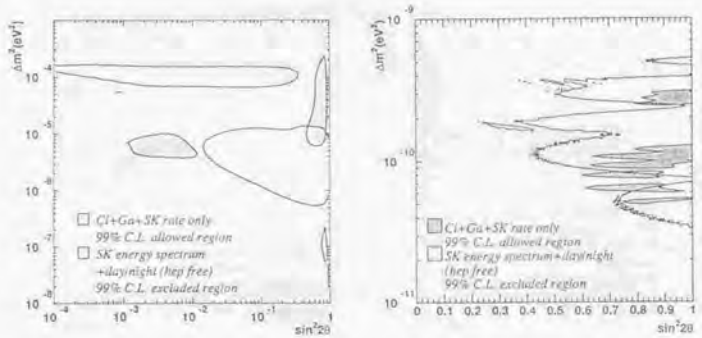

Figure 8–7: The excluded region obtained from combination of measured energy spectrum, flux variation at day and night at 99%C.L. in the case of free hep neutrino flux.

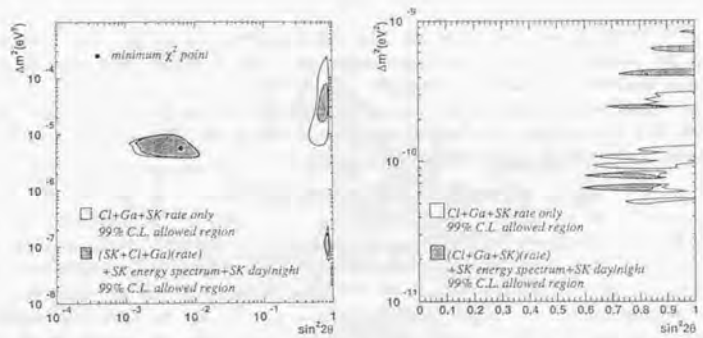

Figure 8–8: The allowed regions which satisfy the measured solar neutrino event rate of Cl, Ga and SK experiments, and day/night flux variation and the energy spectrum measured by SK at 99%C.L..

8.3 Stability of temperature at the center of the sun

The solar neutrino observations are able to investigate the interior of the sun. The ^{8}B neutrino flux $\phi(^8\mathrm{B})$ is very sensitive to the temperature at the center of the sun (T_c). Hence, the measurement of the flux time variation reveals stability of the temperature. Actually, $\phi(^8\mathrm{B})$ is proportional to the 18-th power of T_c, i.e. $\phi(^8\mathrm{B}) \propto T_c^{18}$ [5]. Therefore, the variation of ^{8}B neutrino flux $\delta\phi(^8\mathrm{B})$ and temperature δT_c is correlated with a following relation:

$$\frac{\delta\phi(^8\mathrm{B})}{\phi(^8\mathrm{B})} = 18\frac{\delta T_c}{T_c} \tag{8-17}$$

Figure ?? shows the flux time variation. One bin corresponds to about 33days. The fluctuation around a central value is consistent with each statistical error. Conservatively, we take full width as $\delta\phi(^8\mathrm{B})/\phi(^8\mathrm{B})$, and the fluctuation is found from calculation to be 15.9%. Hence, the temperature at the center of the sun is found to be stable within 0.9% over about two years assuming that possible variation of the solar core temperature is not canceled by the seasonal variation of the flux by neutrino oscillations.

8.4 Future prospect of Super-Kamiokande

This thesis has presented the solar neutrino flux, energy spectrum and day/night analysis using SK 503.8 days live time. Though a slight distortion of the energy spectrum gives a hint of neutrino oscillations, we do not yet have a convincing answer to the solar neutrino problem.

In this thesis, the analysis energy threshold is set to 6.5MeV, because above 6.5MeV trigger efficiency is almost 100%. However, it is very important to measure recoil electron energy spectrum below 6.5MeV, since it enables us to discuss the distortion of the energy spectrum for a wider energy range. Figure 8–9 shows the measured energy spectrum with the expected ones for small angle solution (Δm^2, $\sin^2 2\theta$)= (5.62×10^{-6}eV^2, 6.31×10^{-3}) (broken line), Just-so solution (4.27×10^{-10}eV^2, 0.988) (solid line), and 20×hep neutrino flux with null neutrino oscillations (dotted line). As seen in the figure, future solar neutrino data with the data points below 6.5MeV and higher statistics in higher energy bins enable us to differentiate those possible solutions. The initial motivation of SK for the observation of solar neutrinos is to measure model independent quantities, such as the energy spectral shape or short time variation of the solar neutrino flux, to solve the solar neutrino problem without relying on solar models. Let us consider how many years we need to discuss the current MSW allowed region in the case of null oscillations and to constrain the allowed region in the case of small angle solution (we set (Δm^2, $\sin^2 2\theta$) = (5.623×10^{-6}eV^2, 6.309×10^{-3})) using above 6.5MeV energy spectrum and day/night variation, assuming that the statistical error scales as $\propto \sqrt{1/t}$ (t is observation live time) and the current energy-correlated systematic error is reduced to half. The same χ^2_{skall} in equation (8-14) is used for that purpose. Figure 8–10 shows the 99%C.L. excluded region under the above assumption for 1000 and 4000days observation in the case of null oscillations. As shown in figure 8–10, with the 4000days solar neutrino observation, almost current allowed regions are eliminated except half of the small angle solution. Figure 8–11 shows the 99%C.L.

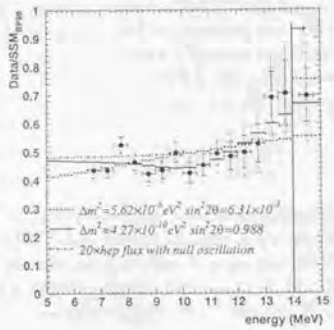

Figure 8–9: The measured energy spectrum. The broken line, solid line and dotted line are the expected energy spectrum for small angle solution(Δm^2, $\sin^2 2\theta$)= (5.62×10^{-6}eV^2, 6.31×10^{-3}), Just-so solution (4.27×10^{-10}eV^2, 0.988) and 20×hep neutrino flux with null neutrino oscillations, respectively.

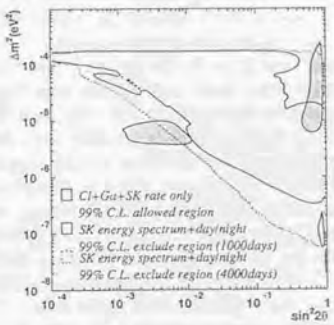

Figure 8–10: The excluded region with 1000 and 4000days solar neutrino observation for the null oscillation case and under the assumption written in the text.

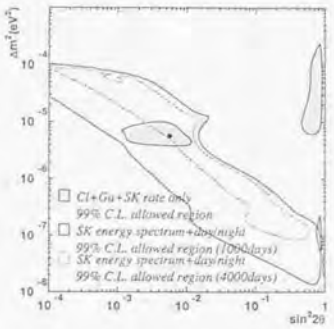

Figure 8–11: The 99%C.L. allowed region calculated using only day/night flux variation and energy spectrum in the case of small angle neutrino oscillations solution at (Δm^2, $\sin^2 2\theta$) = (5.623×10^{-6}eV^2, 6.309×10^{-3})(the filled point in the figure) with 1000 and 4000 days' data.

allowed region for 1000 and 4000 days' data. As shown in figure 8–11, if neutrino oscillations occur at the parameter, (Δm^2, $\sin^2 2\theta$) = (5.623×10^{-6}eV^2, 6.309×10^{-3})(the filled point in the figure), 1000days observation will eliminate the large angle solution at 99%C.L., and 4000days observation will eliminate the LOW solution and further constrain the allowed region. In the small angle solution case, the null oscillations hypothesis test is also carried out. With assumed 1000 days' data, the χ^2 value gives 53.3 with 31 degree of freedom, which is acceptable with only 0.8%.

As described above, the large (20 times) hep neutrino flux distort the expected energy spectrum for higher energy side. In order to settle the "hep neutrino problem", the ratio r should be measured more precisely. It will take about 10 years to measure the r with an accuracy of 10%.

Chapter 9

Conclusion

The 503.8days of solar neutrino data from Super-Kamiokande is presented. The data were taken from 31th of May, 1996 to 25th of March, 1998 and events above 6.5MeV in 22.5kt fiducial volume are analyzed.

The energy spectrum of recoil electrons is measured as shown in figure 7–12. A chi square test is performed to compare the observed and the predicted energy spectrum shape taking into account the systematic errors. The χ^2 value is found from calculation to be 24.4 with 15 degrees of freedom, which corresponds to the significance of 5.9%.

This slightly small significance is discussed with possible large hep neutrino flux and neutrino oscillations. A large hep neutrino flux would affect the energy spectrum, particularly above 14MeV for the recoil electron energy. We found that if the hep neutrino flux is $21.7^{+8.5}_{-7.5}$ times larger than the expectation, the observed spectrum is reproduced. Two flavor neutrino oscillation analysis using the spectrum shape can constrain part of currently allowed region, which explain experimentally measured solar neutrino event rate of Cl, Ga, and SK, at a 99%C.L. as shown in figure 8–3.

Appendix A

Ni-Cf calibration system

A Ni-Cf calibration source emits γ-rays by a reaction Ni(n,γ)Ni, where n is a thermalized neutron originated from a spontaneous fission of ^{252}Cf. Figure 1–1 shows an overview of the Ni-Cf calibration source. A cylindrical polyethylene container with both the height and diameter 20cm contains 2.84kg Nickel wire of 0.1mmϕ and pure water. In the hollow space at the center of the container, a proportional chamber in which ^{252}Cf source is painted on an electrode is located. Intensity of the Cf source is 6.3×10^{4}Bq. ^{252}Cf decay through α decay (96.9%) and spontaneous fission (3.1%). When a ^{252}Cf breaks up by itself, some fast neutrons with averaged kinetic energy ~2MeV are emitted with γ-rays of total energy ~9MeV. The average number of the neutrons and γ-rays produced in one fission are 3.76 and 10.8, respectively. Fission fragments interact with gas in the proportional chamber and make a signal. This signal is called as 'fission trigger' used as triggering of occurrence of the fission event. The emitted neutrons are thermalized by collisions in the pure water filled with the container. The kinetic energy of the neutron decrease down to about 0.025eV and the neutron is captured by Ni nuclei. Mean path length and time of the neutron traveling in this container is ~10cm and ~87μsec (see figure 1–3(a)) respectively. The Ni wire cable can capture the neutrons with high efficiency. The energy of the γ rays produced by the neutron capture reaction of Ni(n,γ)Ni depends on the mass number of Ni nuclei. Table 1–1 shows the energies of γ-rays for various mass numbers of Ni with natural abundances, cross sections and emitted γ-ray intensities. The dominant contribution

mass number	natural abundance (%)	capture cross section (barn)	γ energy (MeV)	intensity (%)
58	67.88	4.4	9.000	65
60	26.23	2.6	7.820	15
62	3.66	15	6.838	12
64	1.08	1.52	6.098	0.4

Table 1–1: The summary of neutron capture of Ni

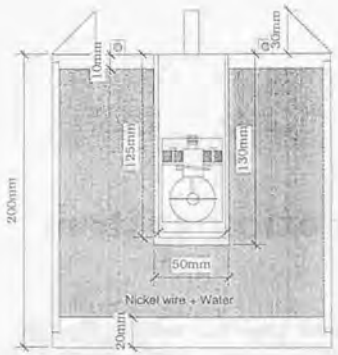

Figure 1–1: An overview of the Ni-Cf calibration source.

of the γ-ray comes from ^{58}Ni(n,γ)^{59}Ni reaction. Figure 1–2 shows a transition diagram of this reaction. In a 52.7% probability, a monochromatic 9.000MeV γ-ray is emitted. The γ-ray which goes out the container scatters electrons by Compton scattering with about 90% probability. The mean energy of the recoil electron is about 7MeV. The remaining 10% γ-ray is converted to an electron-positron pair. Capture cross sections of ^{1}H and ^{16}O are 0.332barn and 0.178mbarn respectively. Though the cross section of ^{1}H(n,γ)^{2}D is small when compared with that of Ni, due to the large number of ^{1}H nuclei (protons), 2.2MeV γ-rays produced by this reaction become main background.

When Ni-Cf calibration data are taken, a 500μsec gate from the fission trigger timing is opened and in the window Ni triggered data (trigger threshold is 150mV, which corresponds to 14hits) are taken. Figure 1–3(a) shows the time distribution from the timing of the fission trigger to that of the Ni trigger. The capture curve of 87μsec life time is seen. The constant bias is due to the 2.2MeV γ-ray background. In order to extract the energy spectrum of the recoil electron events, the energy spectrum in a time range of 300$\sim$450μsec is subtracted from that in 50$\sim$200μsec. The resultant energy spectrum is shown in figure 1–3(b) at the source position of x=(−35.3cm,−70.7cm,0cm). The peak of lower energy in figure 1–3(b) is due to the 2.2MeV γ-rays.

Absolute energy difference between LINAC and Ni-Cf calibration is estimated to be 0.8±0.8%. The main sources of the error 0.8% come from (1)uncertainty of capture cross section, ±0.5%, (2)lines in ^{60}Ni and ^{62}Ni, i.e. the decay lines of ^{60}Ni and ^{62}Ni are not simulated very detail, ±0.5%, (3)uncertainty of reflectivity of obstacle around Ni containers, ±0.25%, (4)uncertainty of position dependence of the neutron capture, i.e. the behavior of the neutrons until they are captured is not simulated, hence the attenuation of γ-ray by material in the container is not

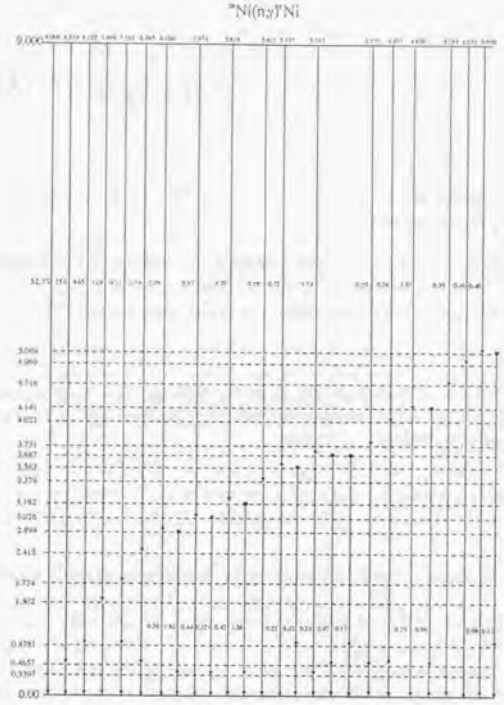

Figure 1–2: The diagram of transition for the reaction ^{58}Ni(n,γ)^{59}Ni.

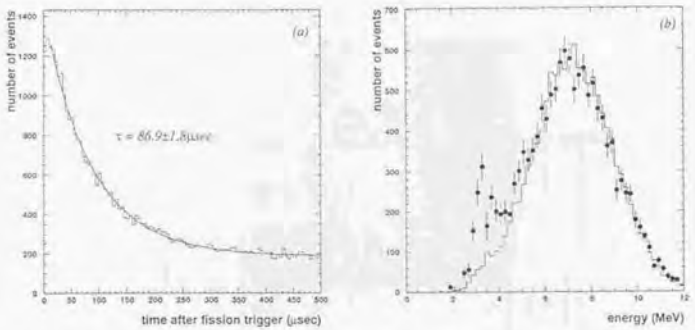

Figure 1-3: (a)Distribution of the time difference from the timing of the fission trigger to that of the Ni trigger. (b) Energy distribution of the Ni calibration data. Filled marks are for data and histogram is for MC simulation data. The source position is x=(−35.3cm,−70.7cm,0cm).

simulated correctly, ±0.2%. Because of the large uncertainty of the Ni-Cf calibration source when compared with that of LINAC calibration system as shown in table 5-3, this source is not used as an absolute energy calibrator currently.

Appendix B

Spallation events

B.1 Spallation products

Spallation events are produced by energetic cosmic ray muons passing through the detector in following interaction,

$$\mu + {}^{16}\mathrm{O} \rightarrow \mu + \mathrm{X} \tag{B-1}$$

where X is radioactive elements. The candidate elements of the spallation products are listed in table 2-1 with life times, decay modes and kinetic energies of the decay products. About 600 spallation products are generated per day in the fiducial volume.

As shown in table 2-1, these radioactive elements emit β-rays and γ-rays whose energies are similar to that of recoil electrons scattered by solar neutrinos. Moreover, these spallation products are generated almost uniformly in space and time, and the directions of the β-rays also distribute uniformly. Hence, these events are a superior calibrator for check of the detector uniformity, although they are troublesome background for the solar neutrino events.

B.2 Method of selection of the spallation events

In order to select (reject) the spallation events, three kinds of information are used, i.e. (1)distance from a muon track to vertex position of a low energy event (DL) [1], (2)time difference between the muon event and the low energy event (DT), (3)residual charge of the muon event (Q_{res}). If DL and DT are small and Q_{res} is large, the low energy event is thought to be a candidate event of the spallation product. Here, Q_{res} is redefined as follow:

$$Q_{res} = Q_{total} - p(t)L \tag{B-2}$$

where $p(t)$ is averaged observed number of photo electrons per unit length of the muon track as a function of time t. This factor cancels out the time variation of total deposit photo-electrons caused by the changing of the water transparency.

[1] Definition of the low energy event is given in chapter 6.

Isotope	$\tau_{1/2}$(sec)	Decay mode	Kinetic Energy(MeV)
$^{8}_{2}$He	0.122	β^-	10.66+0.99(γ)
		β^-+n	(11%)
$^{8}_{3}$Li	0.84	β^-	12.5∼13.0
$^{8}_{5}$B	0.77	β^+	13.73
$^{9}_{3}$Li	0.178	β^-	13.5(75%)
			11.0+2.5(γ)
		β^-+n	∼ 10(35%)
$^{9}_{6}$C	0.127	β^++p	3∼13
$^{11}_{3}$Li	0.0085	β^-	20.77(31%)
		β^-+n	∼16(61%)
$^{11}_{4}$Be	13.8	β^-	11.48(61%)
			9.32+2.1(γ)(29%)
$^{12}_{4}$Be	0.0114	β^-	11.66
$^{12}_{5}$B	0.0204	β^-	13.37
$^{12}_{7}$N	0.0110	β^-	16.38
$^{13}_{5}$B	0.0173	β^-	13.42
$^{13}_{8}$O	0.0090	β^-	8∼14
$^{14}_{5}$B	0.0161	β^-	14.07+6.09(γ)
$^{15}_{6}$C	2.449	β^-	9.82(32%)
			4.51+5.30(γ)
$^{16}_{6}$C	0.7478	β^-	∼4
$^{16}_{7}$N	7.134	β^-	10.44(26%)
			4.27+6.13(γ)(68%)

Table 2-1: Table of the candidate spallation products.

index i	Q_{res} range (p.e.)	A_i	B_i	C_i	DL
1	Q_{res} <2.5×10^4	2.836	5.594	2.107	
2	2.5×10^4 < Q_{res} <5.0×10^4	5.46×10^{-1}	7.176	2.087	
3	5.0×10^4 < Q_{res} <1.0×10^5	2.705×10^{-1}	7.608	1.850	DL ≤2.502m
		2.705×10^{-1}	5.071	0.836	DL ≥2.502m
4	1.0×10^5 < Q_{res} <5.0×10^5	6.607×10^{-2}	8.175	1.301	DL ≤3.635m
		6.607×10^{-2}	5.706	0.622	DL ≥3.635m
5	5.0×10^5 < Q_{res} <1.0×10^6	1.075×10^{-2}	9.187	0.902	DL ≤5.201m
		1.075×10^{-2}	7.288	0.537	DL ≥5.201m
6	Q_{res} >1.0×10^6	2.834×10^{-3}	9.843	0.713	DL ≤5.470m
		2.834×10^{-3}	7.813	0.342	DL ≥5.470m

Table 2-2: The range of 6 Q_{res} and the parameters of the likelihood function L^{DL}_{spa}.

For the purpose of spallation event rejection (spallation cut), a likelihood function is used, which is defined by following equation:

$$L(DT, DL, Q_{res}) = \begin{cases} L^{DL}_{spa}(DL, Q_{res}) L^{DT}_{spa}(DT) L^{Q_{res}}_{spa}(Q_{res}) & \text{(for reconstructed muon)} \\ L^{DT}_{spa}(DT) L^{Q_{res}}_{spa}(Q_{res}) & \text{(for non-reconstructed muon)} \end{cases} \quad \text{(B-3)}$$

Each component of the likelihood function $L(DT, DL, Q_{res})$ is described below.

B.2.1 $L^{DL}_{spa}(DL, Q_{res})$ function

The L^{DL}_{spa} is a likelihood function for distance correlation between the muon track and the low energy event. In order to calculate the function, at first, spallation candidate events are selected using the information of time correlation (DT < 0.1sec) and energy (E >8MeV). Next, DL distributions for 6 Q_{res} ranges are plotted, where 6 each Q_{res} range are written in table 2-2.

Figure 2-1 shows DL distribution for 6 Q_{res} ranges. Let us denote a distribution function as $F^i_{spa}(i = 1, 6)$ for i-th Q_{res} ranges. Peaks around DL < 100cm of each figure are the spallation events and second peaks around $DL \simeq$ 1500cm are non-spallation events which distribute along phase space. In order to obtain DL distribution of the non-spallation events, fake low energy events, which is generated uniformly in the fiducial volume and in time by MC simulation, are prepared. Broken line histograms in figure 2-1 are the DL distribution of the random events. These distribution functions are denoted as $F^i_{rand}(i = 1, 6)$. Then, a prototype likelihood function $L^{prot}_{spa}(DL, Q_{res})$ is defined by:

$$L^{prot}_{spa}(DL, Q_{res}) = \frac{F^i_{spa} - F^i_{rand}}{F^i_{rand}} \quad \text{for } i\text{-th } Q_{res} \text{ region} \quad \text{(B-4)}$$

Figure 2-2 shows distributions of the $L^{prot}_{spa}(DL, Q_{res})$ for 6 Q_{res} regions. The likelihood function

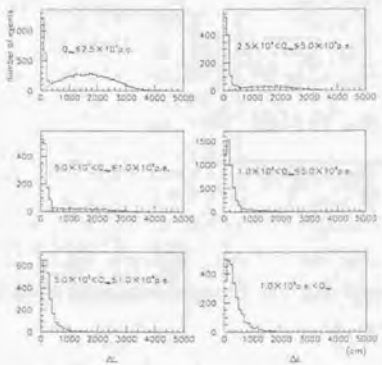

Figure 2–1: DL distributions for 6 Q_{res} ranges.

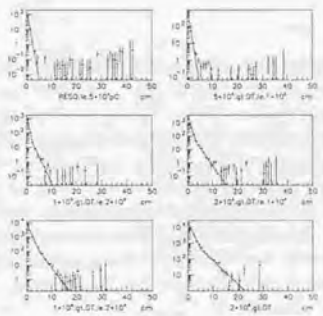

Figure 2–2: The distribution of the likelihood function for DL. Cross marks are the $L_{spa}^{prot}(DL, Q_{res})$ and lines are the likelihood function $L_{spa}^{DL}(DL, Q_{res})$ for 6 Q_{res} regions.

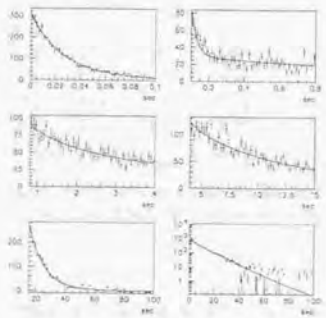

Figure 2–3: The distribution of the likelihood function for DT. Cross marks are DT and lines are fitted likelihood function $L_{spa}^{DT}(DT)$. The right lowest figure is for whole time range 0∼100sec.

$L_{spa}^{DL}(DL, Q_{res})$ is obtained by fitting an assumed function $L_{spa}^{i,fit}(DL)$ given by:

$$L_{spa}^{i,fit}(DL) = A_i e^{B_i - C_i DL} \quad \text{for } i\text{-th } Q_{res} \text{ region} \tag{B-5}$$

Each coefficients are tabulated in table 2–2. Then, the likelihood function for DL is given by,

$$L_{spa}^{DL}(DL, Q_{res}) = L_{spa}^{i,fit}(DL) \quad \text{for } i\text{-th } Q_{res} \text{ region} \tag{B-6}$$

B.2.2 $L_{spa}^{DT}(DT)$ function

In order to obtain the time correlated likelihood function $L_{spa}^{DT}(DT)$, low energy events, whose DL are less than 300cm and energies are greater than 8MeV, parent muon events, whose residual charge Q_{res} are greater than 10^6p.e., are selected in a time range of 0∼100sec for DT. Distributions of DT for 6 DT region are shown in figure 2–3. The distributions are fitted by an assumed function $F_{spa}^{fit}(DT)$:

$$L_{spa}^{fit}(DT) = \sum_{i=1}^{7} A_i 2^{-\frac{DT}{T_{1/2}^i}} \tag{B-7}$$

where $T_{1/2}^i$ is a half life time of typical radioactive elements. The used half life times are listed in table 2–3. In the figure 2–3, typical life times are adopted for each DT region to fit i.e. 0 ∼0.1sec

index i	radioactive element	$T^n_{1/2}$(s)	A_i
1	$^{12}_{5}$B	0.0203	120100
2	$^{12}_{7}$N	0.0110	33900
3	$^{9}_{3}$Li	0.178	338.6
4	$^{8}_{3}$Li	0.84	1254
5	$^{15}_{6}$C	2.449	134.7
6	$^{16}_{7}$N	7.134	676.1
7	$^{11}_{4}$Be	13.83	7.791

Table 2-3: The list of radioactive element and its half life time, which are used to calculate the DT likelihood function. The coefficients of the DT likelihood function are also listed in the last line.

: $^{12}_{5}$B(80%), $^{12}_{7}$N(20%) ; 0.1∼0.8sec : $^{9}_{3}$Li ; 0.8∼4.0sec :$^{8}_{3}$Li ; 4∼15sec : $^{16}_{7}$N ; 15∼100sec : $^{11}_{4}$Be. The right lower figure is whole DT region. The DT likelihood function is given by

$$L^{DT}_{spa}(DT) = L^{fit}_{spa}(DT) \tag{B-8}$$

B.2.3 $L^{Q_{res}}_{spa}(Q_{res})$ function

In order to reconstruct the likelihood function for muon residual charge $L^{Q_{res}}_{spa}(Q_{res})$, time correlated muon events, which are followed by low energy events with energiesy greater than 8MeV and within 0.1sec time window, are selected. Normal muon events un-associated with low energy events are selected. Figure 2–4 shows Q_{res} distributions for two kinds of muon events. The distribution functions of the figure 2–4 are denoted as F_{spa} (for upper figure) and F_{rand} (for lower figure), and a prototype likelihood function is defined by:

$$L^{prot}_{spa}(Q_{res}) = \frac{F_{spa} - F_{rand}}{F_{rand}} \tag{B-9}$$

Figure 2–5 shows the prototype function. To obtain the Q_{res} likelihood function, the prototype function $L^{prot}_{spa}(Q_{res})$ is fitted by a 4th order polynomial and a 2nd order polynomial functions for the Q_{res} range of $Q_{res} < 5.0 \times 10^5$p.e. and $Q_{res} > 5.0 \times 10^5$p.e. respectively. The fitted result is also shown in figure 2–5. The concrete function is given by,

$$L^{Q_{res}}_{spa}(Q_{res}) = \begin{cases} 1.507 \times 10^{-4} + 7.138 \times 10^{-9} Q_{res} + 9.987 \times 10^{-14} Q^2_{res} - 1.307 \times 10^{-19} Q^3_{res} \\ +6.407 \times 10^{-26} Q^4_{res} \quad (\text{for } Q_{res} < 5.0 \times 10^5 \text{p.e.}) \\ -2.644 \times 10^{-2} + 7.086 \times 10^{-8} Q_{res} - 3.661 \times 10^{-15} Q^2_{res} \\ \quad (\text{for } Q_{res} > 5.0 \times 10^5 \text{p.e.}) \end{cases} \tag{B-10}$$

B.2.4 Selection of spallation events

In order to reject the spallation events using the likelihood function, a muon and a low energy event which has maximum likelihood value within a 100sec time window backward in time

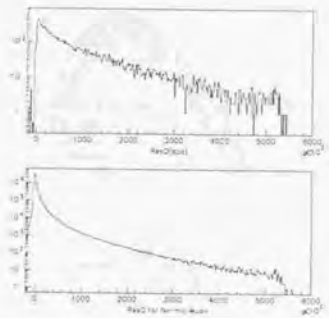

Figure 2–4: Distributions of Q_{res} for the time correlated muon events (upper) and the non-correlated muon events (lower).

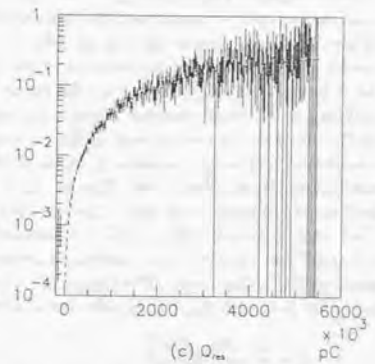

Figure 2–5: The distributions of the prototype likelihood function (cross marks) and the fitted likelihood function (line) for Q_{res}.

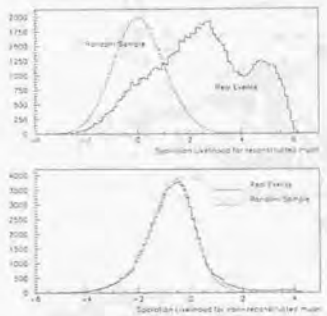

Figure 2–6: The distributions of likelihood value for the reconstructed (upper) and the non-reconstructed (lower) muon events. The solid histograms of two figures correspond to real data. The broken line ones are random sample written in the text for dead time calculation.

from the low energy event are selected for two type likelihood function, i.e. the reconstructed muon likelihood and the non-reconstructed muon likelihood function. Figure 2–6 shows the distributions of likelihood value for the reconstructed and the non-reconstructed muon events. In order to determine a threshold likelihood value to cut the spallation events, 'random sample' events, which are very low energy event (4∼5MeV) disposed randomly in time, are prepared. These events are thought to be β-decay events originated from Rn decay chain or γ-rays coming from outside of the fiducial volume or ID wall material, hence they have nothing to do with the timing of the muon events, i.e. they are non-correlated spallation events. They have vertex position near the wall of the detector. The vertex position is replaced by a random position in the fiducial volume of the detector for the likelihood test. The broken line histograms in figure 2–6 are the likelihood distributions of the random sample. The ratio of the number of removed events to that of all events for random sample, $R_{dead}(l, l')$, corresponds to dead time for the solar neutrino events, where l and l' are the threshold likelihood values for the reconstructed and the non-reconstructed muon events respectively. The threshold values of the likelihood for the spallation cut are determined so as to maximize a significance S defined by:

$$S = \frac{1 - R_{dead}(l, l')}{\sqrt{R_{rem}(l, l')}} \tag{B-11}$$

where $R_{rem}(l, l')$ is the ratio of number of remaining events after the cut to that of all events for real events. Figure 2–7 shows the scatter plot of the dead time and the significance for various l and l'. From figure 2–7, the dead time which gives maximum significance is estimated to be

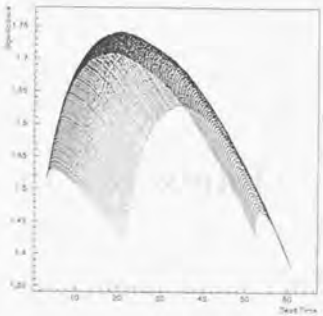

Figure 2–7: The scatter plot of the dead time (horizontal axis) and the significance (vertical axis) for various l and l'.

20% and the threshold likelihood values are given by $l = 0.98$ and $l' = 0.92$.

Appendix C

μ decay electron events

In the ID, about 6000 cosmic ray muons stop in one day. In order to select almost pure μ-decay electron events, following selections are applied, (1)time difference cut in decay time range of 1.5~8μsec[1], (2)fiducial volume cut (i.e. all ID volume(32ktons) $\rightarrow$ fiducial volume(22.5ktons)). Further 18.4% μ^- are captured by oxygen nuclei [53]. Therefore the number of μ-decay electron events we use becomes ~1500 events/day. Figure 3-1 shows time difference distribution between the parent stopping muon events and the following events. A life time of the stopping muon in water is 2.08μsec, which is shorter than that in vacuum (2.20μsec [52]), because the μ^- is captured by ^{16}O nuclei through the following capture process:

$$\mu^- + {}^{16}\mathrm{O} \rightarrow \nu_\mu + {}^{16}\mathrm{N} \tag{C-1}$$

The capture probability is 18.4% and a life time of μ^- decreases to 1.80μsec [53]. A small peak around 15μsec is due to the after pulses described in chapter 3.

The energy spectrum of μ decay electrons (Michel spectrum) is calculated as follow:

$$\frac{dN}{dE_e} = \frac{G_F^2}{12\pi^3} m_\mu^2 E_e^2 \left(3 - \frac{4E_e}{m_\mu}\right) \quad \left(E_e < \frac{m_\mu}{2}\right) \tag{C-2}$$

However, in case of μ^-, the energy spectrum is distorted from the Michel spectrum, since almost all μ^- is trapped by a oxygen atom in K-shell orbit and the decay electron is influenced by electric potential of the oxygen nuclei and orbital motion of the parent μ^- [54], [55]. Figure 3-2(a) shows calculated positron (line histogram) and electron energy spectra (broken line histogram) of decay μ^+ and μ^- in water respectively. In the case of μ^-, the lower peak is due to attractive electrical force of the oxygen nuclei and higher tail is due to Doppler shift caused by the orbital motion of the parent μ^-. Figure 3-2(b) shows the observed energy spectrum in SK detector (cross mark) and a corresponding MC simulation (histogram) with the consideration of the effect. The small peak around 6MeV in figure 3-2(b) is due to γ-ray produced by exited ^{16}N nuclei which captured μ^- by the reaction of (C-1).

The energy of these μ decay electron events (~37MeV) is much higher than that of solar neutrino events (~10MeV), hence it is irrelevant to use these events for the purpose of absolute

[1] In order to reject the after pulse event, only the events decaying in this time range are used.

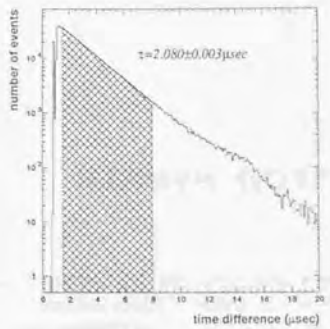

Figure 3–1: The time difference distribution between the parent stopping muon and the following events.

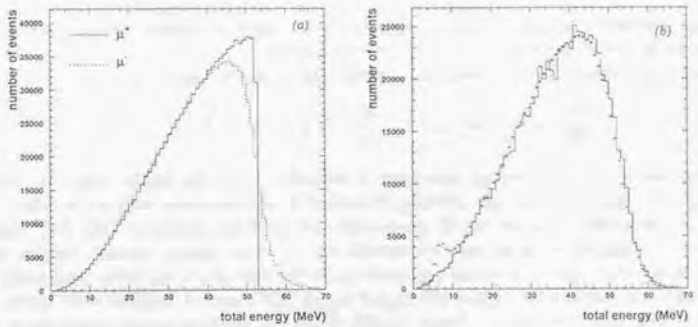

Figure 3–2: Figure (a) shows the calculated positron (line histogram) and electron (broken line histogram) energy spectrum of decay μ^+ and μ^- in water. Figure (b) shows the observed energy spectrum of the μ-decay electrons+positrons in SK detector(cross) and the MC simulation (histogram) with the consideration of the μ^- decay spectrum.

energy calibration. However, it is useful to investigate the systematic difference of absolute energy scale between data and MC simulation auxiliary, and the difference is found to be 1.23±0.24%. Hence, even if the energy is much higher than that of the LINAC calibration, the absolute energy scale is consistent within 1% between data and MC simulation.

Appendix D

Calculation method of two flavor neutrino oscillation

Generally, the two flavor neutrino propagation in matter is described by the time development differential equation (2-39). In a case of uniform matter density, equation (2-39) can be strictly solved:

$$\begin{aligned}
&\begin{pmatrix} |\,\nu_e(L_0+L)\rangle \\ |\,\nu_\mu(L_0+L)\rangle \end{pmatrix} \\
&= \begin{pmatrix} \cos\frac{\pi\omega}{L_V}L + i\frac{\cos 2\theta - \frac{L_V}{L_e}}{\omega}\sin\frac{\pi\omega}{L_V}L & -i\frac{\sin 2\theta}{\omega}\sin\frac{\pi\omega}{L_V}L \\ -i\frac{\sin 2\theta}{\omega}\sin\frac{\pi\omega}{L_V}L & \cos\frac{\pi\omega}{L_V}L - i\frac{\cos 2\theta - \frac{L_V}{L_e}}{\omega}\sin\frac{\pi\omega}{L_V}L \end{pmatrix} \begin{pmatrix} |\,\nu_e(L_0)\rangle \\ |\,\nu_\mu(L_0)\rangle \end{pmatrix} \\
&\equiv P_M(L,N_e)\begin{pmatrix} |\,\nu_e(L_0)\rangle \\ |\,\nu_\mu(L_0)\rangle \end{pmatrix} \qquad \text{(D-1)}
\end{aligned}$$

where

$$\omega = \sqrt{1-2\left(\frac{L_V}{L_e}\right)\cos 2\theta + \left(\frac{L_V}{L_e}\right)^2} \qquad \text{(D-2)}$$

$$L_V = 4\pi\frac{E}{\Delta m^2} = 2.48\frac{E(\mathrm{GeV})}{\Delta m^2(\mathrm{eV}^2)}(\mathrm{km}) \qquad \text{(D-3)}$$

$$L_e = \frac{\sqrt{2}\pi}{G_F N_e} = 1.62\times 10^4\frac{1}{N_e(\mathrm{mol/cm}^3)}(\mathrm{km}) \qquad \text{(D-4)}$$

and L_0 is an original point and L is the propagation length in unit of kilometer. The 2×2 matrix $P_M(L,N_e)$ is the propagation matrix of two flavor neutrino states in traveling length of L, which is also a function of electron density N_e in matter.

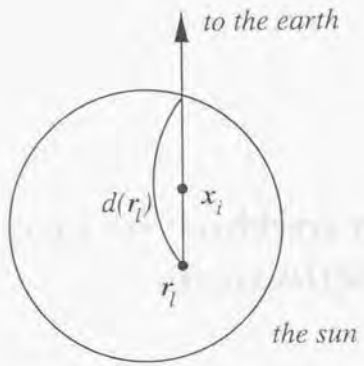

Figure 4-1: Definition of the variables in equation (D-7).

In vacuum case, i.e. $N_e = 0$, the propagation matrix is simplified as follow:

$$P_V(L) \equiv P_M(L,0) = \begin{pmatrix} \cos\frac{\pi}{L_V}L + i\cos 2\theta \sin\frac{\pi}{L_V}L & -i\sin 2\theta \sin\frac{\pi}{L_V}L \\ -i\sin 2\theta \sin\frac{\pi}{L_V}L & \cos\frac{\pi}{L_V}L - i\cos 2\theta \sin\frac{\pi}{L_V}L \end{pmatrix} \quad \text{(D-5)}$$

From now on, in order to simplify we define following vector:

$$|\nu_e\rangle \equiv \begin{pmatrix} 1 \\ 0 \end{pmatrix} \quad |\nu_\mu\rangle \equiv \begin{pmatrix} 0 \\ 1 \end{pmatrix} \quad \text{(D-6)}$$

In order to propagate two flavor neutrino states in the sun, where the electron density depends on the position, we assume that in a short distance at one propagation step the electron density is constant. When a neutrino produced at a position r_l ($l = 1, \cdots, N_l$, and N_l is a number of positions) propagates to the sun surface, the propagation matrix $P_{sun}(r_l)$ is represented by:

$$P_{sun}(r_l) = \prod_{i=1}^{N_{sun}} P_M\left(\frac{d(r_l)}{N_{sun}}, N_e(x_i)\right) \quad \text{(D-7)}$$

where N_{sun} is a number of steps, $d(r_l)$ is the distance from the position r_l to the sun surface as shown in figure 4-1, and $N_e(x_i)$ is the electron density at x_i. Note that the order of the propagation matrix in production of equation (D-7) is determined uniquely.

Next, we consider vacuum propagation between the sun and the earth. Let us denote the distance from the sun to the earth as L_{se}. Because of the elliptical orbit of the earth around

the sun, L_{se} is not constant. The minimum and maximum distance, L_{min} and L_{max}, is:

$$L_{min} = 1.471 \times 10^8(\text{km}) \quad L_{max} = 1.521 \times 10^8(\text{km}) \text{ [45]} \quad \text{(D-8)}$$

In order to consider the variation, we divide the interval $L_{max} - L_{min}$ by a number N_V and define $\Delta L = (L_{max} - L_{min})/N_V$. Let us define live time ratios, $\Delta t_{se,m} (m = 1, \cdots, N_V)$, i.e. which is the ratio of solar neutrino observation time to the total observation time, in which the L_{se} is in the following interval:

$$(m-1)\Delta L + L_{min} \le L_{se} < m\Delta L + L_{min} \quad \text{(D-9)}$$

Of course, $\sum_{m=1}^{N_V} \Delta t_{se,m} = 1$. We assume that in the interval the distance L_{se} is constant value $L_{se,m}$:

$$L_{se,m} = (m - \frac{1}{2})\Delta L + L_{min} \quad \text{(D-10)}$$

At night, the solar neutrinos penetrate the earth, therefore we have to consider the neutrino propagation in the earth only for night time. The propagation matrix in the earth is calculated as follow:

$$P_{earth}(\theta_n) = \prod_{j=1}^{N_{earth}} P_M\left(\frac{d(\theta_n)}{N_{earth}}, N_e(x_j)\right) \quad \text{(D-11)}$$

where $n = 1, \cdots, N_\theta$. N_θ is a number of zenith angle division at night, and θ_n, $d(\theta_n)$, x_j are defined in figure 4-2. N_{earth} is number of propagation steps in the earth. We define the live time ratio to the total live time $\Delta t_{earth,n}$, at which the following condition is satisfied:

$$(n-1)\Delta\theta \le 180^\circ - \theta_z < n\Delta\theta \quad \text{(D-12)}$$

where θ_z is defined in figure 2-15, and $\Delta\theta = 90^\circ/N_\theta$. At day, index n of the ratio $\Delta t_{earth,n}$ is set to be 0. Hence $\sum_{n=0}^{N_\theta} \Delta t_{earth,n} = 1$.

There is one point that we have to be careful. Reference [46] indicates that, at $\Delta m^2 \ge 10^{-7}\text{eV}^2$, at which the MSW effect happens, the solar neutrinos are in incoherent state at the earth due to a spatial separation of mass eigenstates, which is caused by velocity difference of different mass states. In order to take account of the condition, we average over the phase of the neutrino wave function. A simple way to do it is to multiply extra vacuum propagation matrix $P_V(\frac{2L_V}{N_p}k), (k = 1, \cdots, N_p)$ and sum up. This phase average method cancels out phase difference of the neutrino wave function caused by the eccentric orbit of the earth. However, in the Just-so solution region in Δm^2 and $\sin^2 2\theta$ map, the difference of the masses is so small that wave packets of two neutrino mass eigenstates do not separate spatially, i.e. they are still in coherent condition at the earth. Hence, when we calculate an electron neutrino survival probability from the product point in the sun to the SK detector, we have to consider separately

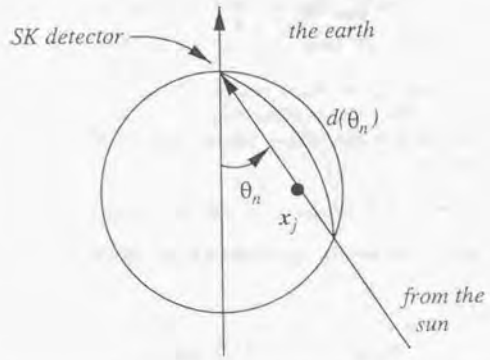

Figure 4–2: Definition of the variables in equation (D-11).

in the MSW solution region and the Just-so solution region. Then we define the MSW solution region as $\Delta m^2 \geq 10^{-8}\mathrm{eV}^2$ and Just-so solution region as $\Delta m^2 \leq 10^{-9}\mathrm{eV}^2$.

In the MSW solution region, the survival probability of an electron neutrino, which is produced at a position r_l in the sun and propagates at the zenith angle of θ_n in the earth, is represented at day:

$$P_{ln}(\nu_e \to \nu_e) = \frac{1}{N_p}\sum_{k=1}^{N_p} |\langle\nu_e|P_V(\frac{2L_V}{N_p}k)P_{sun}(r_l)|\nu_e\rangle|^2 \quad n = 0 \tag{D-13}$$

and at night:

$$P_{ln}(\nu_e \to \nu_e) = \frac{1}{N_p}\sum_{k=1}^{N_p} |\langle\nu_e|P_{earth}(\theta_n)P_V(\frac{2L_V}{N_p}k)P_{sun}(r_l)|\nu_e\rangle|^2 \quad n = 1, \cdots, N_\theta \tag{D-14}$$

Hence, the overall survival probability $P(\nu_e \to \nu_e)$ is:

$$P(\nu_e \to \nu_e) = \sum_{l=1}^{N_l} w_a(r_l)\sum_{n=0}^{N_\theta} \Delta t_{earth,n} P_{ln}(\nu_e \to \nu_e) \tag{D-15}$$

where $w_a(r_l)$ is neutrino production rates at the position r_l of a-type neutrino, where a is an index indicating pp, pep, ^{7}Be, ^{8}B, ^{13}N, ^{15}O, ^{17}F, and hep neutrino.

parameter	number
N_{sun}	10^5
N_l	35
N_V	100
N_θ	45
N_p	40

Table 4–1: Input parameters for the oscillation study.

In the Just-so solution region, the neutrino propagation between the sun and the earth have to be taken into account. When the neutrinos propagate the distance $L_{se,m}$, the probability $P_{lmn}(\nu_e \to \nu_e)$ is calculated as follow:

$$P_{lmn}(\nu_e \to \nu_e) = |\langle\nu_e|P_{earth}(\theta_n)P_V(L_{se,m})P_{sun}(r_l)|\nu_e\rangle|^2 \quad n = 0, \cdots, N_\theta \tag{D-16}$$

where we set $P_{earth}(\theta_0) = 1$ for convenience. Hence the overall survival probability is calculated as follow:

$$P(\nu_e \to \nu_e) = \sum_{l=1}^{N_l} w_a(r_l)\sum_{m=1}^{N_V}\Delta t_{se,m}\sum_{n=0}^{N_\theta}\Delta t_{earth,n} P_{lmn}(\nu_e \to \nu_e) \tag{D-17}$$

We can get conversion probability from an electron neutrino to a muon neutrino, $P(\nu_e \to \nu_\mu)$ by replacing $\langle\nu_e|$ to $\langle\nu_\mu|$ in equations (D-13), (D-14) and (D-16), which is equal to $(1-P(\nu_e \to \nu_e))$. For concrete calculation, we set the parameters in above equations as listed in table 4–1. The neutrino production points are represented by the $(r,\ \theta)$ coordinate system, where r is the distance from the center of the sun and θ is zenith angle respect to the earth direction. The points are (0., 0.06, 0.12, 0.18, 0.24) for r, where the unit is solar radius $R_\odot$, and (0, 30, 60, 90, 120, 150, 180) for θ, where the unit is degree. The weights of the position dependent neutrino production rate, $w_a(r_l)$, are obtained from the table in reference [11].

Bibliography

[1] Z.Maki, M.Nakagawa, S.Sakata, Prog.Theor.Phys. 28(1962)870, V.Gribov and B.Pontecorvo, Phys.Lett 28B(1969)493

[2] L.Wolfenstein, Phys.Rev.D 17(1978)2369

[3] S.P.Mikheyev and A.Yu.Smirnov, Nuovo Cim. 9C(1986)17

[4] Tilton,G.R.,1988, in *Meteorites and the Early Solar System*, edited by J.F.Kerridge and M.S.Matthews(University of Arizona, Tucson),p.259

[5] J.N.Bahcall,"*Neutrino Astrophysics*",(Cambredge,1989)

[6] Turck-Chièze,S. and I.Lopes, Astrophys.J. 408(1993)347.

[7] Castellani, V.S.Degl'Innocenti, G.Fiorentini, L.M.Lissia, and B.Ricci, Phys.Lett.B 324(1994)425.

[8] Kovets,A., and G.Shaviv, Astrophys.J. 426(1994)787.

[9] Christensen-Dalsgaard, J., 1994, Europhysics News 25, 71

[10] Shi,X., D.N.Schramm, and D.S.P.Dearborn, Phys.Rev.D 50(1994)2414

[11] J.N.Bahcall and M.H.Pinsonneault, Rev.Mod.Phys. 67(1995)781

[12] J.N.Bahcall, S.Basu, and M.H.Pinsonneault, Phys.Lett.B 433(1998)1

[13] E.Adelberger, *et.al* Rev.Mod.Phys. (accepted, Oct. 1998) (astro-ph/9805121)

[14] Filippon, *et.al* Phys.Rev.Lett. 50(1983)412, Phys.Rev.C 28(2222)1983

[15] J.N.Bahcall, *et.al*, Phys.Rev.C 54(1996)411

[16] J.Napolitano, *et.al*, Phys.Rev.C 36(1987)298

[17] J.N.Bahcall Phys.Rev. 135(1964)B137

[18] E.K.Warburton, Phys.Rev.C 33(1986)303

[19] F.C.Barker, Aust.J.Phys. 42(1990)1719

[20] B.J.Farmer and C.M.Class Nucl.Phys. 15(1960)626

[21] L.De Braeckeleer, *et.al*, Phys.Rev.C 51(1995)2778

[22] B.T.Cleveland, *et.al*, Astrophys.J. 496(1998)505

[23] Y.Takeuchi, *"Measurement of Solar Neutrino from One Thousand Days of Data at KAMIOKANDE-III"*, Ph.D.thesis, Univ.of Tokyo Ins.of.Tech. (1995)(unpublished)

[24] Y.Fukuda, *et.al*, Phys.Rev.Lett 77(1996)1683

[25] T.Kirstein, talk at *"XVIII International Conference on Neutrino Physics and Astrophysics"* (1998)

[26] V.N.Gavrin, talk at *"XVIII International Conference on Neutrino Physics and Astrophysics"* (1998)

[27] W.Hampel, *et.al*, Phys.Lett.B 420(1998)114

[28] J.N.Abdurashitov, *et.al*, hep-ph/9803418

[29] T.Kajita, talk at *"XVIII International Conference on Neutrino Physics and Astrophysics"* (1998)

[30] Felix Boehm and Petr Vogel "*Physics of Massive Neutrinos*" (Cambridge 1987) p146

[31] N.Hata and P.Langacker, hep-ph/9705339

[32] D.L.Anderson, "*Theory of the Earth*" (Blackwell scientific publication, 1989)

[33] J.N.Bahcall, M.Kamionkowski, and A.Sirlin, Phys.Rev.D 51(1995)6146

[34] H.Ikeda,*et.al*, Nucl.Instr.and.Meth.,A320(1992)310

[35] T.Tanimori, *et.al*, IEEE Tran.on.Nucl.Sci 36(1989)497

[36] Y.Koshio, master thesis (1994) (unpublished)

[37] A.Morel, *et.al*, Limnology and Oceanography 22(1977)709

[38] I.Thorm ähelen, K.Scheffler, and J.Scaub, in *Water and Steam*, Proceedings of the 9th ICPS (Pergamon, Oxford, 1980)

[39] Particle Data Groupe, "Review of Particle Properties" 1994, p1253

[40] M.Nakahata, *et.al*, accepted to Nucl.Instr.and.Meth, hep-ex/9807027

[41] A.Suzuki *et.al* Nucl.Instr.and Meth.,A329(1993)299

[42] Y.Takeuchi, *et.al*, to be published

[43] J.N.Bahcall and P.I.Krastev, hep-ph/9807525

[44] R.Escribano, *et.al*, hep-ph/9805238

[45] Rika nenpyo (chronological Scientific Tables), National Astronomical Observatory (ed.), Maruzen co., Ltd.

[46] M.Fukugita and A.Suzuki, "*Physics and Astrophysics of Neutrinos*", (Springer-Verlag, 1994)

[47] J.N.Bahcall, the detailed table of hep neutrino energy spectrum is obtained from web cite at http://www.sns.ias.edu/ jnb/SNdata/sndata.html#hepspec.

[48] J.N.Bahcall, Phys.Rev.C 56(1997)3391

[49] G.L.Fogli and E.Lisi, Astrop.Phys. 3(1995)185

[50] Super-Kamiokande Collaboration (to be published)

[51] Y.Koshio *"Study of Solar Neutrino at Super Kamiokande"*, Ph.D.thesis, Univ.of Tokyo (1998)(unpublished)

[52] Particle Data Groupe, "Review of Particle Properties" 1998, p21

[53] T.Suzuki, D.F.Measday and J.P.Roalsvig, Phys.Rev.C 35(1987)2212

[54] P.Hänggi *et.al*, Phys.Lett 51B(1974)119

[55] N.C.Mukhopadhyay, Phys.Rep 30(1977)1

Super-Kamiokande Collaboration

Institute for Cosmic Ray Research, University of Tokyo
Y. Fukuda, T. Hayakawa, E. Ichihara, K. Inoue, K. Ishihara, H. Ishino, Y. Itow, T. Kajita, J. Kameda, S. Kasuga, K. Kobayashi, Y. Kobayashi, Y. Koshio, M. Miura, M. Nakahata, S. Nakayama, A. Okada, K. Okumura, N. Sakurai, M. Shiozawa, Y. Suzuki, Y. Takeuchi, Y. Totsuka (spokesman), S. Yamada

National Laboratory for High Energy Physics (KEK)
T. Ishii, J. Kanzaki, T. Kobayashi, S. Mine, K. Nakamura, K. Nishikawa, Y. Oyama, A. Sakai, M. Sakuda, O. Sasaki

Bubble Chamber Physics Laboratory,Tohoku University
M. Etoh, K. Fujita, A. Hasegawa, T. Hasegawa, S. Hatakeyama, T. Iwamoto, M. Koga, T. Maruyama, H. Ogawa, J. Shirai A. Suzuki, F. Tsushima

The University of Tokyo
M. Koshiba

Tokai University
M. Nemoto, K. Nishijima

Department of Physics, Osaka University
Y. Nagashima, M. Takita, T. Yamaguchi, M. Yoshida

Niigata University
W. Doki, K. Miyano, H. Okazawa, C. Saji, M. Takahata

Department of Physics, Tokyo Institute of Technology
T. Futagami, Y. Hayato, Y. Kanaya, K. Kaneyuki, Y. Watanabe

Gifu University
S. Tasaka

Department of Physics, Kobe University
S. Echigo, M. Kohama, A.T. Suzuki

Department of Physics, Seoul National University
S.B. Kim

Boston University
M. Earl, A. Habig, E. Kearns, M.D. Messier, K. Scholberg, J.L. Stone, L.R. Sulak, C.W. Walter

Brookhaven National Laboratory
M. Goldhaber

University of California, Irvine
T. Barszczak, D. Casper, W. Gajewski, P.G. Halverson, J. Hsu, W.R. Kropp, L.R. Price, F. Reines, M. Smy, H.W. Sobel, M.R. Vagins

California State University, Dominguez Hills
K.S. Ganezer, W.E. Keig

George Mason University
R.W. Ellsworth

University of Hawaii
J.W. Flanagan, A. Kibayashi, J.G. Learned, S. Matsuno, V.J. Stenger, D. Takemori

Los Alamos National Laboratory
T.J. Haines

Louisiana State University
E. Blaufuss, B.K. Kim, R. Sanford, R. Svoboda

University of Maryland
M.L. Chen, Z. Conner, J.A. Goodman, G.W. Sullivan

State University of New York, Stony Brook
J. Hill, C.K. Jung, K. Martens, C. Mauger, C. McGrew, E. Sharkey B. Viren, C. Yanagisawa

University of Warsaw
D. Kielczewska

University of Washington
R.A. Doyle, J.S. George, A.L. Stachyra, L.L. Wai, R.J. Wilkes, K.K. Young